APPLICATION OF A LATTICE BOLTZMANN - MOLECULAR DYNAMICS SIMULATION TO PORE-SCALE MODELING OF FLUID FLOW IN SHALE

A Dissertation

by

IJEOMA KINGSLEY MADIEBO

Submitted to the Office of Graduate and Professional Studies of
Texas A&M University
in partial fulfillment of the requirements for the degree of

DOCTOR OF PHILOSOPHY

Chair of Committee,	Hadi Nasrabadi
Committee Members,	Eduardo Gildin
	Maria Barrufet
	Michael King
Head of Department,	A. Daniel Hill

December 2017

Major Subject: Petroleum Engineering

ABSTRACT

In this work, a modified workflow for incorporating molecular effects into a macroscopic fluid flow model via a mesoscopic transition model to more uniformly ascertain transport properties during pore scale analysis, is presented and validated. A combined lattice Boltzmann-molecular dynamics (LBMD) simulation approach to address this issue is employed. The hydrocarbon and shale system taken under consideration here were modeled in molecular form as $n-$octane and silica respectively. The n-octane was set up using the united atom (UA) model. The interaction forcefields primarily employed for the MD system included the standard Lennard-Jones potential, the transferable potentials for phase equilibria (TRAPPE) and the Buckingham potential. The properties studied here were the volumetric flux per unit area, apparent permeability and general fluid dynamics for hydrocarbon flow in the system.

Results from the MD showed a non-linear relationship between the force and the n-octane density. This force was then incorporated into the LB system which already had a Peng-Robinson equation of state embedded into a fluid-fluid particle interaction forcing function. With the variation of the Knudsen number which accounts for slip effect (or gradual deviation from continuum), the fluid dynamics of the system was then modeled. Analysis showed that the slip effect as a function of the Knudsen regime was non-linearly proportional to the volumetric flux per unit area, and thus the deduced permeability of the fluid. The LBMD prediction of apparent permeability showed good agreement with established apparent permeability correlations for shale found in literature. Good qualitative agreement with flow dynamics was also achieved when compared to lab-on-a-chip experiment, representative of nanoscopic shale media and with all results obtained without parameter fitting.

This work aims to extend current understanding of fluid flow behaviour below the continuum regime and improve the accuracy of apparent permeability computation on tight rock geometric imagery, typical of shale rock physics when producing hydrocarbons from shale gas reservoirs. This will be fundamental in the development of a more robust and complex pore-scale modeling framework for simulating more accurate subsurface flow dynamics.

DEDICATION

To my parents, Rowland I. Madiebo and Monica Madiebo, for their help, motivation and support.

ACKNOWLEDGMENTS

I would like to thank my advisor Dr. Hadi Nasrabadi for his mentorship, patience and vision. Specifically, for granting me the opportunity to work on this great project and explore freely other project related ideas during the course of this study. His support in affording me relevant exposure at conferences and meetings can not be overstated. He consistently challenged me to achieve greater heights that made me grow as both a professional and as an individual. So for this, I am grateful.

To the other members on my advisory committee: Dr. Eduardo Gildin for his insightful tutelage to advance and improve this research work, Dr. Michael King and Dr. Maria Barrufet for their enlightened discussions and suggestions that improved the contents of this work; I thank you all. Technical discussions with Dr. Barnerjee also proved invaluable during the course of this study.

I thank the Nasrabadi research group for providing memorable technical discussions during the course of this work.

I offer my appreciation to the Crisman Institute for Petroleum Research and the Texas A&M Energy Institute at Texas A&M University for funding this research project. The High Performance Research Computing Center of Texas A&M University is also acknowledged.

I want to acknowledge my brothers; Chukwunedu, Chibuzor, Ikechukwu and Uchenna for their immense personal support. No words can do justice to how much this meant to me during this academic journey, so I would just say a humble thank you.

I want to thank my departmental doctoral colleagues and friends at Texas A&M University for an incredible learning experience. Other peers of mine I want to thank: Hope Asala, for the personal and academic motivation we have given one another over the years;

and also Bayo Taiwo, for our genuine camaraderie. Along with all my other friends I must have missed who have been in no small way part of my academic journey towards achieving this doctorate degree, I am indeed very appreciative.

Finally, I want to express my utmost gratitude to my parents, Chief and Mrs. R. I. Madiebo, for the unassailable love and care they showed me as a growing child; for the unbelievably selfless and quite often irrational support they afforded myself and my siblings amidst prevalent economic challenges; for instilling the discipline of hard work in me, which I learnt by simply observing their daily lives; and for sacrificing so much to mold me into the person I am today. I thank them greatly for all of these, and I will forever be indebted to them.

CONTRIBUTORS AND FUNDING SOURCES

Contributors

This work was supported by a dissertation committee consisting of Professor Hadi Nasrabadi [advisor], Professor Eduardo Gildin and Professor Michael King of the Department of Petroleum Engineering and Professor Maria Barrufet of the Department of Petroleum Engineering & Chemical Engineering.

All other work conducted for the dissertation was completed by the student independently.

Funding Sources

Graduate study was supported by a research fellowship from the Crisman Institute of Petroleum Research at Texas A&M University

NOMENCLATURE

f	discrete particle distribution function
x	position of the molecule in space
Ψ	potential function
t	time
J	volumetric flux per unit area
$\vec{\xi}$	particle velocity
p	pressure
Q	non-linear integral collision operator
μ	dynamic viscosity
Ω	discrete collision operator
k	permeability
ω	relaxation frequency
λ	mean free path of gas molecule
τ	relaxation time
b	Klinkenberg factor
e	lattice velocity
α	rarefaction coefficient
Kn	Knudsen number
H	distance from center of channel
R	ideal gas constant
$\mathbf{F}$	body force term

ρ	density
r'	reflection coefficient
u	fluid velocity
r	distance between particles
σ	length of scale
ϵ	particle interaction strength
ϵ_0	free space permittivity
e'	elementary charge
V	volume
ϕ	porosity
H	distance from channel centerline to inner boundary
D	channel width
ζ	body force term for particle distribution function
$\hat{\omega}$	accentric factor
Π	stress tensor
m	column vector of moments
M	transformation matrix
S	relaxation time matrix
$\hat{\mathrm{S}}$	collision matrix
U	energy potential

Abbreviations

LB	Lattice Boltzmann
MD	Molecular Dynamics

$LBMD$	Lattice Boltzmann - Molecular Dynamics
PD	Pore Distribution
RD	Rock Distribution
LJ	Lennard-Jones

Subscripts and Superscripts

s	slip coefficient
eq	equilibrium
$\vec{u}$	macroscopic velocity vector
app	apparent
T	temperature
$corr$	correction
m	maximum
o	characteristic
e	effective
ff	fluid-fluid
sf	solid-fluid
$dpdl$	pressure drop
g	gravity
α, β	phase space in x-axis,y-axis
i	discretized phase space direction
d	dimensionless
p	physical

c	critical
l	lattice
r	real
cut	cut-off
$lb-bc$	lattice Boltzmann - mixed boundary condition
$lbmd$	lattice Boltzmann molecular dynamics
N	north
S	south
W	west
E	east

TABLE OF CONTENTS

Page

LIST OF FIGURES

FIGURE Page

LIST OF TABLES

TABLE Page

1. INTRODUCTION

1.1 Background

Even with the recent decline in conventional resources, the global economy continues to remain highly dependent on energy from fossil fuel. The main reason for this is the continuous advancement made in research and development of unconventional resources. Shale gas reservoirs are one of such resources. A key component to be considered during production in such reservoir is the pore distribution network. This is because when it comes to shale reservoirs specifically, there are four levels of pore size distribution scales that can be associated with it and these are: mesoscopic scale comprising hydraulic fractures, meso-microscopic scale comprising of natural fractures, micro-nanoscopic scale comprising of interparticle pores and nanoscopic scale comprising of kerogen pores (Wang and Reed, 2009). In particular, the kerogen pores consist of finely dispersed porous sediments usually rich in organic content and having its pore size range from $2nm$ to $50nm$ (Fathi and Akkutlu, 2012, Kang et al., 2011). A significant amount of the gas is stored in Kerogen pockets as free gas and adsorbed gas is embedded on the surface of the resident organic matter, which therefore makes it have great potential for natural gas production (Kang et al., 2011). To efficiently estimate gas reserves locked in these pores, adequate understanding of the physics of gas flow through ultra low porosity-permeability network is essential.

Diverse spectra of scales that consequently lead to different transport mechanisms occur in shale gas reservoirs. These can be characterized as Knudsen diffusion, slip flow, adsorption-desorption and non-slip flow with the former two being more dominant in the fluid transport process (Chen et al., 2015). Unlike in inorganic channels where two-phase flow controls the gas transport, flow in organic nanochannels have slip flow and transition

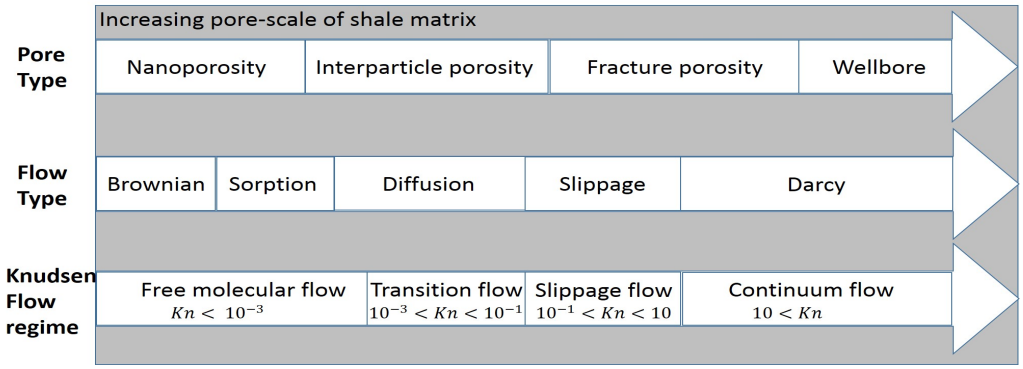

Figure 1.1: Schematic showing shale gas storage matrix and flow regime[*adapted from Sondergeld et. al.,(2010)*]

diffusion flow as the dominant transport mechanism (Shi et al., 2013). High influence of the rarefaction effect that is prominent below the micro-scale, results in reasonably significant deviation of the gas flow from the continuum flow regime assumption and subsequently inaccurately deduced flow variables (Fathi and Akkutlu, 2012, Michalis et al., 2010). The Knudsen number (Kn), which can be defined as the ratio of the molecular mean free-path (λ) to the characteristic system length scale (H) has in recent times been used to characterize fluid flow regimes. These flow regimes have been described (Roy et al., 2003, Sondergeld et al., 2010) as continuum fluid-flow regime $(Kn < 10^{-3})$, slip fluid-flow regime $(10^{-3} < Kn < 10^{-1})$, transition fluid-flow regime $(10^{-1} < Kn < 10)$ and free molecular fluid-flow regime $(10 < Kn)$ as shown in Fig.1.1. For gas flow in micro and nanoporous geometries, the regimes encountered here are typically the slip flow and the transition flow regime. This means the permeability that would typically be calculated based on the Darcy equation, may prove inadequate to properly model the dynamics of flow when dealing with such scale.

1.2 Motivation

Traditionally, permeability has usually been obtained from core measurements during laboratory experiments. Though accepted and employed over the years, it is well-known that these experiments are not only quite expensive but they are also not very robust, especially when dealing with core samples obtained from tight formations with ultra-low permeability (Gong et al., 2013). In recent times, pore-scale modeling techniques have become an emerging technology (Blunt et al., 2013). It employs micro x-ray computed tomography (micro-CT) and scanning electron microscope (SEM) imagery based on the geometric information obtained from cores in order to directly estimate rock properties.

Earlier attempts had been made to analytically describe flow and pore-fluid interface behavior (Vafai and Kim, 1990). Other extensive studies of flow at nanoscale using techniques like molecular dynamics and direct simulation Monte-Carlo have also been explored, with both methods seemingly computationally inefficient (Homayoon et al., 2011, Zhang et al., 2014). The Lattice Boltzmann (LB) method which is one of a few known mesoscopic simulation methods has in recent time garnered interest by the research community. This can be attributed to its simplicity in implementation with respect to other existent methods, complex geometry suitability and numerical superiority when traversing different spectra of scales (Guo et al., 2007). The LB equation can be derived from the continuous Boltzmann transport equation based on the fluid particle distribution function (Mohamad, 2011). The LB method can be classified into two models which are single relaxation-time models based on the Bhatnagar-Gross-Krook (BGK) approximation (Bhatnagar et al., 1954) and multiple relaxation-time models (dHumieres, 1992), which shall be used for the purpose of this study. Some other authors have also shown the ability of the LB method to handle multiphase flow and its effects on viscous coupling (Huang et al., 2009, Wang et al., 2015). This makes it an ideal candidate in computing macroscopic flow

parameters, with emphasis in this case being on permeability.

Some attempts have used the LB method in porescale modeling of porous media specifically to study flow behavior in micro models of reconstructed sandstone and carbonate imagery (Al-Kharusi and Blunt, 2007, Blunt et al., 2013, Boek and Venturoli, 2010); even in multiphase displacement systems (Boek, 2010). However, the permeability computed at this scale is still replicable by continuum flow equations since it still falls in the continuum regime. But for porous media possessing pore spaces below the micro-scale like that observed in shale, the typical intrinsic permeability calculation has seemed inadequate. Over the past few years, the notion of apparent permeability (Javadpour, 2009) has proven popular in order to facilitate simulation work in shale reservoir modeling. The concept incorporates the slip flow and Knudsen diffusion with the advection flow and re-expresses the computed volumetric flux as a coupled form of the Darcy equation already having the intrinsic permeability. This is very useful when applied during studies of natural gas flow in shale, as it reduces computational complexity and establishes a paradigm for which variations in permeability models can be juxtaposed. Due to the higher fluid-wall interaction experienced at this scale, this approach had to be employed to capture this effect.

Standard LB models have a direct proportionality relationship of the existent force between the fluid and the rock and the fluid density. This assumption however is not representative of the actual physical phenomena under certain flow circumstances (Gong et al., 2013), particularly in the slip flow regime. Previous attempts to capture this phenomena had come by way of boundary condition adjustment (Fathi and Akkutlu, 2012, Guo et al., 2007, Homayoon et al., 2011, Succi, 2002, Zhang et al., 2014). This method however has limitations with respect to the selected scheme and it's first order accuracy, which constrains it's applicability (Madiebo et al., 2015, Verhaeghe et al., 2009). Other attempts have aimed at either combining or concurrently comparing the LB and the molecular dy-

namics(MD) methods (Ahlrichs and Dunweg, 1998, 1999, Fyta et al., 2007, Horbach and Succi, 2006, Sbragaglia et al., 2007, Succi et al., 2007). The former only involves comparison while the latter does attempt to couple LB and MD but simultaneous computation and variable transfer between LB and MD for non-focus and focus portions of the system. Gong et al. (2013) more recently has attempted to integrate LB and MD in the form of forcing function inclusions into the standard LB method. However, the set-up considered was for a non-hydrocarbon system with little emphasis on nanoscale considerations. In this work, a modified and more rigorous form of this approach will be adopted for a hydrocarbon system on a pore size more representative of shale matrix.

This study proposes to model the volumetric flux, apparent permeability and general fluid dynamics for hydrocarbon flow in a shale nanochannel using a combined lattice Boltzmann-molecular dynamics simulation method. Results shall be validated by comparison with established apparent permeability correlations for shale and qualitative results from lab-on-a-chip experiment. The aim of this work is to provide a foundation for implementation of this new lattice Boltzmann-molecular dynamics approach for apparent permeability computation on tight rock geometric imagery. This will be fundamental in the development of a more robust and complex pore-scale modeling framework for simulating more accurate subsurface flow dynamics. Particularly for ultra-low permeability core measurements, where experimental accuracy could prove inconsistent when subjected to repeatability under varying fluid and flow conditions.

1.3 Research Objectives and Dissertation Outline

The overall objectives of this research are listed as follows:

1. Develop a molecular dynamics simulation methodology for modeling hydrocarbon phase behavior in nanocapillaries. The simulations involved here shall be executed

using the Large-scale Atomic/Molecular Massively Parallel Simulator (LAMMPS) library which is an open source molecular dynamics software package. The freely available Open Visualization Tool (OVITO) (Stukowski, 2010) would be employed here for observation of molecular structures.

2. Develop an executable code based on a coupled lattice Boltzmann method and molecular dynamics simulation scheme in order to model fluid flow in porous media based on synthetic 2D nanomodel (or SEM image) of shale rock matrix.

3. Model the flow dynamics from hydrocarbon-in-nanofluidic chip experiment. Apply this new approach to calculate flow field and apparent permeability in these nanomodels, which are exemplary of shale reservoir rocks.

The flow of this research and corresponding chapters can be summarized as follows.

Chapter 1: A general introduction, the problem statement and focus of this study

Chapter 2: A review of fluid flow concept and the fundamentals of the lattice Boltzmann method and molecular dynamics simulation.

Chapter 3: Development of the standard LB code for macroscopic Navier-Stokes flow

Chapter 4: Describes molecular dynamics simulation system set-up for shale structure and hydrocarbon model.

Chapter 5: Development of the LBMD approach and how MD would be incorporated.

Chapter 6: Implementation of the LBMD algorithm on test cases and discussion of its performance on these models.

Chapter 7: Summarizes the conclusions and accomplishments of this study and states future work.

2. LATTICE BOLTZMANN METHOD OVERVIEW

2.1 Fluid Flow Fundamentals

2.1.1 Flow mechanics

Fluid flow behaviour can typically be described by the *continuity equation* and the *compressible Navier-Stokes equation* (Latt, 2007, Schmidt and Federrath, 2001) which are given by Eq. 2.1 and Eq. 2.2.

$$\frac{\partial \rho}{\partial t} + \nabla \cdot (\rho \vec{u}) = 0, \tag{2.1}$$

$$\frac{\partial (\rho \vec{u})}{\partial t} + \nabla \cdot (\rho \vec{u} \otimes \vec{u}) + \nabla p - \mu \nabla^2 \vec{u} - \left(\frac{\mu}{3} + \mu'\right) \nabla (\nabla \cdot \vec{u}) = \frac{d\vec{F}}{dV} \tag{2.2}$$

where ρ is the fluid density, $\vec{u}$ is fluid flow velocity, p is the pressure, μ is the dynamic bulk viscosity, μ' is the volume viscosity (typically $\mu' = 0$ in monoatomic ideal gases (Viggen, 2009) and $\frac{d\vec{F}}{dV}$ which is the total external body force assessed as a rate of change of the Newtonian force F with the fluid volume V. When dealing with incompressible fluids, the density variation becomes negligible. Hence at the incompressibility limit, this results in an almost constant density

$$\rho \approx \rho_o = constant \tag{2.3}$$

Based on Eq. 2.3 along with the inclusion of the kinematic viscosity $\nu = \frac{\mu}{\rho}$, effective viscous parameter $\nu_e = f(\nu)$ and porosity ϕ, Eq. 2.1 and Eq. 2.2 can be simplified into Eq. 2.4 and Eq. 2.5 (Guo and Zhao, 2002)

$$\frac{\partial \vec{u}}{\partial t} + (\vec{u} \cdot \nabla) \frac{\vec{u}}{\phi} + \frac{1}{\rho_o} \nabla (\phi p) - \nu_e \nabla^2 \vec{u} = \frac{1}{\rho_o} \frac{d\vec{F}}{dV} \tag{2.4}$$

$$\nabla \cdot \vec{u} = 0, \tag{2.5}$$

Eq. 2.4 and Eq. 2.5 are commonly known as *incompresible Navier-Stokes equation* and *incompressible continuity equation* respectively. These equations are popularly used for studying flow incompressible fluids, typical of most liquids. Since this study focuses on a liquid hydrocarbon, these equations form a fundamental basis of this work. Mainly to link the mesoscopic scaled - LB method to the macroscopic scale.

2.1.2 Mesoscopic concept in fluid dynamics

For most engineering problems, a macroscopic and continuum description has typically proven adequate simply because of the huge disparity that exists between temporal and spatial scales pertinent to these applications and the microscopic scales for the underlying molecular dynamics. This usually results in the insensitivity of the macroscopic dynamics to the underlying microscopic physics. With multi-scale and multi-physics engineering applications recently gaining more attention, macroscopic methods have proven inadequate and microscopic or molecular methods may be impractical due to the unreasonable computational demands required for execution. Mesoscopic techniques has proven popular in recent years based on their ability to combine microscopic and macroscopic physics for adequate fluid dynamics description especially in multi-scale applications. One of such techniques is the lattice Boltzmann (LB) method while others include lattice gas cellular automata, discrete velocity models, gas kinetic schemes, dissipated particle hydrodynamics and smoothed particle hydrodynamics (Derksen et al., 2013). The focus of this study shall be on the LB method.

2.2 Apparent Permeability

When it comes to reservoir engineering, a key concept to be considered is the permeability. It is a measure of fluid flow capacity in any porous media. Popularly calculated from the Darcy equation, it was originally derived on the basis of the continuum assumption. One

of the several variants that could be used to express this equation is given as:

$$\vec{u} = J = -\frac{k}{\mu}\nabla p, \tag{2.6}$$

where J is the volumetric flux rate per unit area, μ is the dynamic viscosity, Δp is the pressure gradient and k is the intrinsic permeability which is typically a function of the porous media structure. Although Darcy's equation has been used for fluid flow calculations in porous media, it is important to note that with decreasing pore size comes an increase in the Knudsen effect governed by an increase in Knudsen number. Thus, increasing the uncertainty in the validity of its application involving flow at micro and nanoscale (Beskok and Karniadakis, 1999). Such permeability parameter attempting to factor in this phenomena in the Darcy equation is usually redefined as the apparent permeability. The apparent permeability (Javadpour, 2009, Klinkenberg, 1941) based on the Dusty Gas model (DGM) can be modeled as in Eq. 2.7, where $f_{corr}(Kn)$ is the permeability correction factor that is a function of the Knudsen number.

$$k_{app} = k f_{corr}\left(Kn\right). \tag{2.7}$$

Over the years, different correlations have been suggested in literature for apparent permeability along with their corresponding Knudsen correction factors (Swami et al., 2012). Some of these correlations had been compared and matched with actual experimentally reported shale gas data (Civan, 2009) along with being defined solely on the Knudsen phenomena, hence their selection for this study. The proposed correction based on the Klinkenberg (1941) correlation for apparent permeability is shown in Eq. 2.8. Florence et al. (2007) and Sakhaee-Pour and Bryant (2012) define the parameter Λ as 4 and 13.58

respectively.

$$k_{app} = k\left(1 + \Lambda Kn\right). \tag{2.8}$$

Civan (2009) gave a simplified form for the factor in the model initially proposed by Beskok and Karniadakis (1999). This can be modeled by Eq. 2.9 and Eq. 2.10, where $b = -1$ and $\alpha(Kn)$ denotes the rarefaction coefficient when dealing with slip flow. We would refer to the combination of these two equations as the Beskok and Karniadakis –Civan correction during the rest of this study.

$$f_{corr}\left(Kn\right) = \left[1 + \alpha\left(Kn\right)\right]\left[1 + \frac{4Kn}{1 - b \cdot Kn}\right]. \tag{2.9}$$

$$\alpha\left(Kn\right) = \frac{1.358}{1 + 0.17Kn^{-0.4348}}. \tag{2.10}$$

Chen et al. (2015) studied the pore structures of shale based on a reconstructed pore network obtained via Markov chain Monte Carlo (MCMC) on some SEM image slices, and thus proposed a correction factor as described in Eq. 2.11.

$$f_{corr}\left(Kn\right) = \left(1 + \frac{64}{3\pi}Kn\right). \tag{2.11}$$

The variant of the Hagen-Poiseuille equation for parallel plates being employed here was in its dimensionless form (Chen et al., 2015, Zhang et al., 2014) and representative of the analytical permeability and velocity in the channel, are shown in Eq. 2.12 and Eq. 2.13, respectively. Refer to appendix A for the analytical solution for Eq. 2.13.

$$k = \frac{D_p^2}{12}. \tag{2.12}$$

$$\frac{u}{u_m} = 1.5\left[1 - \frac{y^2}{H^2}\right]. \tag{2.13}$$

where u is the fluid velocity calculated at a given distance y from the center of line, u_m is the mean fluid velocity of the nanochannel, y is the distance measured from the center line of the width of the channel and H is the fixed distance measured from the nanochannel center line to the inner boundary wall and it is equivalent to one half of the nanochannel width, D_p. This equation along with the other aforementioned correlations, were employed for comparison with the apparent permeability obtained from the lattice Boltzmann simulation in this work.

2.3 Review of the Lattice Boltzmann method

The lattice Boltzmann method is a computational technique for simulating the physics of flow using microscopic particle distribution functions via the evolution of preset directionally discretized positions and velocities. All this are done whilst still maintaining all mass and momentum conservation laws. Despite being a numerical scheme based on microscopic physics, in the hydrodynamic limit of low Mach number it still possesses the ability to to recover the Navier-Stokes equations (Chukwudozie, 2011, Succi et al., 1989). Emanating from an attempt to address the anomalies of the lattice gas automata (McNamara and Zanetti, 1988), the LB equation can be derived from the Boltzmann transport equation (C., 1988, Homayoon et al., 2011) represented in Eq. 2.14.

$$\frac{\partial f(x,\vec{\xi},t)}{\partial t} + \vec{\xi}\cdot\nabla f(x,\vec{\xi},t) = Q, \tag{2.14}$$

where $f(x,t,\vec{\xi})$ represents the Maxwellian probability distribution function of locating a molecule at a particular position x, whilst traveling at a time t and at a given continuous velocity $\vec{\xi}$, with a non-linear integral term Q as the collision operator comprising of pre-collision and post-collision distribution functions. Eq. 2.14 in its discrete form becomes

Eq. 2.15

$$\frac{\partial f_i}{\partial t} + e_i \cdot \nabla f_i = \Omega_i. \tag{2.15}$$

Without loss of generality, the collision operator can be simplified to a discrete collision operator Ω_i with the phase space direction i. After ensemble averaging of the particle distribution functions, *the lattice Boltzmann evolution equation* can be defined as

$$f_i(x + e_i\Delta t, t + \Delta t) - f_i(x, t) = \Omega_i, \tag{2.16}$$

where we have f_i which is the discretized particle distribution function, e_i denotes the discretized particle velocity, Δt is the discretized time.

It should be noted that Eq. 2.16 is the foundation for the LB method. The fundamental LB method comprises of two major steps: the *streaming step* and the *collision step*. In the streaming step, particles are translated along particular velocity directions between nodes. In the collision step, particles collide with one another at particular nodes which leads to momentum exchange. It is defined by the collision operator in Eq. 2.16.

Transitioning from the discrete kinetic equation to macroscopic equations can easily be done via the derivation of mass and momentum conservation equations using the distribution function f_i and its moments in Eq. 2.17 and Eq. 2.18.

$$\rho(\vec{x}, t) = \sum_i f_i(\vec{x}, t) \tag{2.17}$$

$$\rho(\vec{x}, t)\vec{u}(\vec{x}, t) = \sum_i \vec{e_i} f_i(\vec{x}, t) \tag{2.18}$$

With the inclusion of ζ which is the change in particle probability distribution function due to the total body force term $\mathbf{F}$, Eq. 2.16 can be changed into the generalized lattice Boltzmann equation (Gong et al., 2013, Qian et al., 1992, Shan and Chen, 1994) shown

in Eq. 2.19

$$f_i(x + e_i\Delta t, t + \Delta t) - f_i(x, t) = \Omega_i\left(x, t\right) + \zeta_i\left(x, t\right), \tag{2.19}$$

where ζ can be computed using the exact difference method (Kupershtokh and Medvedev, 2006) as shown in Eq. 2.20

$$\zeta_i\left(x, t\right) = f_i^{eq}\left(\rho, \vec{u} + \Delta\vec{u}\right) - f_i^{eq}\left(\rho, \vec{u}\right) \tag{2.20}$$

This now leads to Eq. 2.21 and Eq. 2.22 as required for retrieval of the generalized Navier-Stokes equation with $\vec{\mathbf{u}}$ representing the real fluid velocity (Guo et al., 2007).

$$\rho = \sum_{i=0}^{8} f_i\left(x, t\right). \tag{2.21}$$

$$\vec{\mathbf{u}} = \frac{1}{\rho}\sum_{i=0}^{8} f_i\left(x, t\right) \cdot \vec{e_i} + \frac{\Delta t}{2}\mathbf{F}. \tag{2.22}$$

$\mathbf{F}$ can be categorized under any of the following: lattice fluid-fluid force interaction between neighbor lattice F_{ff}, lattice solid-fluid boundary wall interaction F_{sf}, and macro body force like the body force term for the pressure drop F_{dpdl} or body force term for gravity F_g. Emphasis of this work was on the determination of the interaction force F_{sf}. With the employment of the Chapman-Enskog expansion , the familiar version of the conservation laws analogous to Eq. 2.1 and Eq. 2.2 can be obtained in Eq. 2.23 and Eq. 2.24 (Tarakanov et al., 2016)

$$\frac{\partial\left(\rho u^{\alpha}\right)}{\partial t} + \frac{\partial}{\partial x^{\alpha}}\left(\rho u^{\alpha} u^{\beta}\right) = -\frac{\partial}{\partial x^{\beta}}\Pi^{\alpha\beta} + \sum_i F_i e_i^{\alpha}, \tag{2.23}$$

$$\frac{\partial\rho}{\partial t} + \frac{\partial}{\partial x^{\alpha}}\left(\rho u^{\alpha}\right) = 0, \tag{2.24}$$

The function $\Pi^{\alpha\beta}$ represents the stress tensor given by the expression

$$\Pi^{\alpha\beta} = \sum_i \left(c_i^\alpha - u_i^\alpha\right)\left(c_i^\beta - u_i^\beta\right) f_i, \tag{2.25}$$

This can be approximated using the Taylor series expansion with a relaxation time parameter τ during the Chapman-Enskog procedure to obtain Eq. 2.26

$$\Pi^{\alpha\beta} = P\delta^{\alpha\beta} + \tau P\left(\frac{\partial u^\alpha}{\partial x^\alpha} + \frac{\partial u^\beta}{\partial x^\beta} - \frac{2}{3}\frac{\partial u^\gamma}{\partial x^\gamma}\partial^{\alpha\beta}\right) + \tau\left(\rho\frac{\partial P}{\partial \rho} - \frac{1}{3}P\right)\frac{\partial u^\gamma}{\partial x^\gamma}\partial^{\alpha\beta} + O\left(\tau^2\right) \tag{2.26}$$

where $\sum_i F_i e_i^\alpha$ accounts for the external macroscopic forces like electrical or gravitational forces (Tarakanov et al., 2016). From Eq. 2.25 it is clear that there is an assumed dependence of pressure on the fluid density specified, that is $P = P(\rho)$ and $\tau = \frac{\mu}{P}$. In addition, as the system approaches equilibrium, Eq. 2.22 - 2.25 approximates to a standard macroscopic fluid behaviour. See Guo and Zhao (2002), Latt (2007), Viggen (2009),Tarakanov et al. (2016) for more details on the Chapman-Enskog expansion usage in the LB method for macroscopic reformulation.

2.3.1 Lattice scheme

In order to implement the LB method, an exact lattice scheme has to be selected for the simulation set-up (Frisch et al., 1986). Various schemes can be used for the lattice in either two or three dimensions. For two dimensional simulations, a nine-speed square lattice aligned in only two dimensions $[D2Q9]$ has extensively been used (Abbaszadeh et al., 2015, Amara et al., 2016, Benamram et al., 2016, Fathi and Akkutlu, 2012, Guo et al., 2007, Homayoon et al., 2011, Madiebo et al., 2015, Succi, 2002, Tarakanov et al., 2016). Fig. 2.1a shows this $[D2Q9]$ scheme and Fig. 2.1b shows the particle distribution function assigned to particular discretized molecular velocity. This is not only because of its ease of implementation and its simplicity, but rather its ability to satisfy isotropic conditions

necessary for the recovery of the incompressible Navier-Stokes equation (Viggen, 2009). Hence, this was the lattice scheme implemented for this work.

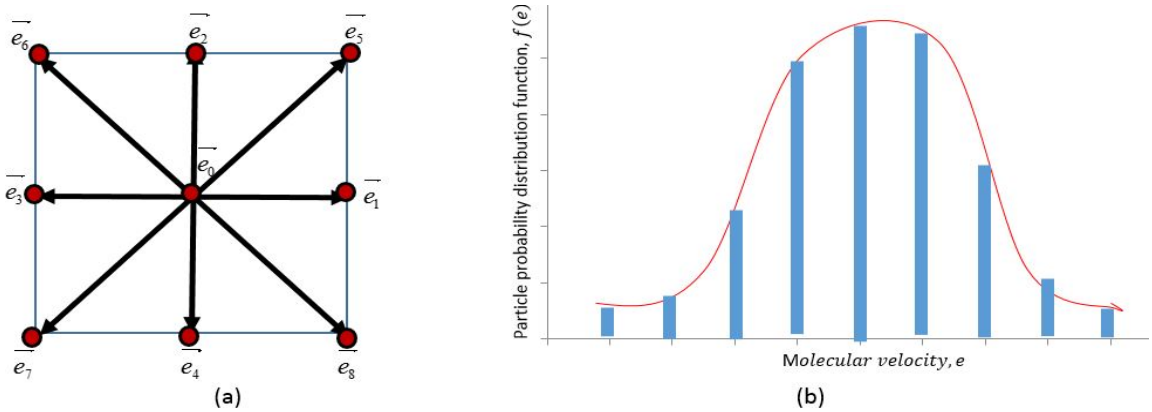

Figure 2.1: (a) A discretized two-dimensional lattice vector scheme for the LB method. (b) A discretized particle probability distribution function for a fluid $f(e)$ as a function of molecular velocity, e

2.3.2 Collision operator

In terms of kinetic models to approximate the collision term Ω_i, the Bhatnagar-Gross-Krook (BGK) approximation (Bhatnagar et al., 1954) and the Multiple Relaxation Time (MRT)(dHumieres, 1992) are the most commonly employed operators..

2.3.2.1 BGK operator

The BGK operator is shown in Eq. 2.27. τ is the relaxation time (Note: $\tau = \frac{1}{\omega}$, where ω is the relaxation frequency). It is usually assumed constant when handling an isothermally incompressible fluid and f_i^{eq} is the local equilibrium distribution function. The operator

$$\Omega_i = -\frac{1}{\tau}(f_i - f_i^{eq}). \tag{2.27}$$

If Eq. 2.27 is inserted back into the collision operator of Eq. 2.19, Eq. 2.28 is obtained.

$$f_i(x + \vec{e_i}\Delta t, t + \Delta t) - f_i(x,t) = -\frac{1}{\tau}\left[f_i(x,t) - f_i^{eq}(x,t)\right] + \zeta_i\left(x,t\right), \tag{2.28}$$

f_i^{eq} is the Maxwellian equilibrium particle distribution function that dictates the flow equations solved for the selected lattice Boltzmann scheme. In this case, for a $D2Q9$ scheme needed for solving the Navier-Stokes equation this function can be expressed in the form of Eq. 2.29 (Succi, 2002).

$$f_i^{eq} = w_i\rho\left[1 + \frac{3\left(\vec{e_i}\cdot\vec{u}\right)}{c_s^2} + \frac{9\left(\vec{e_i}\cdot\vec{u}\right)^2}{2c_s^4} - \frac{3\left(\vec{u}\cdot\vec{u}\right)}{2c_s^2}\right]. \tag{2.29}$$

Here, the weights w_i are given as $w_0 = 4/9; w_1 = w_2 = w_3 = w_4 = 1/9; w_5 = w_6 = w_7 = w_8 = 1/36$; $\vec{e_i}$ denotes the lattice velocity given as the ratio of the lattice size Δx to lattice timestep Δt; the lattice speed of sound $c_s = \dfrac{\vec{e_i}}{\sqrt{3}}$; the fluid density ρ and the fluid velocity u are macroscopic flow quantities. In this scheme, each particle travels over a single lattice unit at a velocity e in any one of the designated eight directions shown by $0 - 8$ in Fig. 2.1, in which case each velocity can be computed by Eq. 2.30 (Fathi and Akkutlu, 2012). Fig. 2.2 $(a) - (c)$ shows the streaming and collision step for the aforementioned $D2Q9$ discretized velocity scheme.

$$e_i = \begin{cases} (0,0), & i = 0. \\ \left[\cos\frac{(i-1)\pi}{4}\cdot\sin\frac{(i-1)\pi}{4}\right], & i = 1,2,3,4. \\ \sqrt{2}\left[\cos\frac{(i-1)\pi}{4}\cdot\sin\frac{(i-1)\pi}{4}\right], & i = 5,6,7,8. \end{cases} \tag{2.30}$$

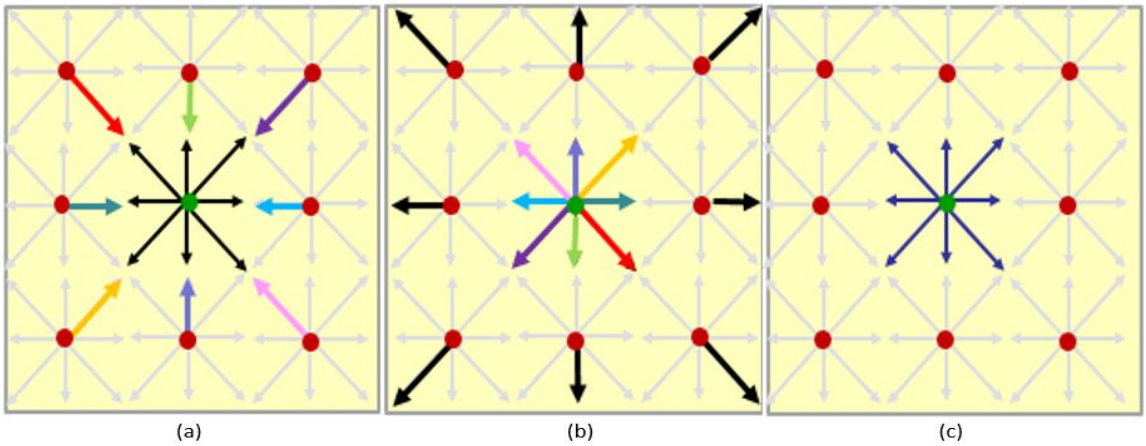

Figure 2.2: (a) Before particle streaming. (b) After particle streaming. (c) Particle relaxation to local equilibrium post collision.

The rest particle positioned at the centre of the lattice possesses zero velocity.

2.3.2.2 MRT Operator

As stated earlier, another class of collision models that can be considered for use in Eq. 2.2 is that proposed by dHumieres (1992) which is the multiple relaxation time (MRT) model. This model transforms the distribution function from the velocity space in the BGK model into a moment space by invoking a transformation matrix that consists of different relaxation times required to relax the various moments to their equilibrium states.

The evolution equation of the MRT model can be expressed in Eq. 2.31 as

$$f_i(x + \vec{e_i}\Delta t, t + \Delta t) - f_i(x, t) = -\mathrm{M}^{-1}\hat{\mathrm{S}}\left[\mathrm{m_i}(x + \vec{e_i}\Delta t, t + \Delta t) - \mathrm{m_i}^{eq}(x, t)\right] \quad (2.31)$$

where m and $\mathrm{m_i}^{eq}$ are column vectors of moments and equilibrium moments respectively of the form, $\mathrm{m} = (\mathrm{m_0}, \mathrm{m_1}, ...\mathrm{m_n})^T$.

$$\mathrm{m} = \mathrm{M}f \quad and \quad \mathrm{m}^{\mathrm{eq}} = \mathrm{M}f^{eq} \tag{2.32}$$

$$\mathrm{M} = \begin{bmatrix} 1 & 1 & 1 & 1 & 1 & 1 & 1 & 1 & 1 \\ -4 & -1 & -1 & -1 & -1 & 2 & 2 & 2 & 2 \\ 4 & -2 & -2 & -2 & -2 & 1 & 1 & 1 & 1 \\ 0 & 1 & 0 & -1 & 0 & 1 & -1 & -1 & 1 \\ 0 & -2 & 0 & 2 & 0 & 1 & -1 & -1 & 1 \\ 0 & 0 & 1 & 0 & -1 & 1 & 1 & -1 & -1 \\ 0 & 0 & -2 & 0 & 2 & 1 & 1 & -1 & -1 \\ 0 & 1 & -1 & 1 & -1 & 0 & 0 & 0 & 0 \\ 0 & 0 & 0 & 0 & 0 & 1 & -1 & 1 & -1 \end{bmatrix} \tag{2.33}$$

$$\mathrm{m} = \begin{bmatrix} \rho, & E, & \hat{\epsilon}, & j_x, & q_x, & j_y, & q_y, & p_{xx}, & p_{xy} \end{bmatrix}^T \tag{2.34}$$

$$\mathrm{S} = diag \begin{bmatrix} s_p & s_E & s_{\hat{\epsilon}} & s_j & s_q & s_j & s_q & s_s & s_s \end{bmatrix}^T \tag{2.35}$$

$$\mathrm{m}^{\mathrm{eq}} = \begin{bmatrix} \rho \\ -2\rho + 3\left(j_x^2 + j_y^2\right) \\ \rho - 3\left(j_x^2 + j_y^2\right) \\ j_x \\ -j_x \\ j_y \\ -j_y \\ \left(j_x^2 - j_y^2\right) \\ j_x j_y \end{bmatrix} \tag{2.36}$$

M represents a transformation matrix, $\hat{\mathrm{S}} = \mathrm{M} \cdot \mathrm{S} \cdot \mathrm{M}^{-1}$ represents a collision matrix while S represents the relaxation time matrix. The velocity and moment spaces can be mapped via linear transformation as seen in Eq. 2.32. For the D2Q9 model, the matrix M, m, S and m^{eq} as expressed by Lallemand and Luo (2000), can be given in Eq. 2.33, Eq. 2.34, Eq. 2.35 and Eq. 2.36 respectively. They are defined by the following macroscopic variables: ρ as the fluid density, $\hat{\epsilon}$ the square of the internal energy E, then j_x, j_y and q_x and q_y representing the mass fluxes and energy fluxes in the x and y directions respectively, while p_{xx} and p_{xy} are the diagonal component and off-diagonal component respectively for the viscous stress tensor. The values of S in Eq. 2.34 used by Mohamad (2011) and defined as $\mathrm{S} = diag\left(1.0, 1.4, 1.4, s_3, 1.2, s_5, 1.2, s_7, s_8\right)$, $s_7 = s_8 = 2/\left(1 + 6\nu\right), s_3 = s_5 = 1.0$, would be used for MRT computations in this work. The density and momentum would be expressed as

$$\rho = \sum_i f_i, \quad j_x = \rho u_x = \sum_i f_i e_{ix}, \quad j_y = \rho u_y = \sum_i f_i e_{iy} \tag{2.37}$$

The different moments would be relaxed at different relaxation times. It should be noted that this model could still be reverted back to the BGK model (Verhaeghe et al., 2009) if $\mathrm{S} = s_\alpha I$ where $s_i = 1/\tau \; \forall \; i = 1...9$. Further details of the MRT method can be found in dHumieres (1992), Lallemand and Luo (2000), Mohamad (2011).

The permeability dependence on the viscosity has in recent times been considered an issue when dealing with the BGK model (Pan et al., 2006, Verhaeghe et al., 2009, Zhang et al., 2013). A suggestion typically given to reduce this effect is to use of the MRT. Regardless, the BGK model still continues to remain very popular amongst several authors (Ansumali and Karlin, 2005, Ansumali et al., 2007, Guo et al., 2007, Homayoon et al., 2011, Sofonea and Sekerka, 2005, Succi, 2002) not only because of its ease of implementation but more importantly its reliability and efficiency. Especially for first order Knudsen correction

(Verhaeghe et al., 2009) in the slip regime which is the focus of this study. Comparisons of both models under no-slip flow conditions have been included in this study just to show the sufficiency of the BGK model in addressing flow considerations of this system.

2.3.3 Dimensional analysis

This is a mathematical method that employs fundamental units of dimension and dimensionless numbers in order to analyse physical parameters that influence fluid flow mechanics. It serves as a good basis for scale modeling of systems with the same geometry. The flow in Eq. 2.5 is governed by the porosity and the following dimensionless parameters: The Reynolds number, Darcy number and viscosity ratio; as shown respectively in Eq. 2.38.

$$Re = \frac{ul}{\nu}; \qquad Da = \frac{k}{l^2}; \qquad J = \frac{\nu_e}{\nu} \tag{2.38}$$

This means if the use of characteristic quantities (Latt, 2008) having a subscript o are employed such that $x_p = l_{o,p}\vec{x_d}$; $t_p = t_{o,p}\vec{t_d}$; $u_p = \frac{l_{o,p}}{t_{o,p}}\vec{u_d}$; $p_p = \left(\rho_o \frac{l_{o,p}^2}{t_{o,p}^2}\right) p_d$; and $\partial t_p = \left(\frac{1}{t_{o,p}}\right) \partial t_d$ Hence Eq. 2.5 becomes

$$\frac{\partial \vec{u_d}}{\partial t_d} + (\vec{u_d} \cdot \nabla_d) \left(\frac{\vec{u_d}}{\phi}\right) + \nabla_d (\phi p_d) - \nu_d \nabla_d^2 \vec{u_d} = \vec{F_d} \tag{2.39}$$

where subscript d and p are dimensionless and physical units respectively, the relationships

$$Re_d = Re_p \qquad Da_d = Da_p \qquad J_d = J_p \tag{2.40}$$

becomes very important in order properly scale the flow behaviour between systems of similar geometry. This will be essential in order to transition from the lattice system to the physical system.

2.3.4 Equation of state

The implementation of the BGK operator in Eq. 2.27 introduces a second order truncation error (He et al., 1998) that is be absorbed by the kinematic viscosity ν as shown in Eq. 2.41.

$$\tau = \frac{\rho\nu}{P} + 0.5, \tag{2.41}$$

where the fluid pressure P would be obtained from the equation of state (EOS). The EOS is a mathematical representation that establishes a relationship between state variables like pressure, volume and temperature in order to describe the state of matter with respect to a set of physical conditions. Studies have shown that the EOS can be incorporated into the LB method by: direct body force which involves addition of an extra term to the distribution function post the collision process (Buick and Greated, 2000, Martys and Chen, 1996) or by velocity-shifting of the equilibrium distribution function (Yuan and Schaefer, 2006). This work will implement the method applied in the latter. From Yuan and Schaefer (2006), this method starts by recalling the equilibrium form of Eq. 2.42 given as

$$\rho(\vec{x},t)\vec{u}(\vec{x},t) = \sum_i \vec{e_i} f_i^{eq}(\vec{x},t) \tag{2.42}$$

Then the macroscopic velocity u will be replaced by Eq. 2.43 such that

$$\vec{u}^{eq}(\vec{x},t) = \vec{u}(\vec{x},t) + \frac{\tau F_{ff}}{\rho(\vec{x},t)} \tag{2.43}$$

where $\frac{\tau F_{ff}}{\rho(\vec{x},t)} = \Delta\vec{u}$ found in Eq. 2.20. Here F_{ff} is the fluid-fluid interaction force between particles and is approximated by Eq. 2.44. Fig. 2.3 showed the particle-particle force of interaction that was accounted for by the EOS.

$$F_{ff}(x) \approx -c_0\psi(x)\, g\nabla\psi(x) \tag{2.44}$$

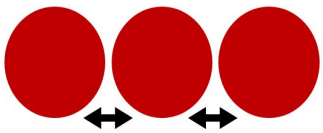

Figure 2.3: Schematic of particles showing fluid-fluid interaction force F_{ff}

g is a temperature dependent variable that controls the intensity of particle interaction and psi is the effective mass and is defined as a function of the local density $\psi(x)$ given by

$$\psi(\rho(x)) = \sqrt{\frac{2P^*}{c_0 g}} \tag{2.45}$$

where P^* is the non-ideal portion of the EOS and is defined as $P^* = P - c_s^2\rho$ with the square of the lattice speed of sound given as $c_s^2 = \frac{1}{3}$. It is clear from Eq. 2.44 and Eq. 2.45, the advantage of this method versus other popular LB phase models (Martys and Chen, 1996, Shan and Chen, 1993) is that the heuristic value g is eliminated and thus rendered inconsequential since a real temperature value is already incorporated via the EOS in the pressure variable (Yuan and Schaefer, 2006). For the $D2Q9$ LB scheme, the gradient term $\nabla\psi(x)$ can be defined using the six-point scheme for the x and y dimensions as

$$\begin{aligned}\frac{\partial\psi(i,j)}{\partial x} &= c_1\left[\psi(i+1,j) - \psi(i-1,j)\right] + \\ &\quad c_2\left[\psi(i+1,j+1) - \psi(i-1,j+1) + \psi(i+1,j-1) - \psi(i-1,j-1)\right]\end{aligned} \tag{2.46a}$$

$$\begin{aligned}\frac{\partial\psi(i,j)}{\partial y} &= c_1\left[\psi(i,j+1) - \psi(i,j-1)\right] + \\ &\quad c_2\left[\psi(i+1,j+1) - \psi(i+1,j-1) + \psi(i-1,j+1) - \psi(i-1,j-1)\right]\end{aligned} \tag{2.46b}$$

where c_1 and c_2 are weighting coefficients for the closest and next-closest nodes related by $c_1 = 4c_2 = \frac{1}{3}$, while $c_0 = 6$. P is the fluid pressure obtained from the typical standard forms of EOS. It can be seen clearly in Eq. 2.45 that the effective mass which controls

the real pressure variation is governed by the choice of EOS implemented. This work implements the ideal gas EOS and the Peng-Robinson EOS formulations. See Yuan and Schaefer (2006) for more detailed study on several other equations of state and their use in LB simulation.

2.3.5 Ideal Gas EOS

Here the fluid pressure is computed as shown in Eq. 2.47

$$P = \hat{\rho} RT \tag{2.47}$$

where $\hat{\rho}$ is the specific density, R is the ideal gas constant and T the temperature (He et al., 1998). The product RT deduced from the choice of lattice speed is given the value of 1/3 on the basis of the equation of state of an ideal gas (Guo and Shu, 2013).

2.3.6 Peng-Robinson EOS

The Peng-Robinson EOS (PR-EOS) calculates the fluid pressure as

$$P = \frac{\hat{\rho} RT}{1 - b\hat{\rho}} - \frac{a\alpha\left(T\right)\hat{\rho}^2}{1 + 2b\hat{\rho} - \left(b\hat{\rho}\right)^2} \tag{2.48}$$

where
$a = \dfrac{0.458R^2T_c^2}{P_c}; b = \dfrac{0.0778RT_c}{P_c}; \alpha\left(T\right) = \left[1 + \left(0.375 + 1.542\hat{\omega} - 0.27\hat{\omega}^2\right)\left(1 - \sqrt{\dfrac{T}{T_c}}\right)\right]^2$
with P_c, T_c and $\hat{\omega}$ representing the critical pressure, temperature and accentric factor respectively of the fluid components. From the theory on *principle of corresponding states*, all fluids show approximately the same level of deviation from ideality when compared at the same reduced temperature and pressure. Based on this theory, the lattice fluid would

be related to the real fluid based on the PR-EOS if Eq. 2.49 is satisfied (Gong et al., 2013).

$$\frac{P^l}{P_c^l} = \frac{P^r}{P_c^r} \quad ; \quad \frac{T^l}{T_c^l} = \frac{T^r}{T_c^r} \quad ; \quad \frac{\hat{\rho}^l}{\hat{\rho}_c^l} = \frac{\hat{\rho}^r}{\hat{\rho}_c^r} \tag{2.49}$$

the subscripts c, l and r represent the critical state, lattice and real fluid respectively. If Eq. 2.49 is satisfied, then analogous to Eq. 2.48 the lattice system should also have the form

$$P^l = \frac{\hat{\rho}^l R^l T^l}{1 - b^l \hat{\rho}^l} - \frac{a^l \alpha^l \left(T^l\right) \left(\hat{\rho}^l\right)^2}{1 + 2b^l \hat{\rho}^l - \left(b^l \hat{\rho}^l\right)^2} \tag{2.50}$$

with $a^l = a^r \dfrac{\left(R^l T_c^l\right)^2 / P_c^l}{\left(R^r T_c^r\right)^2 / P_c^r}$; $b^l = b^r \dfrac{R^l T_c^l / P_c^l}{R^r T_c^r / P_c^r}$; $\rho^l = \rho^r \dfrac{R^r T_c^r / P_c^r}{R^l T_c^l / P_c^l}$;

$\alpha^l \left(T^l\right) = \left[1 + \left(0.375 + 1.542\omega - 0.27\omega^2\right)\left(1 - \sqrt{\dfrac{T^l}{T_c^l}}\right)\right]^2$.

where the values are given as $a^l = 2/49$, $b^l = 2/21$ and $R^l = 1$ to ensure stability and accuracy of the simulation (Yuan and Schaefer, 2006). The desired EOS was applied to Eq. 2.44 and used to calculate F_{ff}.

2.3.7 Boundary Conditions

Accuracy of any fluid flow simulation set-up is typically hinged on proper selection of the boundary conditions. Some boundary formulations used in the LB method and to be implemented here include: bounce-back scheme; mixed boundary scheme; periodic scheme; constant pressure boundary and velocity boundary conditions via the Zou-He boundary scheme (Zou and He, 1997). Focus of this study however shall be on the first two schemes mentioned. The mixed boundary condition scheme comprises of specular-reflection boundary condition and bounceback boundary condition and is typically used to represent the physics of slip flow in the LB methodology (Succi, 2002). When in the continuum regime, the standard bounceback condition is obtained because the slip velocity is approximately zero meaning the slip effect is negligible in this regime. Whereas on

nanochannel capillary walls, the fluid velocity incurs slip on the capillary wall and thus the slip effect is significant and has to be considered. Succi (2002) displayed the relationship of this mixed boundary condition scheme as seen in Eq. 2.51. Where r' and $s = 1 - r'$ are the reflection or bounceback coefficient and slip coefficient respectively with both coefficients ranging from 0 to 1.

$$f_i(x,t) = r' f_{r'}(x,t) + s f_s(x,t). \tag{2.51}$$

The f_s and $f_{r'}$ are the specular portion and bounceback portion of the particle probability distribution function respectively resulting based on the lattice scheme of choice. It can clearly be seen that upon execution of this boundary condition scheme, when $s = 0, r' = 1$, thus the scheme reduces to the standard bounceback condition. This inadvertently means that variation of the extent of the slip effect in the LB boundary condition will be controlled by varying the factor s. Further details of the other aforementioned boundary conditions and their formulations can be found in Mohamad (2011), Sukop and Thorne (2006), Zou and He (1997).

2.4 Knudsen Phenomena

It is well established that one of the key parameters that governs flow in the continuum regime is the Reynold′s number. However for transport at micro and nanoscale with the slip flow regime, the Knudsen number dominates the flow transport (Fathi and Akkutlu, 2012).

$$Kn = \frac{\lambda}{H} = \frac{\nu}{H}\sqrt{\frac{\pi}{2RT}}. \tag{2.52}$$

Eq. 2.52, Eq. 2.53 and Eq. 2.54 show the correction of the single relaxation time to an effective relaxation time τ_{eff} (Suga et al., 2010). This effective relaxation time that

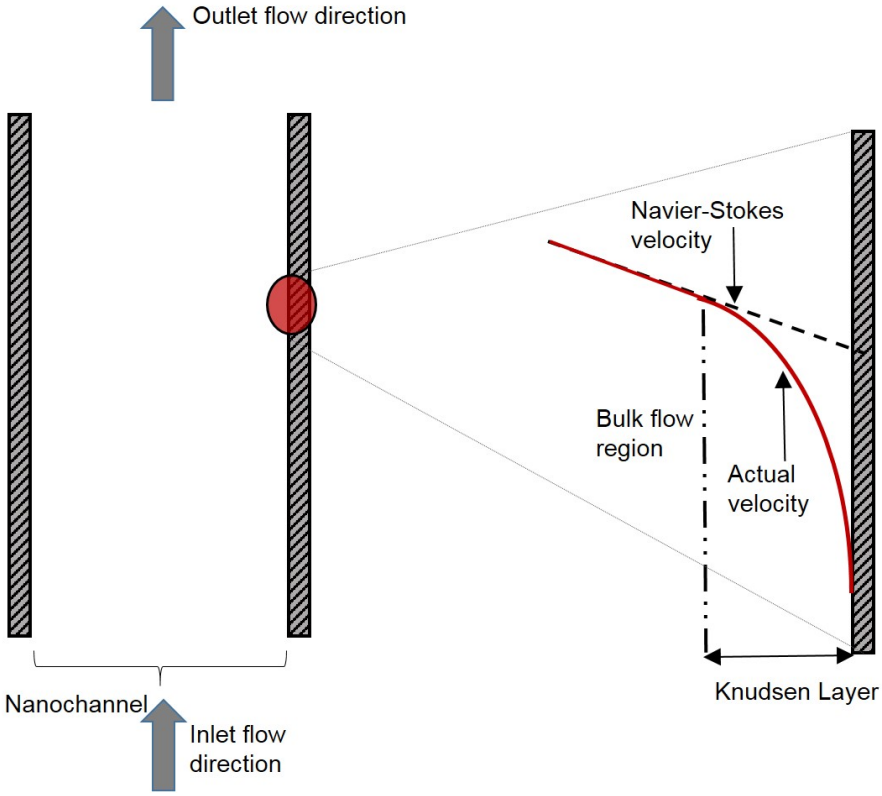

Figure 2.4: Schematic showing Knudsen layer phenomena occurring at the capillary wall [*adapted from Guo et. al.,(2013)*]

tends to vary dynamically as a function of the Knudsen number captures wall effects that could have been ignored in the continuum regime where the relaxation time would have essentially remained constant and mis-representative of the physics at this scale.

$$\tau_{eff} = \tau \cdot \Psi(Kn). \tag{2.53}$$

$$\Psi(Kn) = \frac{2}{\pi} \arctan \sqrt{2} Kn^{-\frac{3}{4}}. \tag{2.54}$$

Fig. 2.4 represents the slip velocity affected by the Knudsen layer phenomena experienced along the capillary wall for which macroscopic properties can be computed. It showed that the actual velocity which is highly non-linear at the Knudsen layer in the flow regime of

such system varies considerably from the macroscopic slip velocity obtained from the extrapolation of the bulk phase Navier-Stokes velocity (Guo and Shu, 2013).

For the capillary walls, a mixed boundary condition scheme was involved comprising of specular-reflection boundary condition and bounceback boundary condition could be implemented to capture this effect (Succi, 2002). When in the continuum regime, the standard bounceback condition is obtained because the slip velocity is approximately zero meaning the slip effect is negligible in this regime. Whereas in nanochannels, the fluid velocity incurs slip on the capillary wall and thus the slip effect is significant and has to be considered. When simulating flow in capillary at this scale, incorporation of the necessary physics of flow by ensuring adequate boundary conditions needs to be employed. The mixed boundary scheme $0 < s < 1$ could be employed to capture this effect and it translates to a Knudsen range of $0 < Kn < 0.18$. Its application and limitations would be reviewed later in the course of this study.

2.5 Molecular Dynamics Simulation

2.5.1 Overview of the MD concept

Molecular dynamics (MD) refers to a computer simulation technique which is a more detailed version of molecular simulation method that computes the motion of a set of interacting particles (atoms, molecules or even constituent forms) (Allen and Tildesley, 1989). Newton's equations of motions are coupled and accurately solved for these interacting particles based on inter-molecular and intra-molecular potentials using several forms of numerical integration schemes (Rapaport, 2004). It's main difference from the Monte Carlo molecular simulation lies in its ability to correctly estimate different configurational properties and dynamic quantities (Haile, 1997). The interactions existent between these particles comprise of complementary close range compression resistant and

particle-binding forces. This is typically represented by potential functions which if chosen appropriately can model the behavior of real substances. The most commonly used form is the 12-6 Lennard-Jones potential

$$U^{LJ}(r) = 4\epsilon\left[\left(\frac{\sigma}{r}\right)^{12} - \left(\frac{\sigma}{r}\right)^{6}\right] \tag{2.55}$$

where r separation between adjacent pair of particles, $U^{LJ}(r)$ is an external potential field, σ defines the length of scale and ϵ represents the interaction strength (Rahman, 1964, Verlet, 1967). For MD, a truncated and shifted potential $U^{tr-sh}(r)$ whose potential vanishes at the cutoff radius r_{cut} is typically used mainly because the intermolecular focus are always finite (Frenkel and Smit, 2002).

$$U^{tr-sh}(r) = \begin{cases} U^{LJ}(r) - U^{LJ}(r_{cut}) & r \leq r_c \\ (0,0) & r > r_{cut}. \end{cases} \tag{2.56}$$

If electrostatic charges happen to be exist in the system under consideration, the adequate Couloumb potentials are included

$$U^{Couloumb}(r) = \frac{1}{4\pi\epsilon_0}\frac{q_i q_j e'^2}{r_{ij}} \tag{2.57}$$

where $i, j \in \{Si, O\}$. The term $U^{Couloumb}(r)$ is the potential energy between the particles i and j, q_i and q_j represent their partial charges and ϵ_0 is the free space permittivity with e' as the elementary charge. The total energy of the system is given by the sum of dispersive(van der Waals) potential, electrostatic potential, bond stretch potential, bond angle potential and dihedral potential interactions (Jorgensen et al., 1996, Le et al., 2016)

$$U^{total} = U^{VDW} + U^{electrostatic} + U^{bond-stretch} + U^{angle-bend} + U^{torsion} \tag{2.58}$$

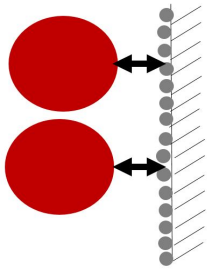

Figure 2.5: Schematic of particles showing solid(grey)-fluid(red) interaction force F_{sf}

U^{VDW} and $U^{electrostatic}$ are defined by the U^{LJ} and $U^{Couloumb}$ respectively. Other intramolecular deformation energy potentials are shown

$$U^{bond-stretch} = \frac{1}{2} K_r \left(r - r_0\right)^2 \tag{2.59}$$

$$U^{angle-bend} = \frac{1}{2} K_\theta \left(\theta - \theta_0\right)^2 \tag{2.60}$$

$$\begin{aligned} U^{torsion} = K_1 \left[1 + cos\left(\phi\right)\right] + K_2 \left[1 - cos\left(2\phi\right)\right] + K_3 \left[1 + cos\left(3\phi\right)\right] \\ + K_4 \left[1 - cos\left(4\phi\right)\right] \end{aligned} \tag{2.61}$$

The standard Lorentz-Berthelot mixing rules from the values obtained from pure compounds were employed to represent non-bonded LJ interactions between different site types i and j.

$$\epsilon_{ij} = \sqrt{\epsilon_{ii}\epsilon_{jj}} \quad \text{and} \quad \sigma_{ij} = \frac{1}{2}\left(\sigma_{ii} + \sigma jj\right) \tag{2.62}$$

For this MD study, two systems of interacting particles shall be modeled: the fluid system and solid system. A schematic of the solid-fluid particle interaction was shown in Fig. 2.5. $n-$octane was the hydrocarbon chosen to be modeled in this study and would thus represent the fluid system. Shale pore structure characterization using SEM and x-ray diffraction(XRD) imagery analysis has shown it's composition to be majorly quartz ($SiO2$),

dolomite ($CaMg(CO3)_2$), aragonite ($CaCO_3$) and clay ($Al_3Si_2O_5(OH)_4$) (Gong et al., 2013). So for this work, quartz in the form of silica was used to represent the shale rock and thus the solid system of particles. Not only because of it's large presence in the rock, but also because it had been commonly used by other researchers (Javadpour, 2009, Le et al., 2015) and thus serves for a good basis for model validation. The MD simulations involved here was executed using the Large-scale Atomic/Molecular Massively Parallel Simulator (LAMMPS) library (Plimpton, 1995) which is an open source molecular dynamics software package. In addition to this library, code development was also complemented with the use of linux and python software packages. The simulations here were performed using facilities from the High Performance Research Computing Center of Texas A&M University. All initial structures were optimized by energy minimization. The equilibration step was done for 2ns with NPT (certain number of particles, pressure and temperature) ensemble and NVT (certain number of particles, volume and temperature canonical). Then the molecular configuration for analyzing the final result was generated over an additional 5ns run.

2.5.2 Static and Thermodynamic Properties

In the past, various attempts had been made to effectively ascertain the phase behavior and static properties of hydrocarbon fluids under confinement. Some were done experimentally (Alfi et al., 2016, Luo et al., 2016), while others via molecular simulation (Jin and Nasrabadi, 2016, Jin et al., 2017). Whereas, this work employs the molecular dynamic approach to do the same study. Properties computed here were the mass density profiles, self-diffusion coefficients and bulk viscosity. The $D_s\,(c)$ in Eq. 2.63 is the self-diffusivity defined by the mobility of tagged particles and would be calculated from the mean-squared

displacement (MSD) (Rapaport, 2004, Wang et al., 2016a)

$$D_s(c) = \lim_{t\to\infty} \frac{1}{6t}\left(\frac{1}{N}\sum_{N} |r(t) - r(0)|^2\right) \tag{2.63}$$

where $r(t)$ is the molecule position at time t, N gives the number of molecules and c the molecular concentration. The equilibrium dynamic viscosity η was computed here by using the equilibrium molecular dynamic (EMD) based on the Green-Kubo formula (Allen and Tildesley, 1989, Mondello and Grest, 1997) by analyzing fluctuations from the off-diagonal components of the pressure tensor in the system.

$$\eta = \frac{V}{k_B T}\int_0^\infty \langle P_{\alpha\beta}(t_0)\, P_{\alpha\beta}(t+t_0)\rangle\, dt \tag{2.64}$$

Where V is the simulation box volume, k_B is the Boltzmann constant, T the temperature, t the time and $P_{\alpha\beta}$ represents the off-diagonal elements for the pressure tensor. The angle brackets represent the pressure tensor time-dependent correlation function, and hence the ensemble average of $\langle P_{\alpha\beta}(t_0)\, P_{\alpha\beta}(t+t_0)\rangle$ for all time regions initialized from t_0 to t (Makrodimitri et al., 2015).

3. CODE DEVELOPMENT AND IMPLEMENTATION

3.1 Benchmark Case - Lid Driven Cavity Flow

A standard LB simulation code was first developed as a base for this study. Code development was done using the Matlab software made available by the Texas A&M High Performance Computing Research. As with most computational fluid dynamics (CFD) programs, the typical lid driven cavity problem was used to validate this code.

A square cavity of 100×100 uniform grid is filled with a hydrocarbon, in this case n-octane. The system is considered isothermal, one side having a tangential velocity of 0.1 at Re of 100, while the rest stay stationary. The lattice scheme used here was the $D2Q9$ scheme. Dirichlet boundary conditions were applied. Values given were in lattice units. The geometric aspect ratio and dimensionless number were matched to those of the real units for proper conversion as stated in previous chapter. Correctly ascertaining the fluid density of the system was the first step. To do this, the average mass density of the domain was preset and initialized using a 0.1% random perturbation for 5000 time-steps (Gong et al., 2013, Yuan and Schaefer, 2006). Temperature was initially set at $298.15K$. The saturated state of the system is achieved after complete coalescence of smaller droplets to get larger ones that represents the liquid until phase equilibrium is met, with the rest of the domain being vapour. This was shown in Fig. 3.1a through 3.1d. Multiple simulations were done at different temperatures using the computed corresponding pressure at that temperature in Eq. 2.45 in order to generate the coexistence curves for the hydrocarbon. The $T - \rho$ plot comparisons are given in Fig. 3.2 and Fig. 3.3 for the reduced and actual values respectively. It can be seen that the LB method showed very good agreement to that from the PR-EOS using Maxwell equal-area construction as well as the experimental values from the National Institute of Science and Technology (NIST) (Lemmon et al.,

2005).

This indicates the ability of the LB method with the PR-EOS to accurately model a single component flow system. Fig. 3.4 shows velocity contours at laminar flow propagating

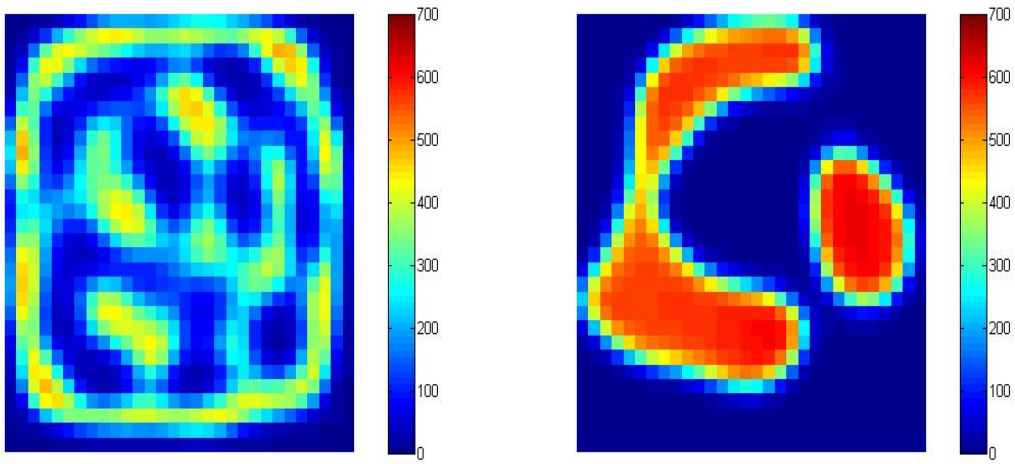

(a)

(b)

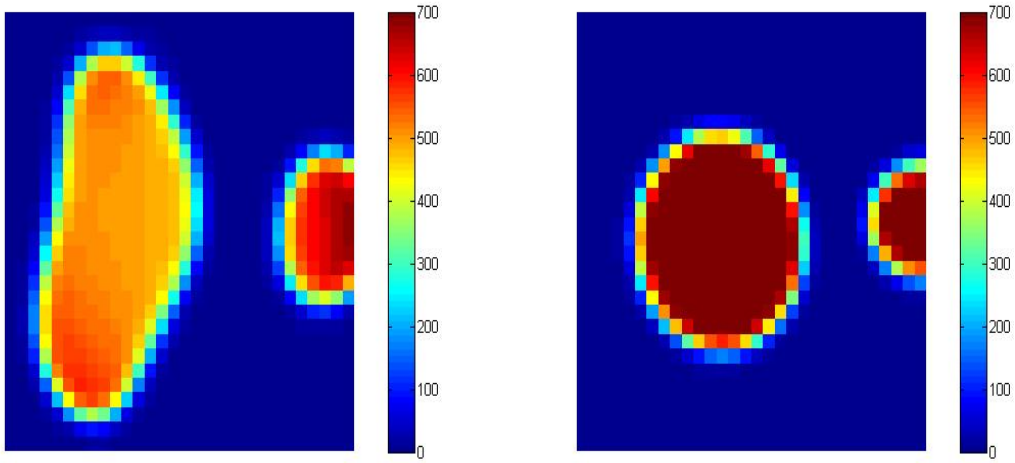

(c)

(d)

Figure 3.1: Simulation snapshots for n-octane density(kg/m^3) distribution after n number of time steps where (a) $n = 40\Delta t$ steps; (b) $n = 120\Delta t$ steps; (c) $n = 200\Delta t$ steps; (d) $n = 400\Delta t$ steps;

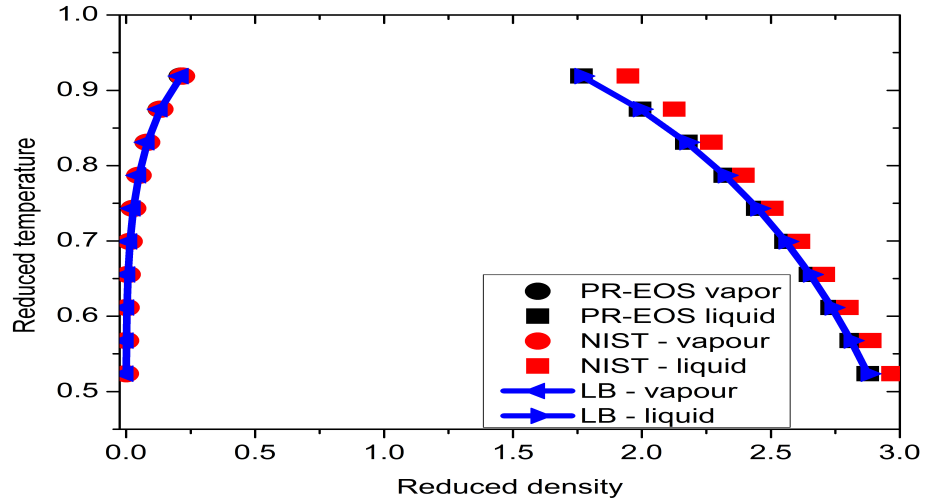

Figure 3.2: Comparison of coexistence curves showing reduced quantities for n-octane with theoretical values and $NIST$ experimental values

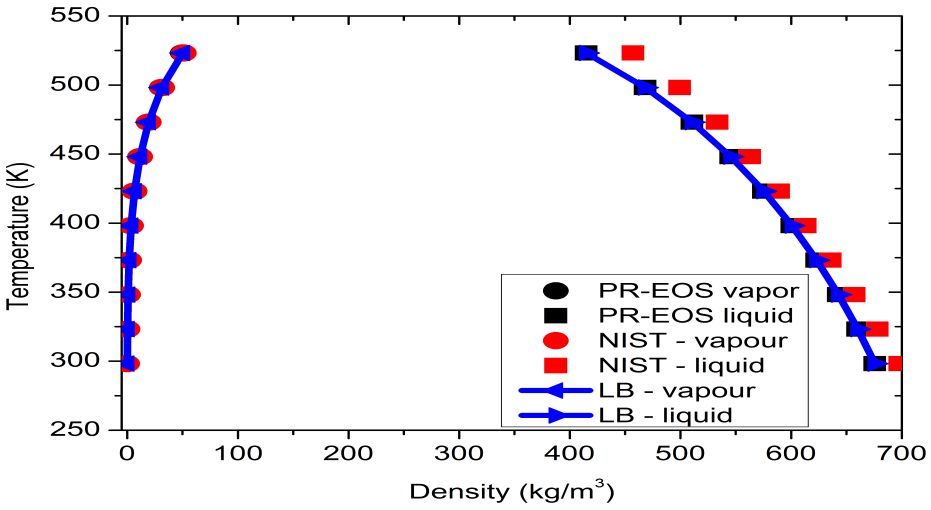

Figure 3.3: Comparison of coexistence curves for n-octane with theoretical values and $NIST$ experimental values

from the moving boundary. When the dimensionless velocity u_d was plotted along the midsection $x_d = 0.5$, a very good agreement was observed to exist when compared to the analytical solution from Ghia et al. (1982). This was shown in Fig. 3.5

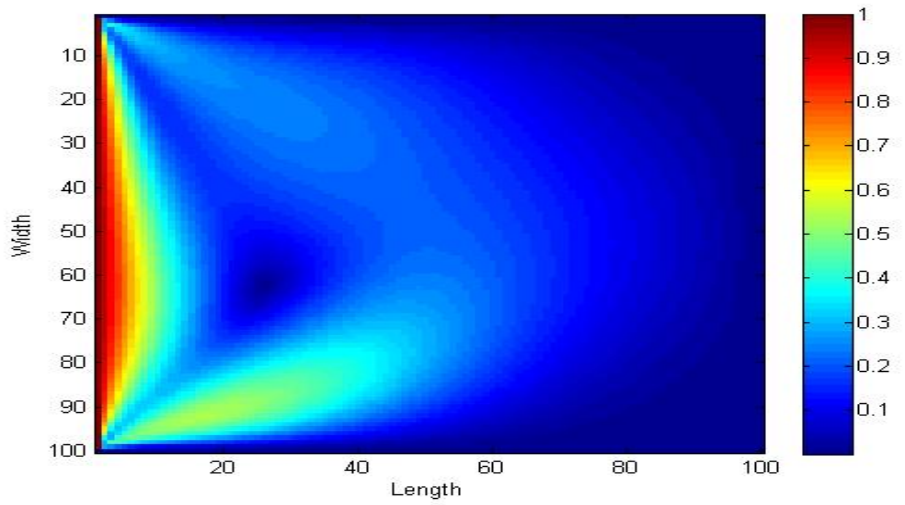

Figure 3.4: Dimensionless velocity field of n-octane flow across 100×100 grid at $Re = 100$

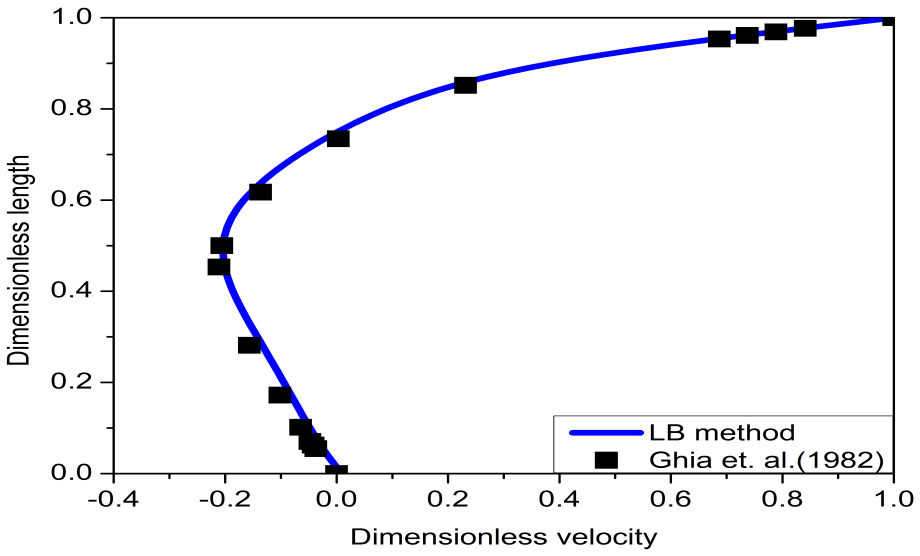

Figure 3.5: Dimensionless velocity profile of n-octane at midsection and mid-height of cavity at $Re = 100$

3.2 Computation of Permeability in porous media

Pore-scale modeling has the ability to predict flow properties by using a topologically disordered pore network model that provides a realistic representation of the rock sample geology. This network could be generated via stochastic methods, micro-CT scanning or even direct imaging techniques. The LB method has proven to have the ability to model petrophysical properties in porous media (Aksnes and Elster, 2009, Chen and Doolen, 1998, Rothman and Zaleski, 1997, Succi, 2002). Permeability is one of such parameters. The porous media here would comprise of two networks: The Pore distribution(PD) network and the Rock distribution(RD) network. This was generated by discretization and conversion of 2D micro-CT and SEM images into binary images whose position vector $\vec{x}$ could be defined by Eq. 3.1.

$$I\left(\vec{x}\right) = \left(\begin{array}{lll} 0 & for & \vec{x} \in PD \\ 1 & for & \vec{x} \in RD \end{array} \right) for \quad \vec{x} = x_i, x_j = 0, 1, ...N_i - 1; 0, 1, ...N_j - 1 \quad (3.1)$$

The permeability can be estimated straight from the rate flux or velocity fields generated from the LB method in conjunction with Darcy's law for the fluid under consideration. Fig. 3.6 shows the procedure used in the simulation model for the permeability calculations of the digitized porous media generated in this study. Here, an external force F_{dpdl} was added to the standard LB simulation model (comprising the initialization, collision and streaming steps) as representation of the total pressure drop along the system length $\frac{\triangle P}{L}$ and expected to cause the same change in momentum as the latter. The average macroscopic velocity was then retrieved and compared to that of the initial time step dependent. The permeability was calculated when the velocity field was at steady state, thus achieving convergence. The system converged when the change in average velocity calculated between iterations was less than the tolerance value $tol = 10^{-10}$ in lattice-units.

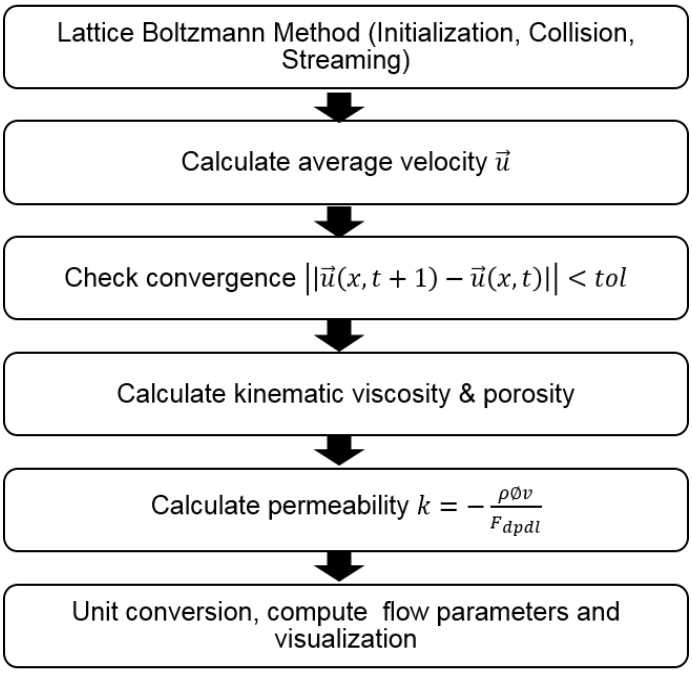

Figure 3.6: Procedure for permeability simulation model using the lattice Boltzmann method

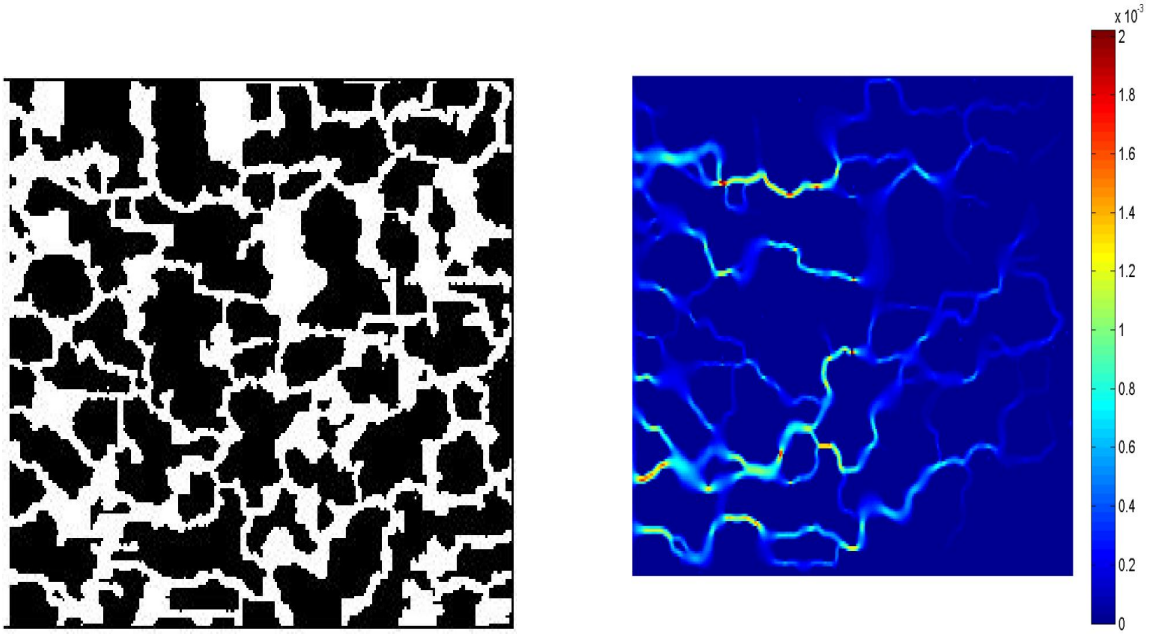

(a) (b)

Figure 3.7: (a) Pore distribution in 2D domain for Berea sandstone; (b) Velocity distribution in 2D domain for Berea sandstone

In order to validate the effectiveness of this permeability calculation procedure for this work, the Berea dataset (Blunt et al., 2013, Boek, 2010, Dong, 2008, Oren and Stig, 2003) with an already known average permeability of 1286 mD was used. This dataset is a representation of the sandstone found in Berea, Ohio. It contains small portions of dolomites, feldspars and clays, thus is popularly used for core analysis (Dong, 2008). Since this code was written in 2D, a random slice from the 3D lattice size was taken, as shown in Fig. 3.7a. The external force was applied in the x-direction and y-direction as $F_x = F_{dpdl}$ and $F_y = 0$ respectively. Upon execution of the simulation, the steady state velocity fields are shown in Fig. 3.7b, the flow under consideration here was at low Re. The velocity field showed the fluid flow direction as it percolates through the pore network domain. Results shown in Fig. 3.8 reflect a good match for the different pressure drop values tested with the code for this work. An average permeability of 1323 mD was obtained.

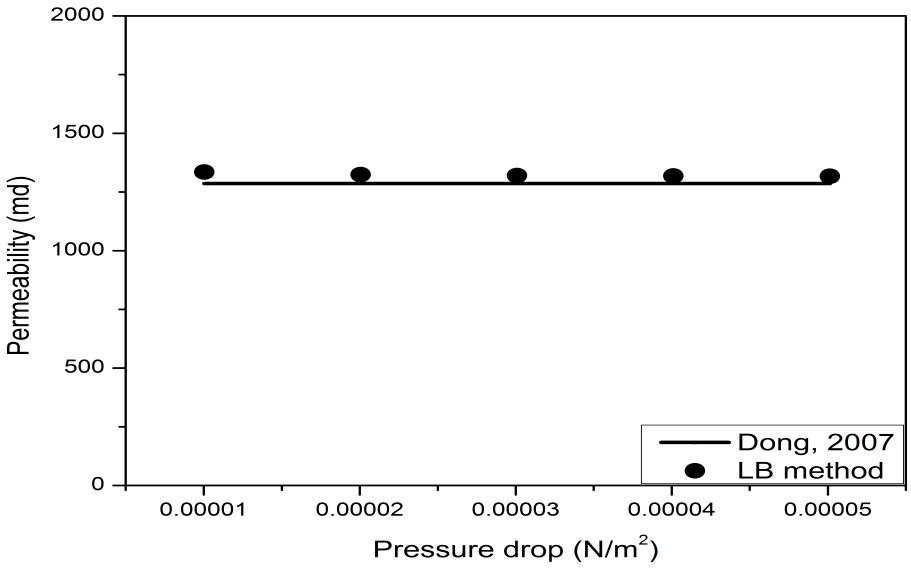

Figure 3.8: Permeability calculated at different pressure drop values for the Berea sandstone dataset

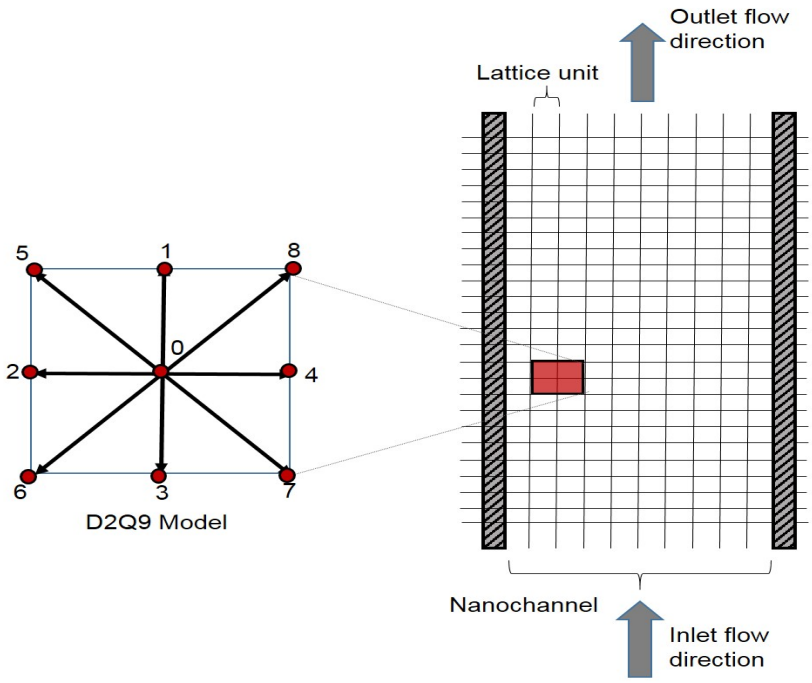

Figure 3.9: Schematic of D2Q9 lattice scheme displaying lattice geometry in capillary nanochannel [*adapted from Fathi et. al, (2012)*]

The relative error was 2.87%. This permeability procedure was later modified and used to perform diagnositics on different test cases to compute the apparent permeability values for the digitized structure of the pore network distributions in this work.

3.3 Hydrocarbon flow in nanochannel considerations

With the verified base LB set-up, flow dynamics in nanochannels under confinement conditions typical of the pore size of a tight rock matrix was investigated. This system is analogous to experimental flow between parallel plates. In order to show this flow concept at varying conditions, a lattice grid that was representative of this system had to be initialized as displayed in Fig. 3.9. This was instantiated by defining a two dimensional grid to accommodate the $D2Q9$ LB scheme employed for tis study. System condition

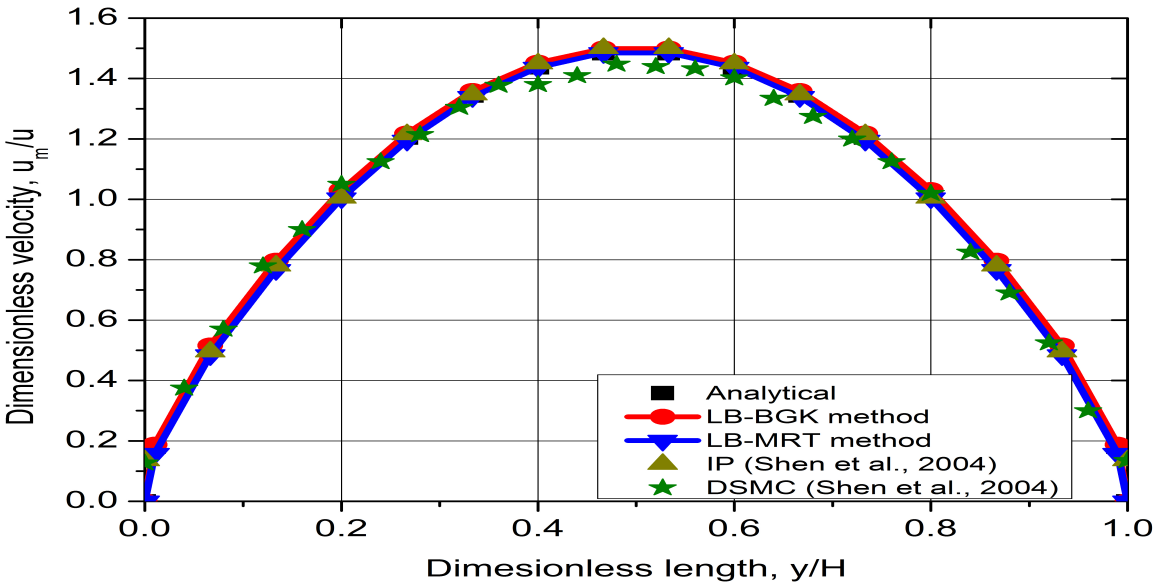

Figure 3.10: Comparison of normalized velocity profile of gas flow across nanochannel for analytical, LB-BGK, LB-MRT, IP and DSMC solutions at $Kn = 0.0194$

was kept isothermal at $298.15K$ for the n-octane having a capillary length by width of $40nm \times 20nm$. For the simulation, the relaxation frequency, pressure drop and channel width parameters used here were all defined in lattice units as 0.5, 0.0125 and 20 respectively. A two lattice unit layer buffer on each side of the capillary nanochannel was also accounted for. Upon execution of the simulation, the standard LB method(BGK) was compared with the LB-MRT, analytical Hagen-Poiseuille equation of fluid flow between parallel plates,the LB multiple relaxation time method (Lallemand and Luo, 2000), and both information preservation method(IP) and direct simulation Monte Carlo (DSMC) which are both numerical solutions $(Kn = 0.0194)$ by Shen et al. (2004) as shown in Fig. 3.10. At the system wall, the mixed boundary condition reformulated to the bounceback condition ($s = 0$) was employed. Very good agreement was achieved between the LB-BGK method used in this study and other numerical solutions in Fig. 3.10. The maximum

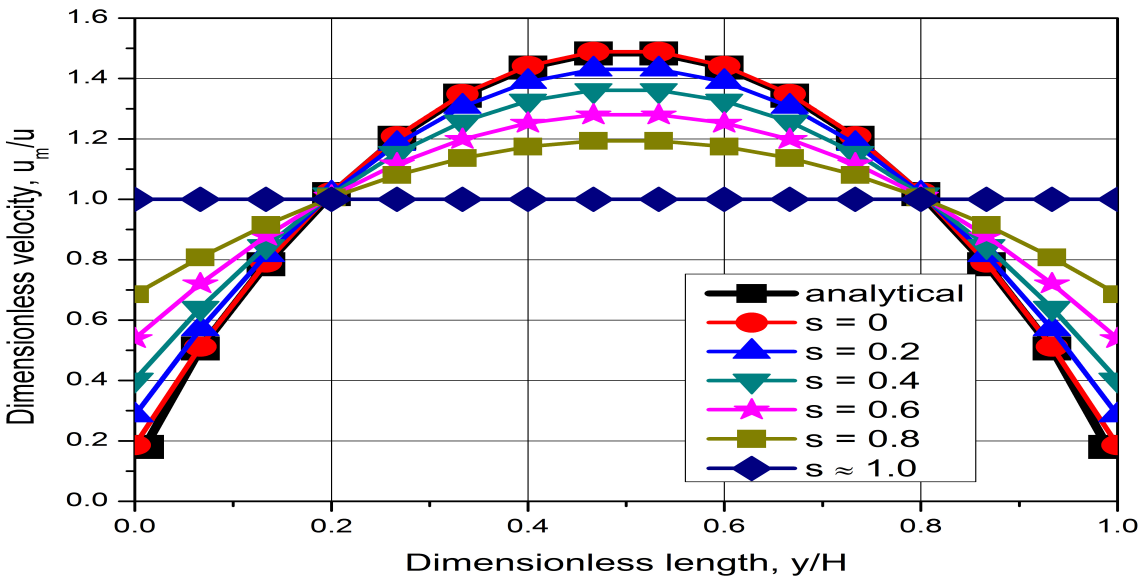

Figure 3.11: Normalized velocity profile of gas flow across nanochannel for various slip coefficients

dimensionless velocity of 1.5 was achieved at the center line axis of the nanochannel. This is consistent with the theoretical derivation of the ratio of the maximum velocity to that of the average velocity in the slip regime. Once this had been established, the slip coefficients were introduced into the system. This consisted mainly of specular and bounceback parameters in order to obtain the required slip velocities existent at the boundaries. The slip coefficient was varied from typical fluid flow displaying no slip to fluid flow displaying full slip, as can be seen in Fig. 3.11. This denotes the slip regime expressed as a variation in the Knudsen criterion which has a direct relationship with the slip coefficient. Velocity profile comparison with theoretical solution was done only at the bounceback condition here. Mainly because this was the only theoretically validated solution for velocity profile under the slip flow regime that ws found during the course of this study. When $s = 0$, a parabolic velocity profile is sustained akin of any fluid undergoing the Hagen-Poiseulle

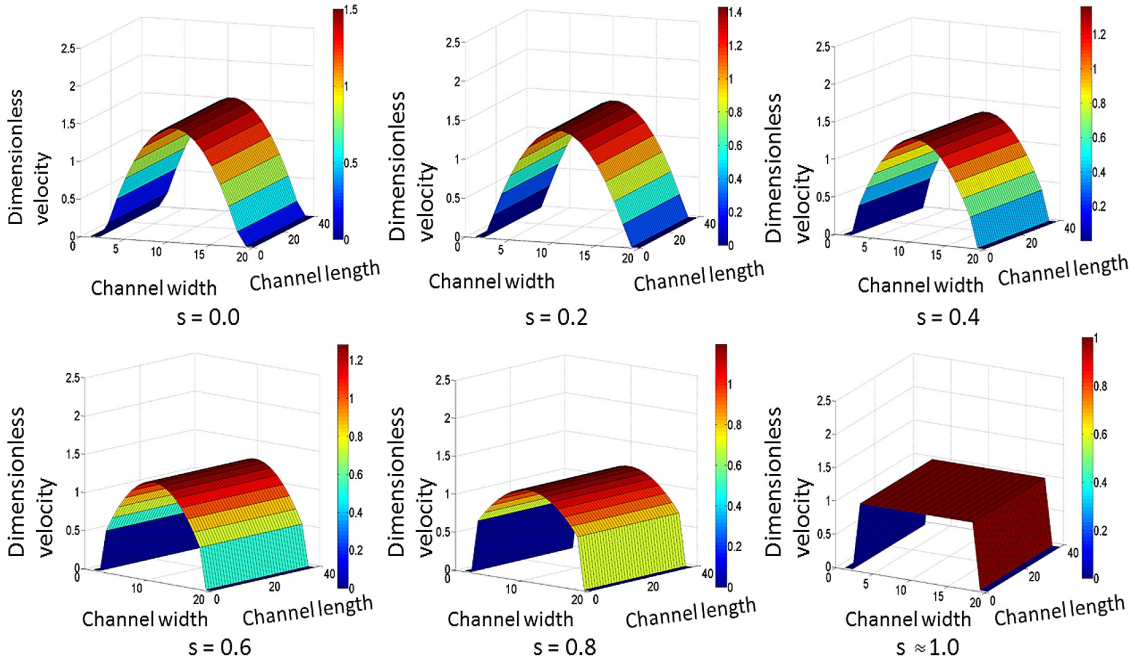

Figure 3.12: Surface plots showing normalized velocity profile of gas flow in the nanochannel for various slip coefficients

flow stemming from the fluid flow assumption of the continuum regime. However as the slip coefficient increases, the velocity profile starts to exhibit curvature inversion at the flow front and consequently transitions into a planar profile. A clearer view of how the flow would transition in a three dimensional rendition of the channel can be seen in Fig. 3.12. Further scrutiny of this regime showed that upon reaching a certain critical slip coefficient s_c with a value of $Kn \sim 0.155$, indefinite slip motion in the simulation system is invoked (Madiebo et al., 2017). The term indefinite here describes a time scale significantly larger than the fluid chemical scale instantiated at the initial stage of the lattice simulation model set-up. This is very analogous to what is known as the glassy behavior or non-vanishing slip flow of gas in the slip flow regime (Succi, 2002). The occurrence of this phenomena which would henceforth be identified as the critical slip coefficient, causes

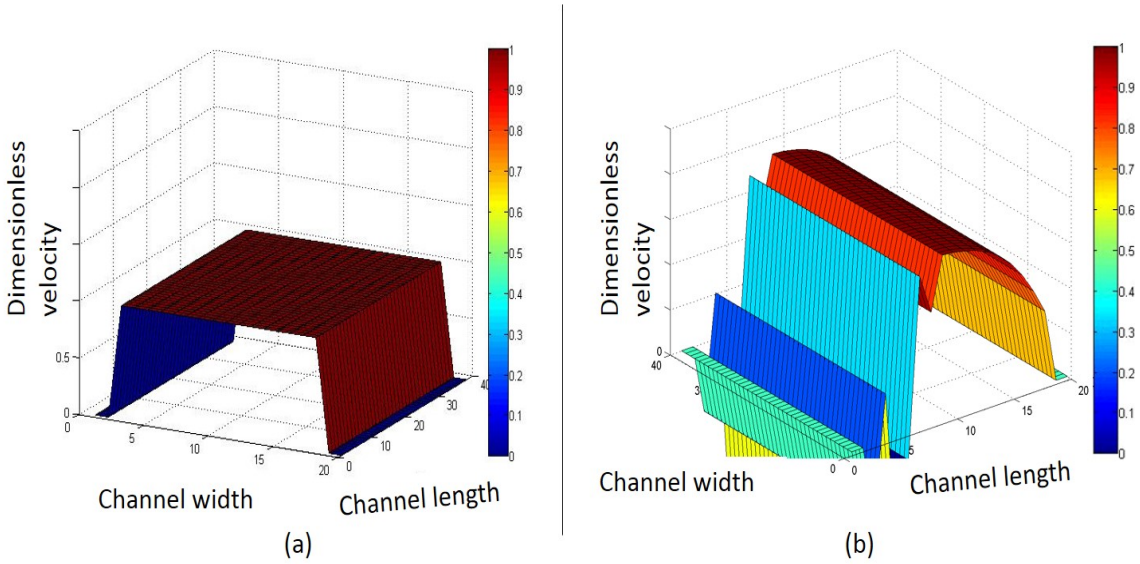

Figure 3.13: Surface plots showing normalized velocity profile instability. (a) $Kn \approx 0.155$ (b) $Kn > 0.155$

a very significant increase and even unstable nature of the velocity profile as shown in Fig. 3.13. It should be stated that this entire study was done at a fixed channel width. However, there have been studies that have shown that an increase in the channel width will cause an increase in the maximum velocity (Madiebo et al., 2017, Zhang et al., 2014). Subsequently, it will lead to an increment in velocity arising from the inclusion of the Knudsen criterion which conversely becomes more important with decreased channel width. It is noteworthy to highlight that this critical slip coefficient s_c occurs just before the limit of the maximum slip coefficient $(s_c = 1)$ was met. This stipulates that a measure of uncertainty will be present when computing the apparent permeability from this critical regime and thus should be addressed. Hence when implementing LB simulation involving mixed boundary conditions, high confidence should be considered for volumetric flux values calculated in the slip regime before the critical slip coefficient and not beyond. This serves as a limitation of this procedure if applied to a tight rock matrix. Simply because the diverse

spectra of scale in a heterogeneous tight rock displaying nanometric pore sizes, would cause flow to continuously translate through Knudsen flow regimes even higher than that of the slip flow as shown much earlier in Fig. 1.1. In addition, the flow computed with the LB method assumes a linear relationship between the fluid density and the rock-fluid interaction force. This is assumption evidently becomes highly questionable especially since its a function of pore size dependence (Gong et al., 2013). Which means the smaller the pore, the more pronounced the molecular interactions would be, and thus the less likely this holds true. To address these issues, a different approach to represent this mixed boundary condition had to be employed. It involved a more definite computation of the rock-fluid interaction force via molecular dynamics for the system under consideration.

4.1 Model for n-octane and atomistic force fields

The united-atom (UA) concept based on the methyl (CH_3) and ethyl (CH_2) was used to model the $n-$octane molecules which reduces computational costs but still maintains its accuracy. This was shown in Fig. 4.1a. The forcefield employed here was the Transferable Potential for Phase Equilibria (TraPPE) (Martin and Siepmann, 1998). The TraPPE-UA force field produced realistic predictions of $n-$octane behavior. The hydrocarbon model was described by bond stretching, angle bending and dihedral constraints. A cut-off radius of 12 Å. was used for the Lorentz-Berthelot combining rules (Wang et al., 2016b, Yang and Zhong, 2006). It had no partial charges. The bond length was set as 1.54 Å. The bond angle was set as 114° and described based on a harmonic potential. The dihedral angles were described based on the Optimized Potentials for Liquid Simulations for united atoms (OPLS-UA) torsional potential.

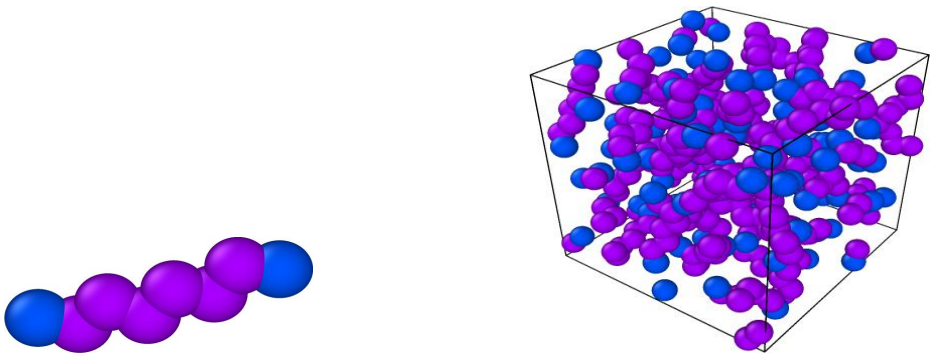

(a) (b)

Figure 4.1: (a) United-Atom model for n-octane. Atom color code: blue and purple, methyl($-CH_3$) and methylene($-CH_2$) groups respectively; (b) Three-dimensional simulation cell with 48 n-octane molecules

atom	$\epsilon/k_B\,(K)$	σ(Å)	$q\,(e)$
CH_3	98	3.75	0
CH_2	46	3.95	0

Table 4.1: Force field parameters for n-octane.

Some other required parameters can be found in table 4.1. The simulation box is made up of 432 unit cells $(4 \times 12 \times 9)$ as shown in Fig. 4.1b. For this simulation, a $1fs$ integration time step was used in the velocity verlet algorithm to integrate the equations of motion (Allen and Tildesley, 1989). Temperature was maintained constant by using a Nosé-Hoover thermostat at a relaxation time of $0.1ps$. The system was run for $2ns$ in the NPT ensemble to achieve equilibration, and then trajectories for the next $5ns$ was collected for result analysis. MD simulations were executed fort he n-octane at various temperature conditions. Fig. 4.2 and Fig. 4.3 showed the density and viscosity values of this work respectively in comparison to the NIST database (Lemmon et al., 2005). The MD den-

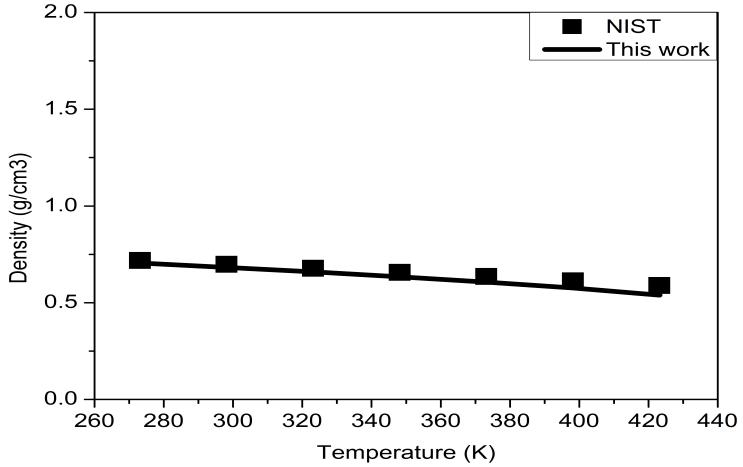

Figure 4.2: Comparison of n-octane density with experimental NIST data at different temperatures

sity and viscosity predictions showed good agreement with the NIST data for the 1 MPa pressure at various temperatures. The density tends to gradually decrease with increasing temperature. On the other-hand, viscosity tends to decrease as the temperature increases.

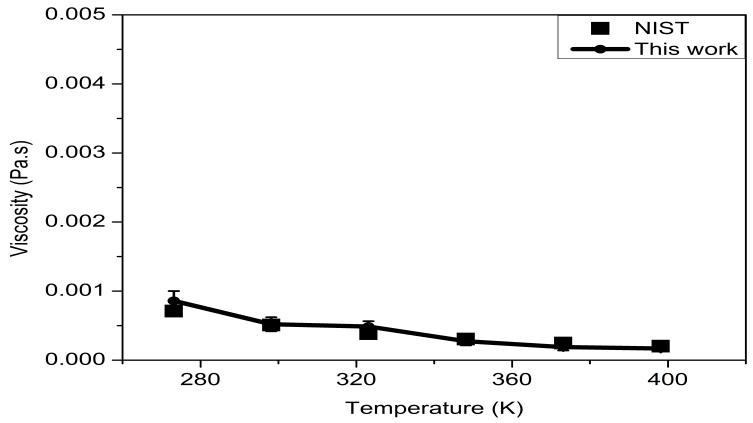

Figure 4.3: Comparison of n-octane viscosity with experimental NIST data at different temperatures

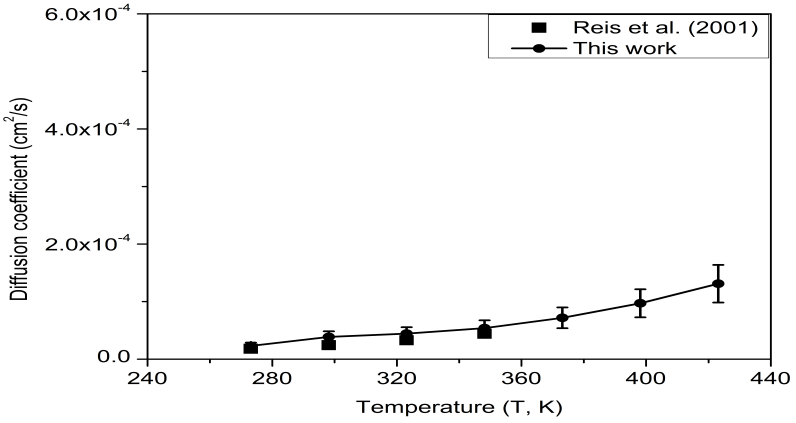

Figure 4.4: n-octane diffusion coefficients simulated at different temperatures

$T\,(K)$	$\rho\,(g/cm^3)$-NIST.	$\rho\,(g/cm^3)$
273.15	0.718	0.706
298.15	0.698	0.682
323.15	0.678	0.660
348.15	0.657	0.634
373.15	0.635	0.606
398.15	0.613	0.576
423.15	0.589	0.539

Table 4.2: Comparison of NIST data and simulation density values for n-octane at different temperatures.

$T\,(K)$	$\eta\,(Pa.s) \times 10^{-3}$-NIST.	$\eta\,(Pa.s)$
273.15	0.710	0.858 ± 0.14
298.15	0.509	0.520 ± 0.1
323.15	0.384	0.487 ± 0.08
348.15	0.305	0.275 ± 0.06
373.15	0.247	0.189 ± 0.05
398.15	0.203	0.169 ± 0.04

Table 4.3: Comparison of NIST data and simulation viscosities for n-octane at different temperatures.

Computed MD self-diffusion coefficients were also compared with experimental values from Reis et al. (2001) and shown in Fig. 4.4. The diffusion coefficient exhibited a direct proportionality relationship with the temperature. A good match with the experimental data was also observed. Numerical values of the density, viscosity and diffusion-coefficient values were shown in Table 4.2, 4.3 and 4.4 respectively. Average deviations between the experimental values (NIST) and the measured MD values was about 5% for of all computed properties.

$T\,(K)$	$D_s\,(cm^2/s \times 10^{-4})$-Expt.	$D_s\,(cm^2/s \times 10^{-4})$
273.15	0.181	0.172 ± 0.06
298.15	0.243	0.29 ± 0.1
323.15	0.327	0.333 ± 0.11
348.15	0.441	0.405 ± 0.14
373.15	-	0.539 ± 0.18
398.15	-	0.728 ± 0.24
423.15	-	0.981 ± 0.32

Table 4.4: Diffusion coefficients obtained for n-octane at different temperatures.

4.2 Model for silica and atomistic force fields

The silica used in this study to represent the nanochannel was modeled using a short-range Buckingham potential shown in Eq. 4.1, in conjunction with a long-ranged Couloumbic potential. This model was chosen because of its popular usage by other researchers in studying structural properties of glass and shale under various conditions (Le et al., 2015, van Beest et al., April 16, 1990). The energy obtained from this potential can be calculated from the expression in Eq. 4.2

$$U^{Buckingham} = A_{ij}e^{-B_{ij}r_{ij}} - \frac{C_{ij}}{r_{ij}^6} \tag{4.1}$$

$$U\,(r) = U^{Buckingham} + U^{Couloumb} \tag{4.2}$$

where A_{ij}, B_{ij} and C_{ij} are pair potential constants. Values of these constants that would be necessary to reproduce the energies needed to pair silica clusters have been obtained from the studies by Sanders et al. (1984) and Hill and Sauer (1994) and is shown in table 4.5. The partial charges were $q_O = -1.2$ and $q_{Si} = +2.4$. Fig. 4.5 showed the silica structure with two slabs on both sides separated by a $4.37nm$ spacing. See Le et al. (2016), Le Page and Donnay (1976), van Beest et al. (April 16, 1990), Wang et al. (2016a,b) for

more details on the formulation of this structure.

i-j atoms	A (eV)	B (Å^{-1})	C (eV Å^6)
O - O	1388.773	2.760	175.000
Si - O	18003.757	4.873	133.538
Si - Si	0	0	0

Table 4.5: Force field parameters for silica

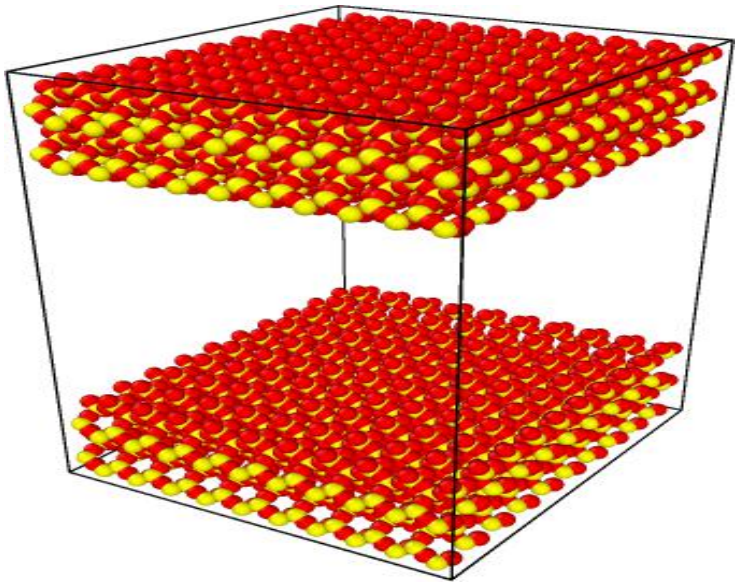

Figure 4.5: Molecular dynamic model of silica system. $L_x = 5.32nm$, $L_y = 4.93nm$, $Lz = 6.57nm$. Si (yellow atom) and O (red atom)

4.3 Silica +n-octane model formulation

When it comes to shale rock, research on imbibition has shown that such rocks have a higher affinity to oleic phases with the capillary pressure obtained via the Young's-Laplace model being lesser than the force that actually translates the oil through its pores (Wang

et al., 2016b). The reason behind this stems from the hydrocarbon adsorption onto the shale rock surface. To gain insight on this adsorption effect caused by confinement of the hydrocarbon in nanopores, the transport properties of the n-octane through the silica nanochannel system were studied by running the NVT simulation for 6 ns post equilibration as stated earlier. Periodic boundary conditions were maintained in the x and y direction for the $5.32nm \times 4.93nm \times 6.57nm$ box, as shown in Fig. 4.6. A CHARMM forcefield was employed to account for the intermolecular interactions between different phase molecules (Cruz-Chu et al., 2006). The cut-off radius selected here was 12Å (Wang et al., 2016b). The density profile based on the center-of-mass of alkane and perpendicular to the z dimension of the structure was computed, with the local mass density also determined. Fig. 4.7 shows this density profile distribution from this simulation at $298.15K$. The nanochannel width, measured as length between substrate slabs under consideration, was given as $4.37nm$. It is evident that the density profiles of the n-octane molecules shows prominent oscillatory behaviour near the silica substrate walls and alot less pro-

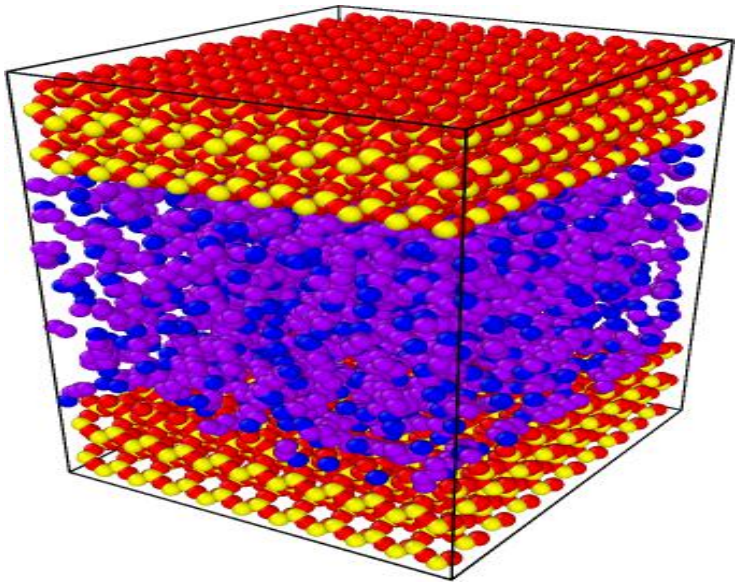

Figure 4.6: Molecular dynamic model of Silica + n-Octane system

nounced at the central $z - axis$ plane as it moves farther away from the substrate. It gradually approaches the bulk n-octane density simulation value $0.68g/cm^3$ which is close to the experimental NIST value of $0.693g/cm^3$ (Lemmon et al., 2005). The oscillation would diminish more and become even more bulk-like in the center plane as the channel width increases (Wang et al., 2016a). Fig. 4.8 showed the mass density profile variations predicted by the MD model for various temperatures.

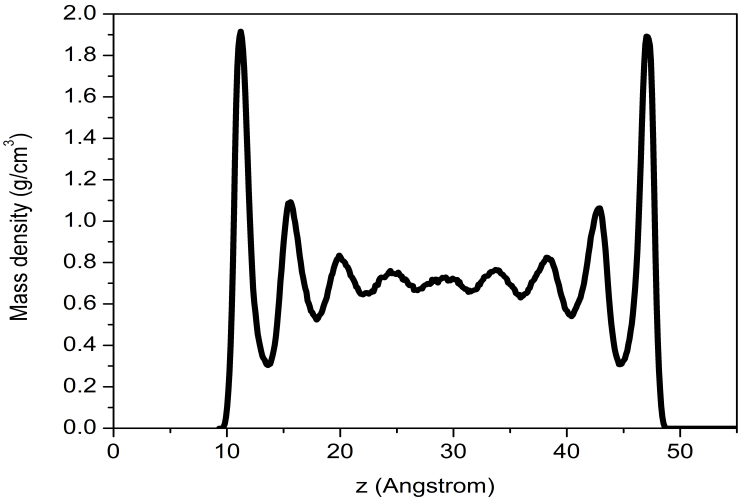

Figure 4.7: Silica + n-octane mass density profile at $T = 298.15K$

The pore size also plays a key role in affecting the diffusion in pores. As pore size increases the density of the hydrocarbon molecules would decrease because the molecules would be adsorbed into the relatively larger pores of the pore surface. This pore size effect on diffusion as a result of confinement is evident in Fig. 4.9. The smaller the channel width, $4nm$ in this case, the more hydrocarbon molecules were adsorbed on the contact surface which leads to the a reduction in the diffusivity rate at that temperature. It is also worth

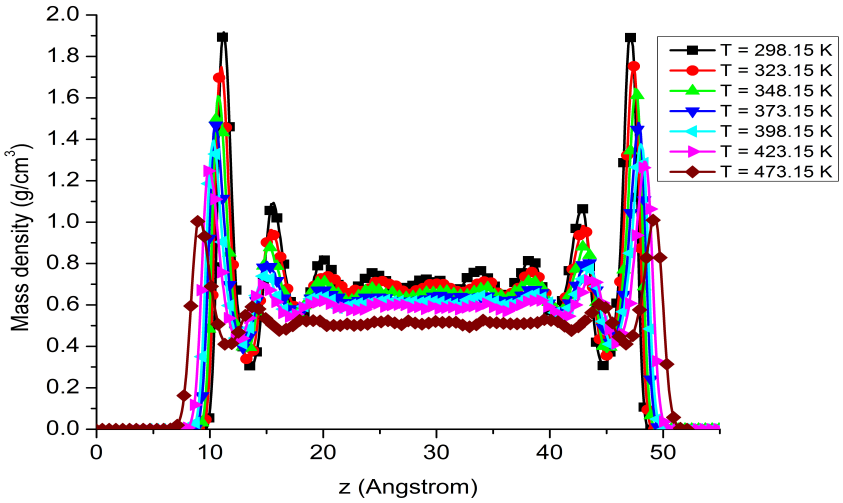

Figure 4.8: Silica + n-octane mass density profile at different temperatures

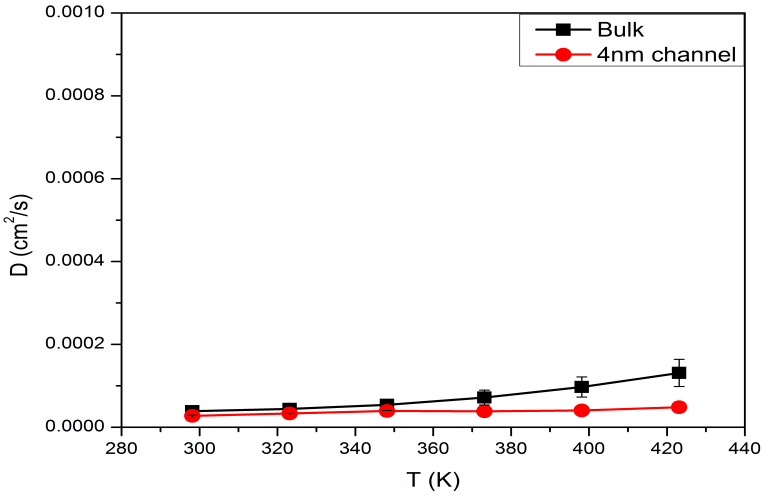

Figure 4.9: Silica + n-octane diffusion coefficients at different temperatures

noting that even as the temperature was increased, the rate of increase in the diffusivity rate was alot faster in the bulk phase than it was in the $4nm$ channel.

5. LATTICE BOLTZMANN - MOLECULAR DYNAMICS (LBMD) MODEL APPLICATION

5.1 Molecular Dynamics Force Computation

After the MD simulation model had reached equlibrium, the force of interaction between the silica and the n-octane particles was also computed during the post equilibration run for data analysis. Fig. 5.1a shows two-dimensional view of the pore channel where the hydrocarbon interacts with the boundary structure.

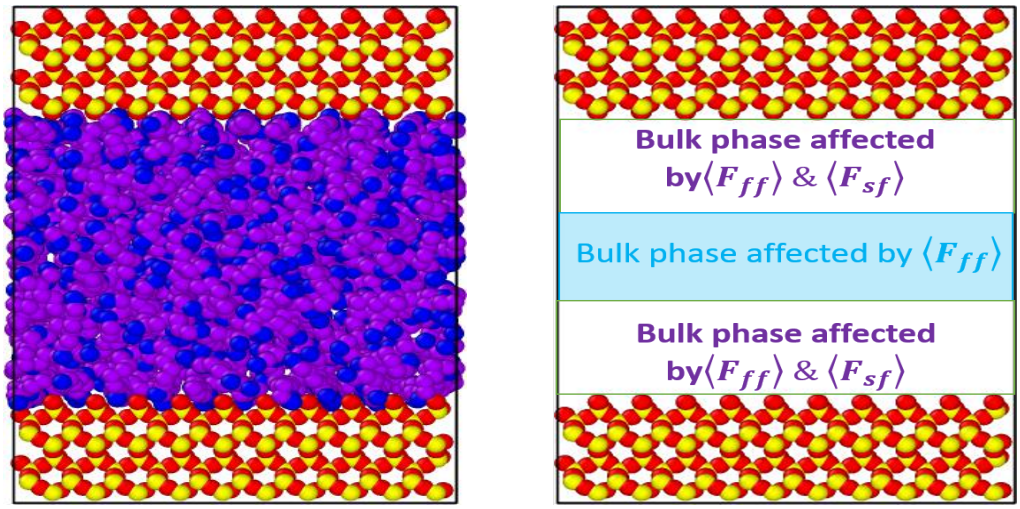

(a) (b)

Figure 5.1: (a) A simulation snapshot showing n-octane flowing through a $4.37nm$ pore channel (b) Force of interactions F_{ff} and F_{sf} existent between individual hydrocarbon particles and hydrocarbon particles and the boundary respectively

From Fig. 5.1b, it can be seen that the distance between the center fluid region and the boundary wall exceeded the cut-off radius of 12 Å, thus the n-octane molecules in this region can be considered to only be affected by the intraparticle potential F_{ff}. Whereas in

the regions closer to the boundary, the n-octane molecules were considered to be affected by both F_{ff} and F_{sf} functions. F_{ff} would already be accounted for via the EOS. In order to compute F_{sf}, the particle-boundary MD force of interaction F_{md} would need to be determined as $F_{sf} = f(F_{md})$. This was calculated directly based on the prevailing 12-6 LJ potential in Eq.2.55. This calculation could be translated directly into the LB model as follows:

Recalling Eq.2.55

$$U^{LJ}(r) = 4\epsilon\left[\left(\frac{\sigma}{r}\right)^{12} - \left(\frac{\sigma}{r}\right)^{6}\right] \quad ; \quad r < r_c \tag{5.1}$$

r is the particle to wall distance whereas r_c is the cut-off distance beyond which the particle-wall interaction ceases. r_c would be approximated to equate the skin molecular mean free path λ of the n-octane molecules. From this Eq. 5.1, it is evident that U^{LJ} has an inverse relationship with the function of r. Hence, let's assume a simple relationship between these two parameters such that $U^{LJ} \propto \frac{1}{r}$. Also recall from the definition of Kn that it is a function of λ. Now λ is the average distance a particle would travel in order to interact or collide with another particle within a fluid system. Since r is the distance the fluid particle would need to travel to collide with the wall particle and so long as it does not exceed λ in the vacuum range (See Jennings (1988) for $\lambda_{ambient}$ values), a simplifying assumption can be made such that $r \approx \lambda$. Thus for a particle-wall interaction experiencing a potential along a surface area A, the following expression for the potential per unit area could be generated

$$\frac{U^{LJ}}{A} \propto \frac{1}{\lambda} \tag{5.2}$$

$$\frac{U^{LJ}\lambda}{A} = C(\lambda) \tag{5.3}$$

where C is a system constant for the defined λ. This means for different values of λ

$$\frac{U_1^{LJ}\lambda_1}{A_1} \quad , \quad \frac{U_2^{LJ}\lambda_2}{A_2} \quad , \quad \frac{U_3^{LJ}\lambda_3}{A_3} \quad , \quad \cdots \quad , \quad \frac{U_c^{LJ}\lambda_c}{A_c} \tag{5.4}$$

λ_c is the cut-off distance analogous to r_c. If Eq. 5.4 is divided by the limiting function, it becomes

$$\frac{U_1^{LJ}\lambda_1 A_c}{U_c^{LJ}\lambda_c A_1} \quad , \quad \frac{U_2^{LJ}\lambda_2 A_c}{U_c^{LJ}\lambda_c A_2} \quad , \quad \frac{U_3^{LJ}\lambda_3 A_c}{U_c^{LJ}\lambda_c A_3} \quad , \quad \cdots \quad , \quad \frac{U_n^{LJ}\lambda_n A_c}{U_c^{LJ}\lambda_c A_n} \tag{5.5}$$

This expression gives a parameter, whose fundamental unit from dimensional analysis yields

$$\frac{U^{LJ}\lambda A_c}{U_c^{LJ}\lambda_c A} \,[=]\, \frac{M'L'}{T'^2} \tag{5.6}$$

where M', L', T' are mass, length and time respectively. This is dimensionally consistent to the unit of Force F. Therefore, the expression in Eq. 5.6 would become

$$\frac{U^{LJ}\lambda A_c}{U_c^{LJ}\lambda_c A} \approx \frac{F^{LJ}}{F_c^{LJ}} \tag{5.7}$$

Since the surface area of the system under consideration remained constant, thus $A = A_c$. Eq. 5.7 then becomes

$$\frac{U^{LJ}\lambda}{U_c^{LJ}\lambda_c} \approx \frac{F^{LJ}}{F_c^{LJ}} \tag{5.8}$$

Thus for the different values of λ, the expression for becomes

$$\frac{F_1^{LJ}}{F_c^{LJ}} \quad , \quad \frac{F_2^{LJ}}{F_c^{LJ}} \quad , \quad \frac{F_3^{LJ}}{F_c^{LJ}} \quad , \quad \cdots \quad , \quad \frac{F_n^{LJ}}{F_c^{LJ}} \tag{5.9}$$

$$(F_{md})_{d1} \quad , \quad (F_{md})_{d2} \quad , \quad (F_{md})_{d3} \quad , \quad \cdots \quad , \quad (F_{md})_{dn} \tag{5.10}$$

where $(F_{md})_d$ is the dimensionless particle-boundary force of interaction.

Eq. 5.8 and Eq. 5.10 would serve as key expressions for the F_{md} inclusion to the modi-

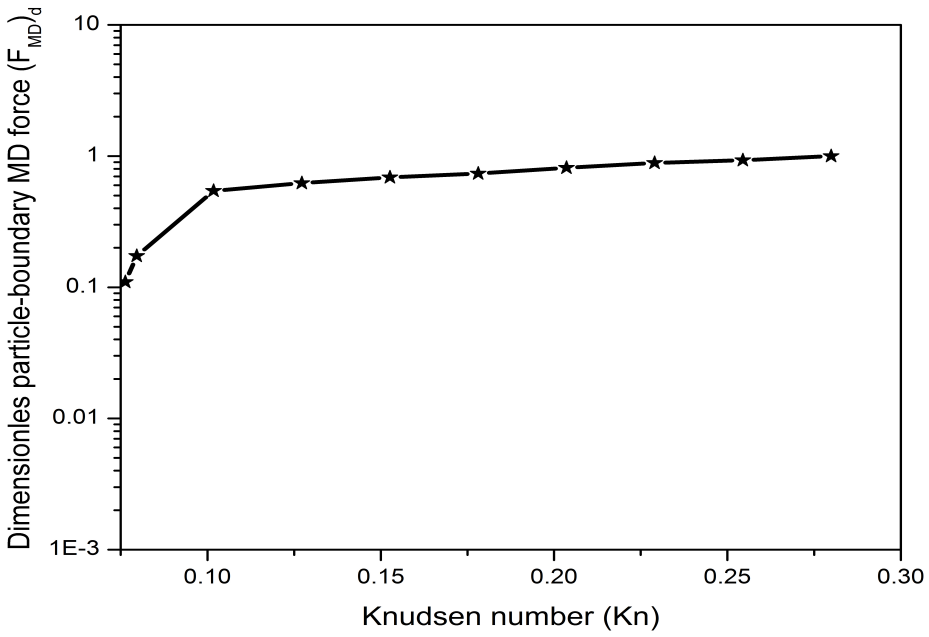

Figure 5.2: Dimensionless particle-boundary interaction force from silica + n-octane system F_{md} was a function of the Knudsen number Kn

fied LB system for the LBMD formulation. Using these equations, the force based on the pair-potential between the silica and n-octane molecules was obtained. Fig. 5.2 showed the results of the dimensionless force as a function of the Knudsen number. This also implied that as the particle density increased with respect to the boundary, there was also an increase in the force of interaction. Unlike the conventional assumption of a linear relationship between boundary interaction force and fluid density in the continuum flow regime, this study has shown a non-linear force relationship existing between the shale(silica employed here) and the hydrocarbon (n-octane) as the density in a the slip flow regime, similar to the study by Gong et al. (2013). This force was then incorporated into the already existent LB model as a substitute for the mixed boundary condition.

5.2 Forcing Function Computation and Model Formulation

In an attempt to amalgamate both simulation methodologies, a more detailed understanding of the numerical implication when using the current mixed boundary condition and its approximation given in Eq. 2.54 had to be addressed. From Fig. 3.13 shown earlier, it was evident the mixed boundary condition showed limitations at high Knudsen numbers in the Knudsen regime. This was better represented numerically when the resultant particle-boundary forces for the mixed boundary condition LB system F_{lb-bc} were calculated for each of the corresponding Kn values as shown in Fig. 5.3. This indicated that at the early stage of the simulation $(s(Kn) = 0)$, the resultant force inducing the rate flux in the flow would gradually increase until it stabilized, and from there it would remain constant. This was to be expected as the system approached equilibrium. However, this occurs until a certain critical regime (Horbach and Succi, 2006, Madiebo et al., 2017) where the force kinks and continued increasing over time. Thus leading to unstable rate flux behavior that prevents the system's ability to achieve equilibrium. Taking the limit at the critical slip where $Kn_c = 0.155$, the dimensionless force for the system $(F_{lb-bc})_d$ could be computed. Fig. 5.4 showed a non-linear proportionality relationship between F_{lb-bc} and Kn. It is also worth noting that the F_{lb-bc} method seemed efficient at the early stages of the Kn regime due to its closeness in dynamic behavior to a macroscopic flow system. This should be expected since the standard LB method as stated earlier, was formulated on the basis of the Navier-Stokes equation via the Chapman-Enskog expansion. In order to model systems possessing higher Kn values, this concept had to be reformulated so as to have the ability to handle higher Kn flow regimes.

Beginning from the concept of the adjusted boundary condition to capture this effect, Eq. 2.51 could be recalled and modified into Eq. 5.11.

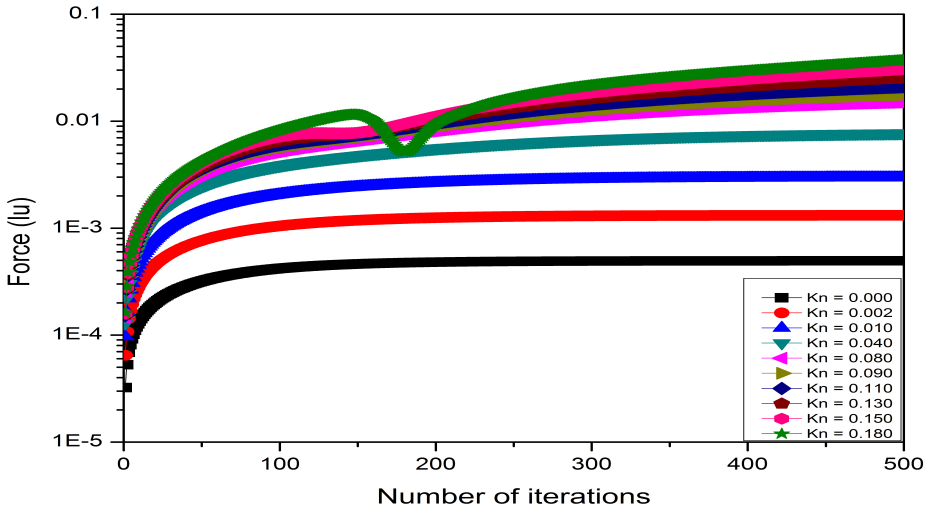

Figure 5.3: Force of fluid-solid particle interaction F_{lb-bc} from the lattice Boltzmann mixed boundary condition

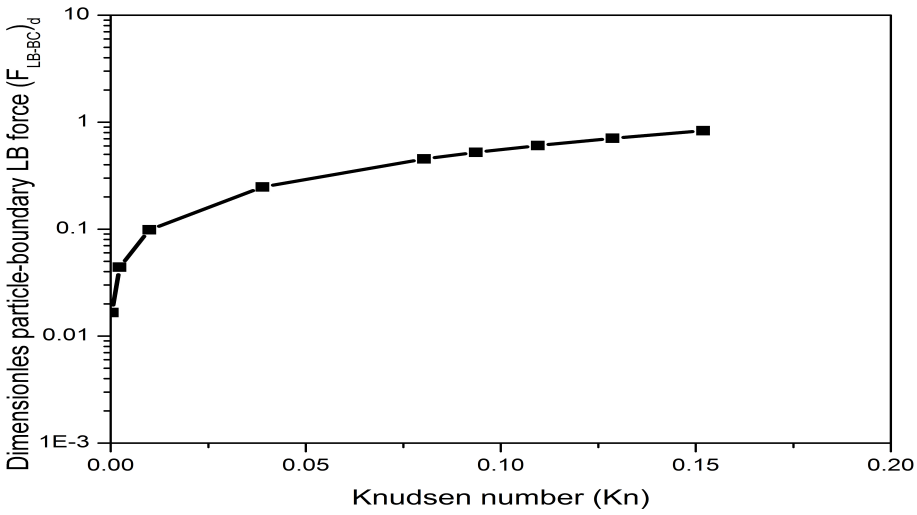

Figure 5.4: Dimensionless fluid-solid particle interaction force F_{lb-bc} from the lattice Boltzmann mixed boundary condition as a function of the Knudsen number Kn

$$f_i(x,t) = (1-s)\, f_{r'}(x,t) + s f_s(x,t) \tag{5.11}$$

Mathematically, this could be represented by either Eq. 5.12 or Eq. 5.13.

$$f_i(x,t) = f_{r'}(x,t) + s\left[f_s(x,t) - f_{r'}(x,t)\right] \tag{5.12}$$

$$f_i(x,t) = f_s(x,t) + (1-s)\left[f_{r'}(x,t) - f_s(x,t)\right] \tag{5.13}$$

Since the typical LB method uses the bounceback condition that could be reproduced here by setting $s(Kn) = 0$, hence the choice of Eq. 5.12. This means that the influence from this adjusted boundary condition with respect to a standard LB model comes from a particle density forcing function given by $s\left[f_s(x,t) - f_{r'}(x,t)\right]$. This can thus be equated to the nodal rock-fluid molecular interaction force $\left[\bar{F}_{sf}\right]_i = \left[\dfrac{F_{sf}}{\rho u/\Delta t}\right]_i$ with respect to the system momentum density that accounts for the slip flow regime. This implies that

$$s\left[f_s(x,t) - f_{r'}(x,t)\right] \equiv \left[\bar{F}_{sf}\right]_i \tag{5.14}$$

This could then be approximated by the particle-boundary MD interaction force as

$$\left\|\sum f_i(x,t)\,\vec{e_i}\right\| + F_{sf}\Delta t \cong \left\|\sum f_i(x,t)\,\vec{e_i} \pm \vec{F}_{md}\Delta t\right\| \tag{5.15}$$

This implementation of this formulation was summarized as shown in Fig. 5.5 and could be described as follows: Analogous to the standard LB model, first the system parameters f_i, τ, ρ, u were initialized along with the forcing function (F_{dpdl}). Next the initial macroscopic quantities ρ and $\vec{v}$ were computed. The applicable EOS using the defined F_{ff} as described in earlier section was included then the corresponding f_{eq} was calculated. F_{dpdl} was then imposed on the system and the collision operation performed.

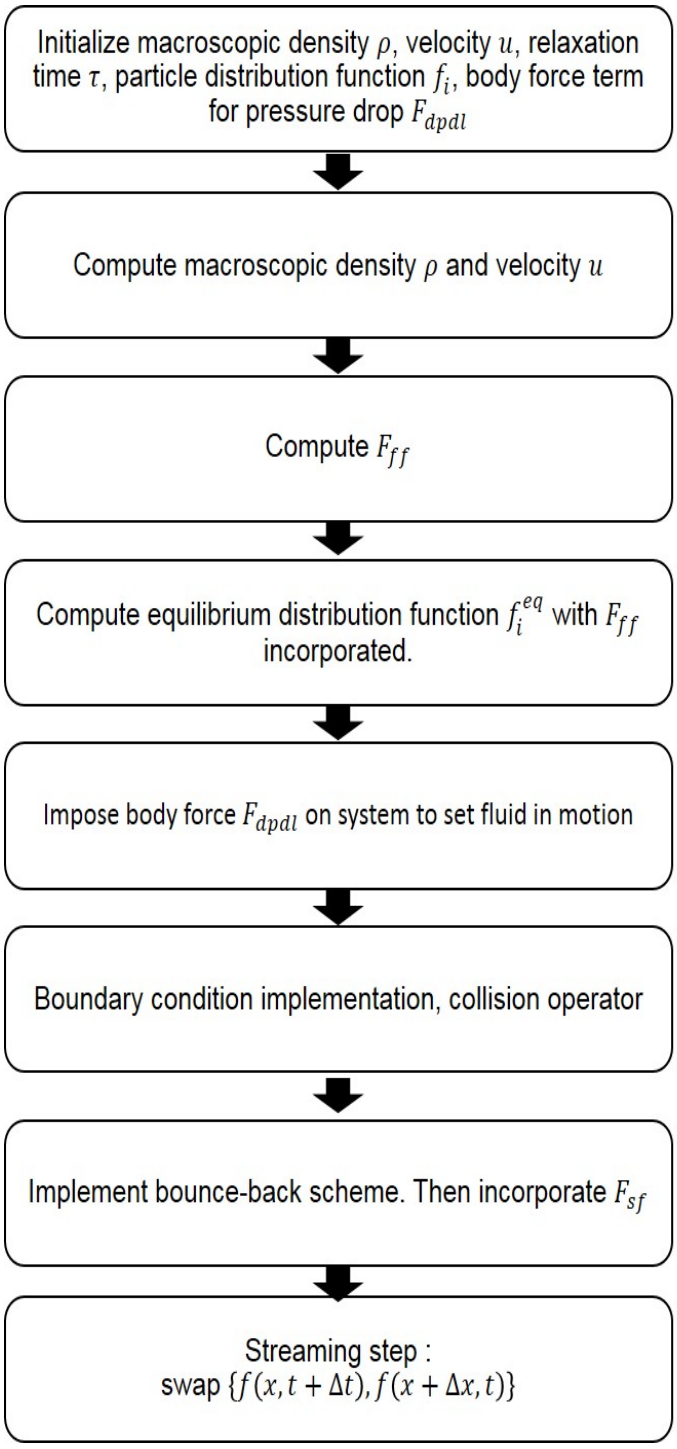

Figure 5.5: Procedure for LBMD simulation model for permeability computation

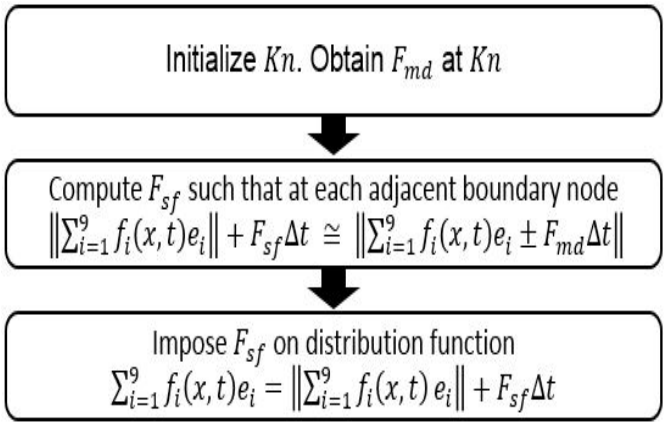

Figure 5.6: Procedure for fluid-solid force F_{sf} calculation

The bounceback boundary condition scheme was employed and then the solid-fluid interaction forcing function F_{sf} was incorporated, along with the final streaming step. Details of this incorporation and the F_{md} inclusion was shown in Fig. 5.6. To simply incorporate F_{md} into the LB system, a maximum particle-boundary interaction force occurring at the cut-off distance in the LB system $(F_{md})_{c-lb}$ was defined and multiplied by the prevailing dimensionless force $(F_{md})_d$ obtained from the MD system initially configured. It should also be noted that this force computed here is analogous to the interaction strength potential possessing an adsorption coefficient by Shan and Chen (1993), Sukop and Or (2004) when implemented in the LB model. Hence, it would be negative for stronger or attractive forces(wetting) and would grow increasingly more positive vice versa. Thus, the negative sign was employed for F_{md} in the organic nanochannel system. This approach was then used to compute the rate flux based on the procedure described earlier in Fig. 3.6, for the n-octane in silica along with the apparent permeability of the porous media .

6. LBMD MODEL: SIMULATION DIAGNOSTICS

In order to validate this new model, two test cases were investigated and modeled.

(i) Flow in capillary nanochannel. (ii) n-Octane injection in nanofluidic chip experiment.

6.1 Flow in capillary nanochannel

Recalling the initial nanochannel system set up earlier for the LB method, the LB-BC model was replaced with the new LBMD model. This was done by by incorporating the F_{md} onto the boundary walls as shown in Fig. 6.1 and by following the procedure as described earlier in Fig. 3.6 and assuming $|F_{md}|_c$ as 1 in lattice units for this system, apparent permeability calculations were done. Firstly, the LB-BC solid fluid interaction force $|F_{lb-bc}|$ was compared to that generated by the LBMD model $|F_{lbmd}|$ as shown in Fig. 6.2. It was evident that this force could clearly compute beyond the critical slip regime, $s_c\,(Kn_c) \approx 0.155$, which was a limitation of the former. It was also worth noting that at the early stage of Kn regime, F_{lbmd} was not as efficient in estimating the rate flux as

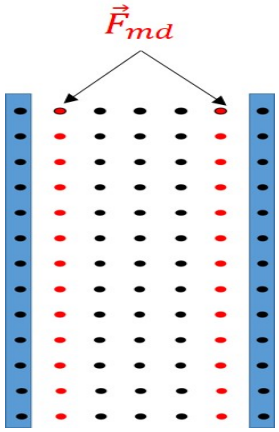

Figure 6.1: Schematic of nanochannel showing inclusion of F_{md} to nodes

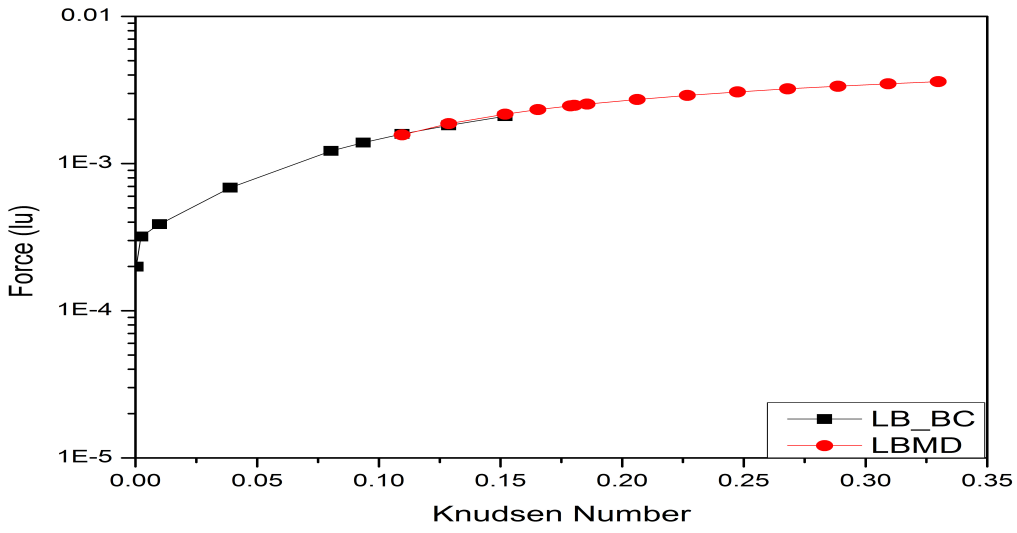

Figure 6.2: Comparison of the force from the LB boundary condition method and the the LBMD method

F_{lb-bc} as expected. Mainly because this regime is much closer to the Navier-Stokes flow, and for which a molecular simulation approach is not adequately suited to represent. This is because the the Navier-Stokes flow occurs in the macroscopic regime which was already effectively modeled with the standard LB method. With the emphasis of this study being to improve on the limitation of the prevalent boundary condition adjustment in the slip regime, the F_{lbmd} was then incorporated into the base LB model set-up in this work. A ratio of the apparent permeability values adjusted for slip effect from the Knudsen layer to their respective theoretical intrinsic permeability values and an understanding how they vary with respect to both the Knudsen number was shown in Fig. 6.3. A good match of both models was achieved, thus showing the precision of new model to still efficiently replicate the results from the LB-BC model.

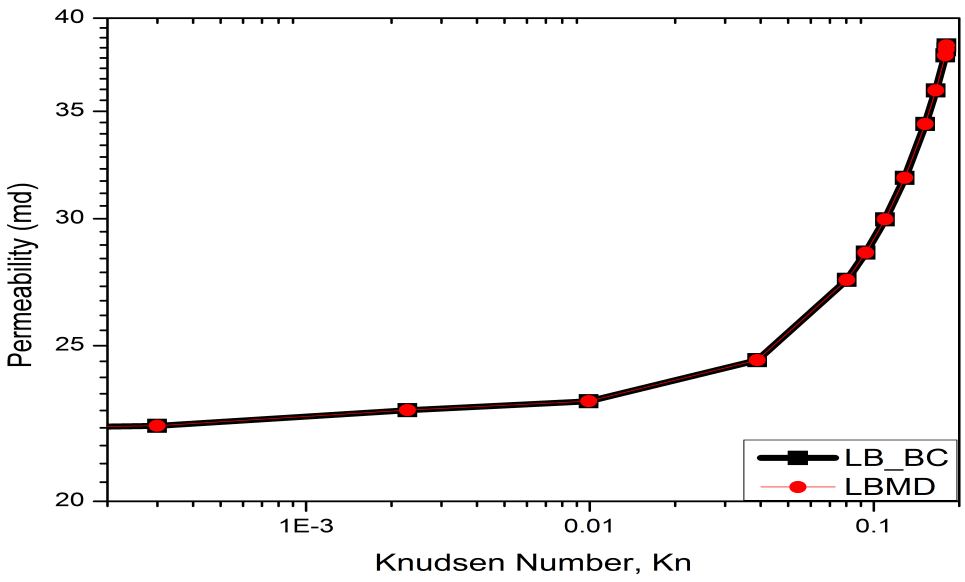

Figure 6.3: Relationship between normalized apparent permeability and Knudsen number for silica + n-octane system in slip flow regime

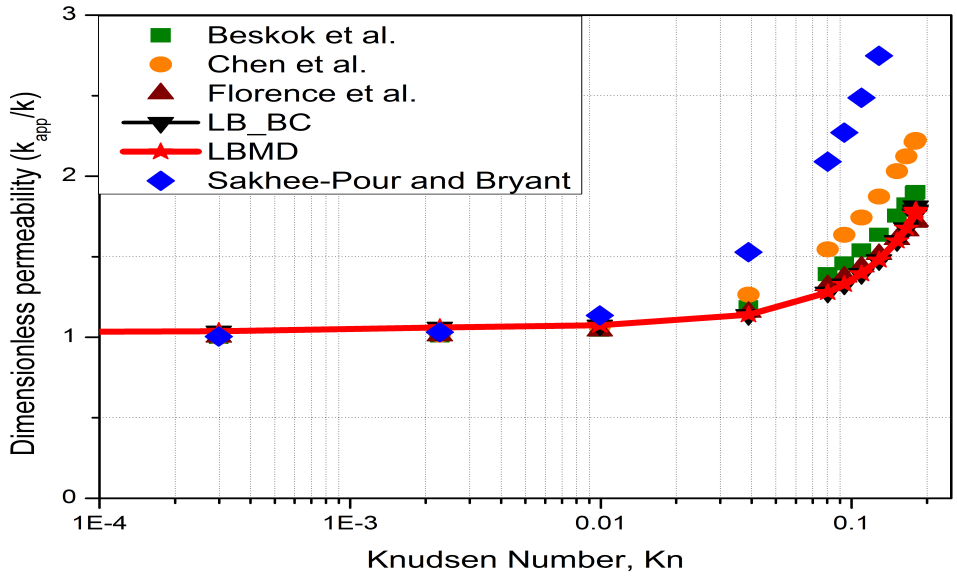

Figure 6.4: Comparison of normalized apparent permeability relationships and Knudsen number for slip flow regime

Subsequently, it's performance in comparison to existent correlations from literature was also evaluated and this was shown in Fig. 6.4. Good agreement was observed to exist between the LBMD simulation and all the other representative correlations. The best agreement seemed to exist between this model and the correlation proposed by Florence et al. (2007), as other correlations which marginally overestimated the apparent permeability as the slip flow regime approached its end. This could be attributed to the basis of

Dimensionless apparent permeability model	**Slip flow correction factors**
Florence et al. (2007)	$1 + 4Kn$
Beskok and Karniadakis (1999)	$(1 + \alpha\,(Kn))\left[1 + \frac{4Kn}{1 - b\dot{K}n}\right]; \quad \alpha = \frac{1.358}{1 + 0.17Kn^{-0.4348}}$
Sakhaee-Pour and Bryant (2012)	$1 + 13.58Kn$
Chen et al. (2015)	$1 + \frac{64}{3\pi}Kn$
This work($silica + n - octane$)	$1 + 2.67Kn$

Table 6.1: Comparison of apparent permeability correction factors

the flow geometry considered during their formulation. Wherein this case both were based on a singular straight micro or nanochannel (Florence et al., 2007), whereas the later correlations try to incorporate more complex geometric nanochannels and more physical parameter influence hence the slight variance from our LB simulation(Civan, 2009). Table 6.1 showed a comparison of the proposed apparent permeability correlations. As seen, the LBMD model does show very good agreement in modeling a nanochannel system and producing a good match with already existent models. It should be noted that this had been done simply by ensuring proper system set-up along with the essential underlying physics rather than attempted parameter-fitting. Therefore, this approach allowed the modeling of the fluid flow behavior in order to produce a unique apparent permeability correlation for this nanochannel system under consideration.

6.2 Hydrocarbon injection in nanofluidic chip experiment.

The next test case assessed was to model hydrocarbon flow analogous to the experimental set-up of a n-octane being injected into a nanofluidic chip. This concept employed here was that of a lab-on chip technology experiment and its procedure was analogous to the study by Alfi et al. (2016). The idea behind this technology simply involves the miniaturization of various laboratory functions integrated into a small microfluidic or nanofluidic chip. The motivation for adopting this process in this study was to use the nanofluidic device as a replica of shale rock media in order to investigate the dynamic behaviour of fluid flow in nanometer-sized pores prevalent in the pore distribution in a shale rock.

6.2.1 Lab-on-a-chip experiment: n-octane injection into glass nanofluidic chip

The nanofluidic device employed for this study was a glass nanofluidic chip that had photolitographically fabricated parallel channels. An image of the actual nanofluidic chip used for this work was shown in Fig. 6.5. This particular design had 20 parallel nanochannels at the center. Each channel was 5μm in width and 10 nm in depth. A glass substrate layered the top of the channels and thus covered the nanochannels in the vertical direction. There

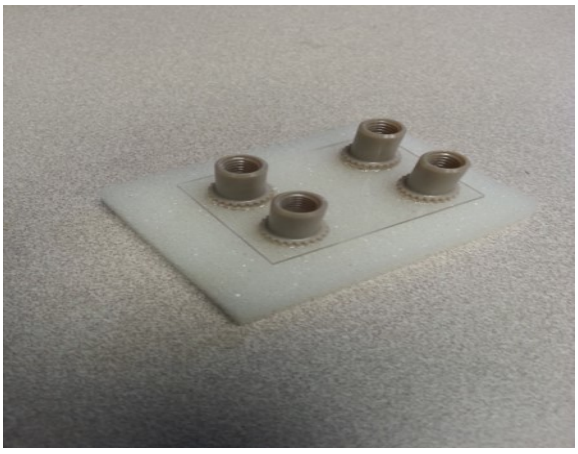

Figure 6.5: Fabricated nanofluidic chip

are four reservoir ports located towards each corner of the square chip. These ports are connected along a channels that are perpendicular to those at the center, for they would serve as inlet or exit ports into the parallel center channels.

The experimental set-up for this study was shown in Fig.6.6. The summary of the procedure employed for this study was in steps. First, proper placement of the nanofluidic chip under the microscope to ensure the the center channels were properly aligned and in focus. Next, the slow injection of the hydrocarbon ($10^{-5}\mu$L n-octane) into the channels through the inlet ports. This was to avoid high pressure drop across the chip that could lead to damage. Then the fluid in the channels were allowed to stabilize, so the internal pressure

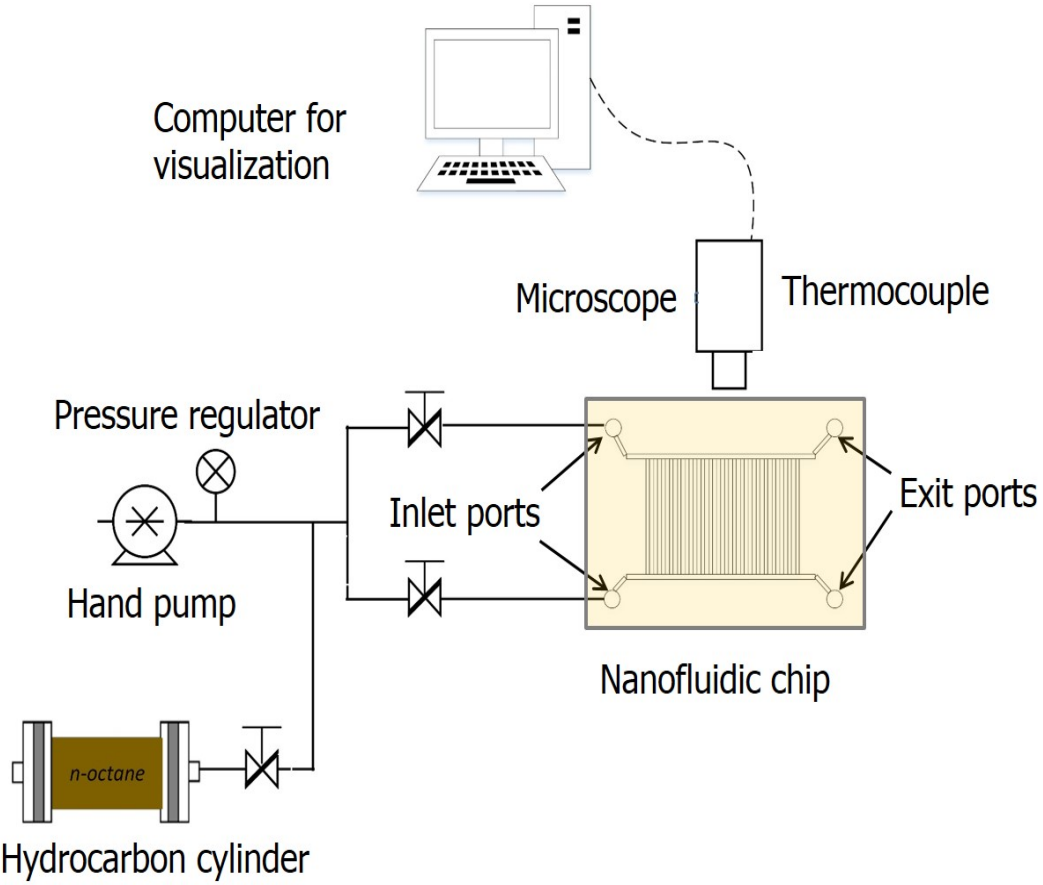

Figure 6.6: Schematic of the experimental set-up for the nanofluidic chip experiment

could equilibrate with the atmospheric pressure effect from the open exit ports once all the channels were filled. Finally, visualization and data acquisition via the microscope and computer monitor were done. After the this was set-up but before the experiment starts, trapped air was siphoned out of the nanochannels via suction and the channels replaced with hydrocarbon vapor.

In order to model the dynamic behaviour of the n-octane as it transitioned through the nanochannels, results for this study were generated in the form of time lapse snapshots as shown in Fig. 6.7a - Fig. 6.7f. In Fig. 6.7a, the experiment had already commenced. The two inlet ports had been injected with n-octane. By inducing a pressure drop across the inlet and exit ports. Experiment already began, injection of n-octane was from both inlet ports. In Fig. 6.7b, dry portions of channel continue to get occupied. Interestingly, n-octane seemed to show higher affinity to first occupy channels along injected path before other channels. In Fig. 6.7c, all the empty portions for the channels along the path of injection become occupied. In Fig. 6.7d, flow begins to converge to the center of the channels where there is still a some portion of the channels that are empty begins. In Fig. 6.7e, the final unfilled portion of the nanochannels located at the center of the channel got filled In Fig. 6.7f, n-octane flow in the channels got stabilized the and the nanofluidic chip became fully saturated.

From this study, it was clear that there was influence of confinement on the dynamics of the n-octane flow. This was due to the fluid-wall interaction between the hydrocarbon and the glass boundary wall. Slip flow was evident as the fluid transitioned through the channels, especially along the path of the injection channel. This means the velocity along these portions of the channels seemed to be faster than that relative to the fluid system. As such produced the resulting flow dynamics observed during this experiment.

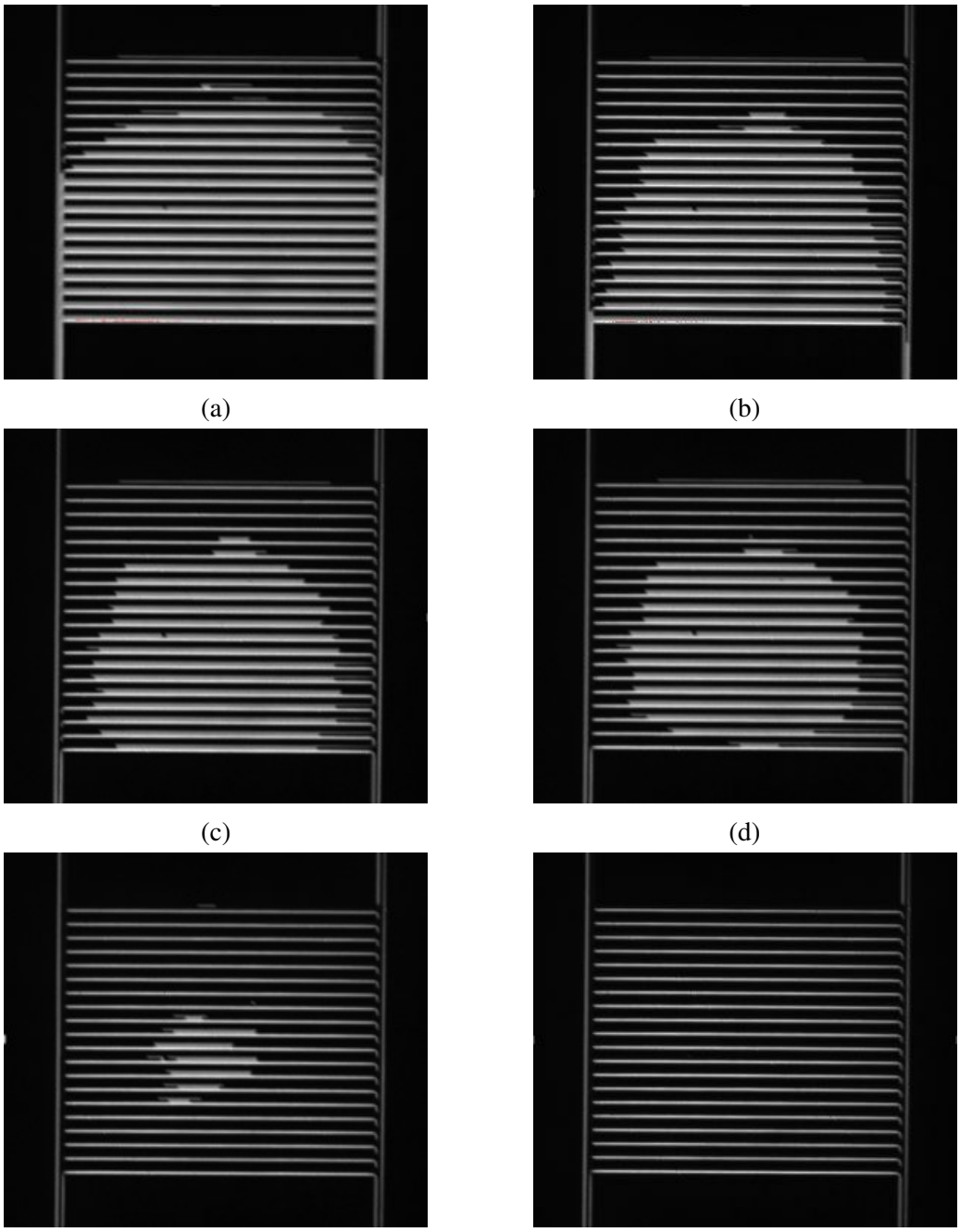

Figure 6.7: Snapshots during visualization of n-octane injection into nanofluidic chip. (a) Experiment already began, injection of n-octane was from both inlet ports (b) Empty portions continue to get occupied. Channels along injected path occupied first before center channels (c) Injection channels fully occupied (d) n-octane convergence to the center of the channels where there is still some empty portion of the channels begins (e) Final portion of the nanochannels that are empty and located at the center of the channel get filled (f) Channels get fully saturated with n-octane

6.2.2 Numerical simulation model: n-octane injection into glass nanofluidic chip

The next step of this study was to numerically model the experiment in the previous section using the LBMD model. This simulation was set-up so as to mimic the actual experiment. Fig. 6.8 showed the nanogrid model constructed for this simulation. The grid here was 212μm$\times$490μm. Each of the channels had a 5μm channel width. Temperature and Pressure were 298.15K and 1atm respectively. Since this simulation was done in 2D, the confinement effect was assumed to only be prevalent along the $x-y$ axis, and so slip flow was modeled as such. A flow regime having a dimensionless force of interaction $(F_{lbmd})_d$ of 0.0024 was also included to capture the confinement effect. Flow was set in the laminar regime. Boundary conditions employed for this study involved: A constant inlet velocity was set at the inlet ports; and a constant pressure condition was set at the exit ports. Refer to appendix B for details on setting up these boundary conditions. The simulation was then allowed to run a total of 10,000 steps to achieve equilibrium.

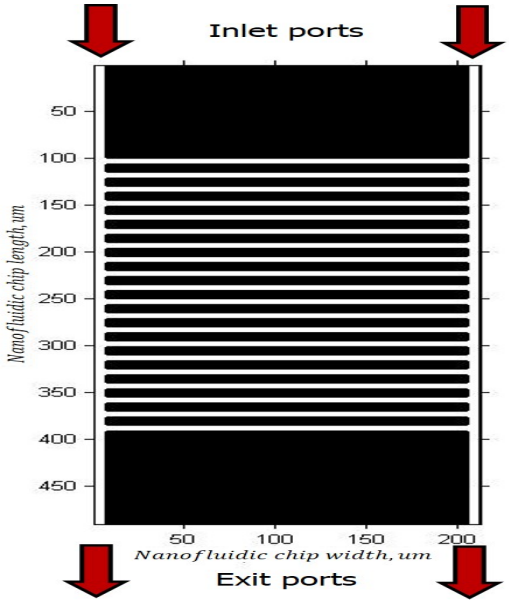

Figure 6.8: Schematic of nanogrid model representing nanofluidic chip

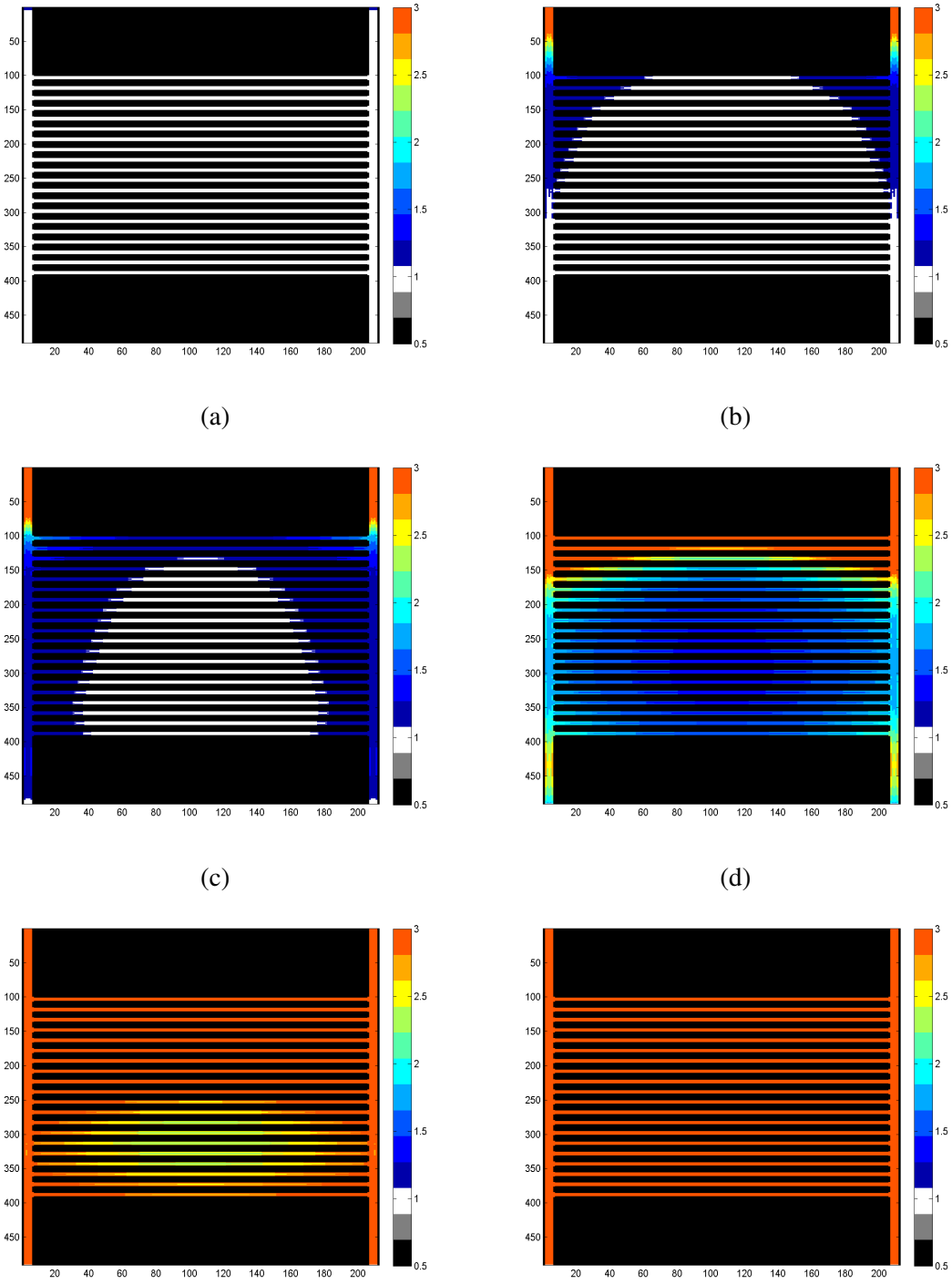

Figure 6.9: Snapshots of density variations of n-octane in LBMD simulation model after n number of Δt time steps where (a) $n = 0\Delta t$ steps; (b) $n = 500\Delta t$ steps; (c) $T = 800\Delta t$ steps; (d) $n = 2000\Delta t$ steps; (e) $n = 4000\Delta t$ steps; (f) $n = 5000\Delta t$ steps

Snapshots of the density distribution variation during the course of this simulation can be seen in Fig. 6.9a - Fig. 6.9f. In Fig. 6.9a, the simulation time step here is at $\Delta t = 0$steps. The channels are empty. In Fig. 6.9b, $\Delta t = 500$steps. Injection of n-octane from both inlet ports has already begun. Dry portions of channel continue to get occupied. Interestingly and just like with the experiment done earlier, n-octane seemed to show higher affinity to first occupy channels along the injected path before other channels. In Fig. 6.9c, $\Delta t = 800$steps. All the empty portions for the channels along the path of injection become occupied. In Fig. 6.9d, $\Delta t = 2000$steps. Flow began to converge to the center of the channels where there is still a some portion of the channels that are empty begins. In Fig. 6.9e, $\Delta t = 4000$steps. the final unfilled portion of the nanochannels located at the center of the channel got filled. In Fig. 6.9f, $\Delta t = 5000$steps. n-octane flow in the channels got stabilized the and the nanofluidic chip became fully saturated. From these results, a good degree of qualitative agreement seems to be prevalent between the results obtained from the lab-on-a-chip experiment and the numerical simulation performed using the LBMD model in this work. More importantly, the incorporation of the particle wall interaction that properly modeled the slip flow proved significant in determining flow dynamics in nanopore network distribution. This is evident when the standard LB model as shown in Fig. 6.10 is compared to the the LBMD model shown in Fig. 6.11. Even when compared to the experimental results in Fig. 6.12, the LBMD model still provided a better qualitative match. This helps improve the current understanding as to why permeabilities observed in very tight formations possessing ultra low permeability are usually underestimated with the conventional simulation methodology. As slip flow that tends to increase fluid velocity due to significant fluid-wall interactions that should be accounted for, is usually not. Ultimately, the results here showed that the LBMD model had the ability to properly model the dynamic fluid behavior for both the flow in capillary nanochannels and the n-octane flow in nanofluidic chip experiment.

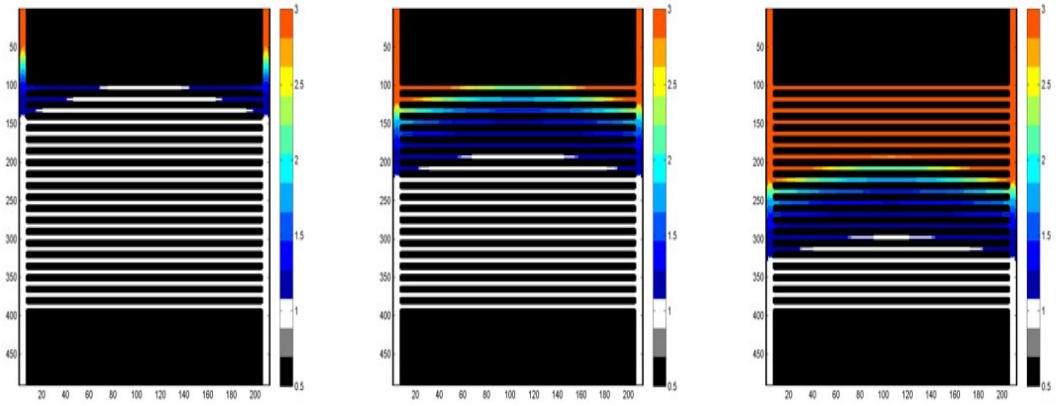

(a) (b) (c)

Figure 6.10: Snapshots of flow dynamics of n-octane flow in standard LB model

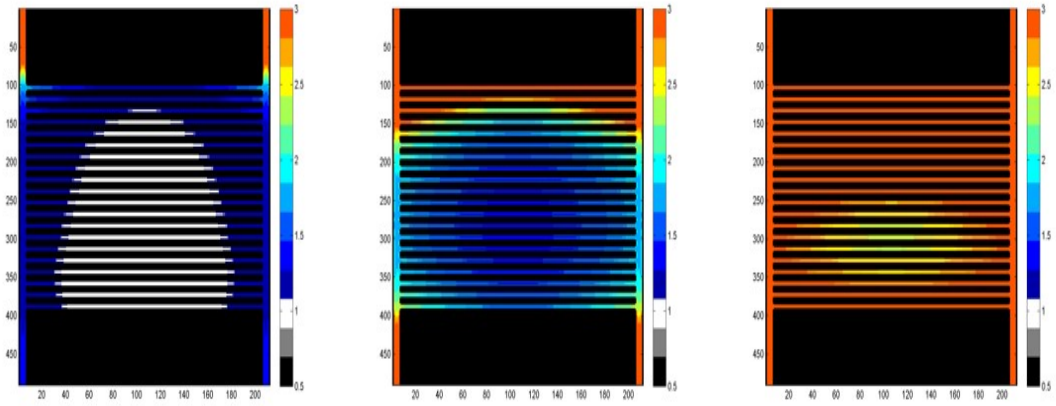

(a) (b) (c)

Figure 6.11: Snapshots of flow dynamics of n-octane flow in LBMD simulation model

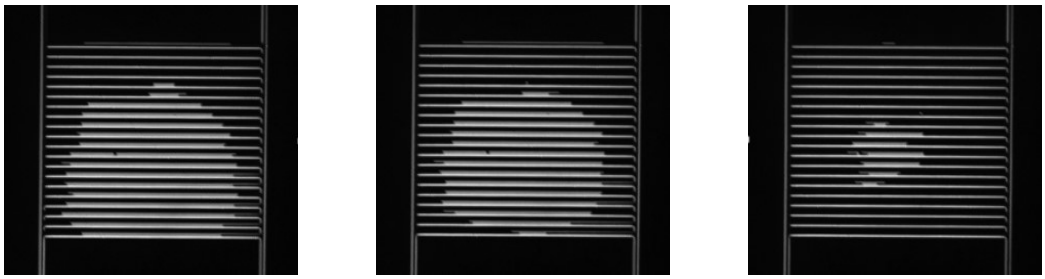

(a) (b) (c)

Figure 6.12: Snapshots of flow dynamics of n-octane in lab-on-a-chip experiment

7. CONCLUSIONS AND RECOMMENDATIONS

7.1 Conclusions

In this work, a combined lattice Boltzmann - molecular dynamics method was used to simulate hydrocarbon flow in nanochannels, analogous to capillaries found in the pore network of a shale matrix for flow in the region beyond the Navier-Stokes flow regime. An assessment of its quantitative ability in deducing apparent permeability for such systems was also done. To achieve this, a representative solid-fluid interaction force was computed from a molecularly set-up shale-hydrocarbon system, in the form of silica and n-octane respectively. The dynamics of this molecular interaction was governed by the $12-6$ Lennard Jones potential and the system dimension replicated one of a $4nm$ channel. This interaction force was then coupled into the lattice system simulation set-up and computations of the desired transport properties were done. In particular, the resultant effect on the volumetric flux per unit area and the apparent permeability of n-octane in a nanochannel system were studied.

It was evinced that the capillary wall effects caused a significant increase of the n-octane flow rate that essentially influenced the deduced permeability. Upon comparison of this lattice Boltzmann simulation with different established correlations, very good agreement was observed. Prior approaches that had aimed to capture this flow regime by implementing a mixed boundary condition criteria had shown limitations in it's ability to efficiently compute beyond a certain Knudsen flow regime of $Kn \approx 0.15$. Whereas, the approach in this study would allow for a more efficient apparent permeability model formulation without Knudsen flow regime limitations. Mainly because unlike the other mixed boundary condition system, this approach actually takes into account the molecular considerations of the actual system components (silica and n-octane) involved as part of the

model. It is noteworthy to indicate that a limitation of this present model could be the quality of the molecular dynamic system set-up. However, this is much better and easier to deal with during simulation modeling since a lot of experimental data to validate such molecular systems already exist. In addition, this new approach was also attempted to replicate a lab-on-a-chip experiment involving the injection of n-octane into a nanofluidic chip, representative of nanoscopic shale media. Good qualitative agreement with the experiment was achieved when comparisons of the dynamic behavior of the hydrocarbon as it saturated the nanochannel was compared to the simulation model. This could be attributed to the model's ability to efficiently capture the significant effect the fluid-wall interactions had on flow of the n-octane when percolating through such nanochannel pore network. Ultimately, this work aimed to serve as a foundation for an alternative approach to inclusion of different flow phenomena when computing transport properties in pore scale modeling.

7.2 Recommendations

Future recommendations to the present study could include the following:

- Development of the algorithm using a three-dimensional lattice model. Since this study assumed homogeneity of the shale rock in the z-direction, a 3D approach would serve better in dealing with heterogenous pore structures.
- Application of this pore scale modeling approach to digitized shale rock CT and SEM imagery.
- Development of more complex molecular dynamic models to accurately simulate multi-component hydrocarbon mixtures.
- Development of this algorithm to accommodate multi-phase modeling, so that the effects of the different phases during pore scale modeling can be studied.

REFERENCES

M. Abbaszadeh, A. Salehi, and A. Abbassi. Heat transfer enhancement in an asymmetrically heated channel partially filled with fibrous porous media-a lbm approach. *Journal of Porous Media*, 18(12):1201 – 1220, 2015. doi: doi:10.1615/JPorMedia.v18.i12.40.

P. Ahlrichs and B. Dunweg. Lattice-boltzmann simulation of polymer-solvent systems. *International Journal of Modern Physics*, C9(08):1429–1438, 1998. doi: 10.1142/S0129183198001291.

P. Ahlrichs and B. Dunweg. Simulation of a single polymer chain in solution by combining lattice boltzmann and molecular dynamics. *Journal of Chemical Physics*, 111(17):8225, 1999. doi: 10.1063/1.480156.

E. O. Aksnes and A. C. Elster. Porous rock simulations and lattice boltzmann on gpus. In *Parallel Computing: From Multicores and GPU's to Petascale, PARCO*, 2009. doi: 10.3233/978-1-60750-530-3-536.

A. Al-Kharusi and M. Blunt. Network extraction from sandstone and carbonate pore space images. *Journal of Petroleum Science and Engineering*, 56(4):219–231, 4 2007. doi: 10.1016/j.petrol.2006.09.003.

M. Alfi, H. Nasrabadi, and D. Banerjee. Experimental investigation of confinement effect on phase behavior of hexane, heptane and octane using lab-on-a-chip technology. *Fluid Phase Equilibria*, 423(Supplement C):25 – 33, 2016. doi: 10.1016/j.fluid.2016.04.017.

M. P. Allen and D. J. Tildesley. *Computer Simulation of Liquids*. Clarendon Press, New York, NY, USA, 1989. ISBN 0-19-855645-4.

B. Amara, M. E. Amine, P. Perre, and S. B. Nasrallah. Lattice-boltzmann analysis of capillary rise. *Journal of Porous Media*, 19(5):453 – 469, 2016. doi: 10.1615/JPorMedia.v19.i5.60.

S. Ansumali and I. V. Karlin. Consistent lattice boltzmann method. *Physical Review Letters*, 95(26):260605, 2005. doi: 10.1103/PhysRevLett.95.260605.

S. Ansumali, I. V. Karlin, S. Arcidiacono, A. Abbas, and N. I. Prasianakis. Hydrodynamics beyond navier-stokes: Exact solution to the lattice boltzmann hierarchy. *Physical Review Letters*, 98(124502), 2007. doi: 10.1103/PhysRevLett.98.124502.

Z. Benamram, A. Tarakanov, H. Nasrabadi, and E. Gildin. Field-wide flow simulation in fractured porous media within lattice boltzmann framework. *Advances in Water Resources*, 96(Supplement C):170 – 179, 2016. doi: 10.1016/j.advwatres.2016.07.001.

A. Beskok and G. E. Karniadakis. A model for flows in channels, pipes, and ducts at micro and nano scales. *Microscale Thermophy. Eng.*, 3(1):43–77, 1999. doi: 10.1080/108939599199864.

P. L. Bhatnagar, E. P. Gross, and M. Krook. A model for collision processes in gases. i. small amplitude processes in charged and neutral one-component systems. *Phys. Rev.*, 94(3):511 – 525, 1954. doi: 10.1103/PhysRev.94.511.

M. Blunt, B. Bijeljic, H. Dong, O. Gharbi, S. Iglauer, P. Mostaghimi, A. Paluszny, and C. Pentland. Pore-scale imaging and modelling. *Advances in Water Resources*, 51 (Supplement C):197–216, 2013. doi: 10.1016/j.advwatres.2012.03.003.

E. Boek and M. Venturoli. Lattice-boltzmann studies of fluid flow in porous media with realistic rock geometries. *Computers & Mathematics with Applications*, 59(7):2305–2314, 2010. doi: 10.1016/j.camwa.2009.08.063.

E. S. Boek. Pore scale simulation of flow in porous media using lattice-boltzmann computer simulations. In *Society of Petroleum Engineers*, 2010. doi: 10.2118/135506-MS.

J. M. Buick and C. A. Greated. Gravity in a lattice boltzmann model. *Physical review.E, Statistical physics, plasmas, fluids, and related interdisciplinary topics*, 61(5A):5307–5320, May 2000. doi: 10.1103/PhysRevE.61.5307.

Carlo C. The boltzmann equation and its applications. *Applied Mathematical Sciences*,

67, 1988. doi: 10.1007/978-1-4612-1039-9.

L. Chen, L. Zhang, and Q. Kang. Nanoscale simulation of shale transport properties using the lattice boltzmann method: Permeability and diffusivity. *Scientific Reports*, 5(8089), 2015. doi: 10.1038/srep08089.

S. Chen and G. D. Doolen. Lattice boltzmann method for fluid flow. *Annual Review of Fluid Mechanics*, 30(1):329–364, 1998. doi: 10.1146/annurev.fluid.30.1.329.

C. Chukwudozie. Pore-scale lattice boltzmann simulations of inertial flows in realistic porous media: A first principle analysis of the forchheimer relationship. Master's thesis, Louisiana State University, Louisiana, USA, 2011.

F. Civan. Effective correlation of apparent gas permeability in tight porous media. *Transport in Porous Media*, 82(2):375–384, 2009. doi: 10.1007/s11242-009-9432-z.

E. R. Cruz-Chu, Aleksei Aksimentiev, and Klaus Schulten. WaterâĹŠsilica force field for simulating nanodevices. *The Journal of Physical Chemistry B*, 110(43):21497–21508, 2006. doi: 10.1021/jp063896o.

J. Derksen, D. Eskin, Li-Shi L., and M. Krafczyk. Mesoscopic methods in engineering and science. *Computers & Mathematics with Applications*, 65(2):127 – 128, 2013. doi: 10.1016/j.camwa.2012.12.010.

D. dHumieres. Generalized lattice boltzmann equations. *Rarefied gas dynamics- Theory and simulations*, 159(2):450–458, 1992. doi: 10.2514/5.9781600866319.0450.0458.

H. Dong. *Micro-CT Imaging and Pore Network Extraction*. PhD thesis, Imperial College London, U.K., 2008.

E. Fathi and I. Y. Akkutlu. Lattice boltzmann method for simulation of shale gas transport in kerogen. *Society of Petroleum Engineers*, 2012. doi: 10.2118/146821-PA.

F. A. Florence, K. E. Rushing, J. Newsham, and T. A. Blasingame. Improved permeability prediction relations for low permeability sands. In *Rocky Mountain Oil & Gas Technology Symposium*. Society of Petroleum Engineers, 2007. doi: 10.2118/107954-MS.

D. Frenkel and B. Smit. *Understanding molecular simulation: from algorithms to applications*. Academic Press, San Diego, 2002.

U. Frisch, B. Hasslacher, and Y. Pomeau. Lattice-gas automata for the navier-stokes equation. *Phys. Rev. Lett.*, 56(14):pp.1505 – 1508, 1986. doi: 10.1103/PhysRevLett.56.1505.

M. G. Fyta, S. Melchionna, E. Kaxiras, and S. Succi. Multiscale coupling of molecular dynamics and hydrodynamics: application to dna translocation through a nanopore. *Multiscale Model. Simul.*, 5(4):1156–1173, 2007. doi: 10.1137/060660576.

U. Ghia, K. N. Ghia, and C. T. Shin. High-re solutions for incompressible flow using the navier-stokes equations and a multigrid method. *Journal of Computational Physics*, 48 (3):387–411, 1982. doi: 10.1016/0021-9991(82)90058-4.

B. Gong, X. Liu, and J. Yu. From molecular dynamics to lattice boltzmann: A new approach for pore scale modelling of multi-phase flow. In *International Petroleum Technology Conference.*, 2013. doi: 10.2523/IPTC16563MS.

Z. Guo and C. Shu. *Lattice Boltzmann method and its applications in engineering*. Advances in computational fluid dynamics. World Scientific, Singapore, May 2013.

Z. Guo and T. S. Zhao. Lattice boltzmann model for incompressible flows through porous media. *Physical review.E, Statistical, nonlinear, and soft matter physics*, 66(3.2B): 036304, Sep 2002. doi: 10.1103/PhysRevE.66.036304.

Z. Guo, B. Shi, T. S. Zhao, and C. Zheng. Discrete effects on boundary conditions for the lattice boltzmann equation in simulating microscale gas flows. *Phys. Rev. E*, 76(5): 056704, 2007. doi: 10.1103/PhysRevE.76.056704.

J. M. Haile. *Molecular Dynamics Simulation: Elementary Methods*. Wiley Interscience, United States, 1st edition, 1997.

X. He, S. Chen, and G. D. Doolen. A novel thermal model for the lattice boltzmann method in incompressible limit. *Journal of Computational Physics*, 146(1):282 – 300, 1998. doi: 10.1006/jcph.1998.6057.

J. R. Hill and J. Sauer. Molecular mechanics potential for silica and zeolite catalysts based on ab initio calculations. 1. dense and microporous silica. *The Journal of Physical Chemistry*, 98(4):1238–1244, 1994. doi: 10.1021/j100055a032.

A. Homayoon, A.H. Meghdadi Isfahani, E. Shirani, and M. Ashrafizadeh. A novel modified lattice boltzmann method for simulation of gas flows in wide range of knudsen number. *International Communications in Heat and Mass Transfer*, 38(6):827 – 832, 2011. doi: 10.1016/j.icheatmasstransfer.2011.03.00.

J. Horbach and S. Succi. Lattice boltzmann versus molecular dynamics simulation of nanoscale hydrodynamic flows. *Phys. Rev. Lett.*, 96:224503, Jun 2006. doi: 10.1103/PhysRevLett.96.224503.

H. Huang, Z. Li, S. Liu, and X. Lu. Shan-and-chen-type multiphase lattice boltzmann study of viscous coupling effects for two-phase flow in porous media. *International Journal for Numerical Methods in Fluids*, 61(3):341 – 354, 2009.

F. Javadpour. Nanopores and apparent permeability of gas flow in mudrocks (shales and siltstone). *Petroleum Society of Canada*, pages doi:10.2118/09–08–16–DA, 2009.

S. G. Jennings. The mean free path in air. *Journal of Aerosol Science*, 19(2):159 – 166, 1988. doi: 10.1016/0021-8502(88)90219-4.

B. Jin and H. Nasrabadi. Phase behavior of multi-component hydrocarbon systems in nano-pores using gauge-gcmc molecular simulation. *Fluid Phase Equilibria*, 425 (Supplement C):324 – 334, 2016. doi: 10.1016/j.fluid.2016.06.018.

B. Jin, R. Bi, and H. Nasrabadi. Molecular simulation of the pore size distribution effect on phase behavior of methane confined in nanopores. *Fluid Phase Equilibria*, 452 (Supplement C):94 – 102, 2017. doi: 10.1016/j.fluid.2017.08.017.

W. L. Jorgensen, D. S. Maxwell, and J. Tirado-Rives. Development and testing of the opls all-atom force field on conformational energetics and properties of organic liquids. *Journal of the American Chemical Society*, 118(45):11225–11236, 1996. doi:

10.1021/ja9621760.

S. M. Kang, E. Fathi, R. J. Ambrose, I. Y. Akkutlu, and R. F. Sigal. Carbon dioxide storage capacity of organic-rich shales. *SPE Journal*, 16(4), 2011. doi: 10.2118/134583-PA.

L. J. Klinkenberg. The permeability of porous media to liquids and gases. In *Drilling and Production Practice*. American Petroleum Institute, 1941.

A. L. Kupershtokh and D. A. Medvedev. Lattice boltzmann equation method in electrohydrodynamic problems. *Journal of Electrostatics*, 64(7):581–585, July 2006 2006. doi: 10.1016/j.elstat.2005.10.012.

P. Lallemand and L. Luo. Theory of the lattice boltzmann method: Dispersion, dissipation, isotropy, galilean invariance, and stability. *Physical Review E*, 61(6):6546 – 6562, 2000.

J. Latt. *Hydrodynamic Limit of Lattice Boltzmann Equations*. PhD thesis, Universite De Geneve, 2007. URL `http://pleiades.epfl.ch/~jlatt`.

J. Latt. Choice of units in lattice boltzmann simulations. *Freely available online http://wiki.palabos.org/media/howtos.lbunits.pdf*, 2008.

T. Le, A. Striolo, and D. R. Cole. Co2âĂŞc4h10 mixtures simulated in silica slit pores: Relation between structure and dynamics. *The Journal of Physical Chemistry C*, 119 (27):15274–15284, 2015. doi: 10.1021/acs.jpcc.5b03160.

T. Le, S. Ogbe, A. Striolo, and D. R. Cole. N-octane diffusivity enhancement via carbon dioxide in silica slit-shaped nanopores âĂŞ a molecular dynamics simulation. *Molecular Simulation*, 42(9):745–752, 2016. doi: 10.1080/08927022.2015.1089991.

Y. Le Page and G. Donnay. Refinement of the crystal structure of low-quartz. *Acta Crystallographica Section B*, 32(8):2456–2459, 1976. doi: 10.1107/S0567740876007966.

E. W. Lemmon, M. O. McLinden, and D. G. Friend. *Thermophysical Properties of Fluid Systems*. NIST Chemistry WebBook, NIST Standard Reference Database Number 69. National Institute of Standards and Technology, Gaithersburg MD, 2005. doi: 10.18434/T4D303. URL `http://webbook.nist.gov`.

Sheng Luo, Hadi Nasrabadi, and Jodie L. Lutkenhaus. Effect of confinement on the bubble points of hydrocarbons in nanoporous media. *AIChE Journal*, 62(5):1772–1780, 2016. doi: 10.1002/aic.15154.

K. I. Madiebo, H. Nasrabadi, and E. Gildin. Volume 7b: Fluids engineering systems and technologies; mesoscopic simulation of slip motion for gas flow in nanochannels. In *International Mechanical Engineering Conference and Exhibition*, page V07BT09A024, 2015. doi: 10.1115/IMECE2015-53696.

K. I. Madiebo, H. Nasrabadi, and E. Gildin. Lattice boltzmann simulation of apparent permeability for gas flow in nanochannel. *Journal of Porous Media*, 20(10), 2017.

Z. ÎŚ. Makrodimitri, A. Heller, T. M. Koller, M. H. Rausch, M. S. H. Fleys, A. N. RenÃl'. Bos, G. P. van der Laan, A. P. FrÃűba, and I. G. Economou. Viscosity of heavy n-alkanes and diffusion of gases therein based on molecular dynamics simulations and empirical correlations. *The Journal of Chemical Thermodynamics*, 91:101–107, December 2015. doi: 10.1016/j.jct.2015.07.026.

M. G. Martin and J. Ilja. Siepmann. Transferable potentials for phase equilibria. 1. united-atom description of n-alkanes. *The Journal of Physical Chemistry B (ACS Publications)*, 102(14):2569 – 2577, 1998. doi: 10.1021/jp972543+.

N. S. Martys and H. Chen. Simulation of multicomponent fluids in complex three-dimensional geometries by the lattice boltzmann method. *Phys. Rev. E*, 53(1):743–750, 1996. doi: 10.1103/PhysRevE.53.743.

G. R. McNamara and G. Zanetti. Use of the boltzmann equation to simulate lattice-gas automata. *Phys. Rev. Lett.*, 61(20):2332 – 2335, 1988. doi: 10.1103/PhysRevLett.61.2332.

V. K. Michalis, A. N. Kalarakis, E. D. Skouras, and V.N. Burganos. Rarefaction effects on gas viscosity in the knudsen transition regime. *Journal of Computational Physics*, 9 (4-5):847 – 853, 2010. doi: 10.1007/s10404-010-0606-3.

A. Mohamad. *Lattice Boltzmann method: Fundamentals and Engineering Applications*

with Computer Codes. Springer-Verlag London, London, 2011.

M. Mondello and G. S. Grest. Viscosity calculations of n-alkanes by equilibrium molecular dynamics. *Journal of Chemical Physics*, 106(22):9327–9336, 1997. doi: 10.1063/1.474002.

P. Oren and B. Stig. Reconstruction of berea sandstone and pore-scale modelling of wettability effects. *Journal of Petroleum Science and Engineering*, 39(3):177–199, 2003. doi: 10.1016/S0920-4105(03)00062-7.

C. Pan, L. Luo, and C. T. Miller. An evaluation of lattice boltzmann schemes for porous medium flow simulation. *Computers and Fluids*, 35(8):898 – 909, 2006. doi: 10.1016 j.compfluid.2005.03.008.

S. Plimpton. Fast parallel algorithms for short-range molecular dynamics, March 1995. URL `http://lammps.sandia.gov`.

Y. H. Qian, D. D'HumiÃĺres, and P. Lallemand. Lattice bgk models for navier-stokes equation. *Europhysics Letters (EPL)*, 17(6):479 – 484, 1992. doi: 10.1209/0295-5075/17/6/001.

A. Rahman. Correlations in the Motion of Atoms in Liquid Argon. *Physical Review*, 136: 405–411, oct 1964. doi: 10.1103/PhysRev.136.A405.

D. C. Rapaport. *The Art of Molecular Dynamics Simulation*. Cambridge University Press, Cambridge, 2nd edition, 2004.

R. A. Reis, J. Vladimir Oliveira, and R. Nobrega. Diffusion coefficients in polymer-solvent systems for highly concentrated polymer solutions. *Brazilian Journal of Chemical Engineering*, 18(4):367, 12 2001. doi: 10.1590/S0104-66322001000400003.

D. A. Rothman and S. Zaleski. *Lattice-gas cellular automata: simple models of complex hydrodynamics*. Cambridge, U.K.; Cambridge University Press, 1997., 1997.

S. Roy, R. Raju, H. F. Chuang, B. A. Cruden, and M. Meyyappan. Modeling gas flow through microchannels and nanopores. *Journal of Applied Physics*, 93(8):4870 – 4879,

doi:10.1063/1.1559936, 2003.

A. Sakhaee-Pour and S. Bryant. Gas permeability of shale. *SPE Reservoir Evaluation and Engineering*, 15(4), 2012. doi: 10.2118/146944-PA.

M. J. Sanders, M. Leslie, and C. R. A. Catlow. Interatomic potentials for sio2. *J. Chem. Soc., Chem. Commun.*, pages 1271–1273, 1984. doi: 10.1039/C39840001271.

M. Sbragaglia, R. Benzi, L. Biferale, S. Succi, K. Sugiyama, and F. Toschi. Generalized lattice boltzmann method with multirange pseudopotential. *Physical Review E*, 75(2), 2007. doi: 10.1103/PhysRevE.75.026702.

W. Schmidt and C. Federrath. A fluid-dynamical subgrid scale model for highly compressible astrophysical turbulence. *Astronomy & Astrophysics (A & A)*, 528(A106):19, 2001. doi: 10.1051/0004-6361/201015630.

X. Shan and H. Chen. Lattice boltzmann model for simulating flows with multiple phases and components. *Physical Review E*, 47(3):1815 – 1819, 1993. doi: 10.1103/PhysRevE.47.1815.

X. Shan and H. Chen. Simulation of nonideal gases and liquid-gas phase transitions by the lattice boltzmann equation. *Phys. Rev. E*, 49(4):2941 – 2948, 1994. doi: 10.1103/PhysRevE.49.2941.

C. Shen, D. B. Tian, C. Xie, and J. Fan. Examination of the lbm in simulation of microchannel flow in transitional regime. *Microscale Thermophysical Engineering*, 8(4): 423 – 432, 2004.

J. Shi, L. Zhang, Y. Li, W. Yu, X. He, N. Liu, X. Li, and T. Wang. Diffusion and flow mechanisms of shale gas through matrix pores and gas production forecasting. In *SPE Unconventional Resources Conference Canada*. Society of Petroleum Engineers, 2013. doi: 10.2118/167226-MS.

V. Sofonea and Robert F. Sekerka. Boundary conditions for the upwind finite difference lattice boltzmann model: Evidence of slip velocity in micro-channel flow. *Journal of*

Computational Physics, 207(2):639 – 659, 2005. doi: 10.1016/j.jcp.2005.02.003.

C. H. Sondergeld, R. J. Ambrose, C. S. Rai, and J. Moncrieff. Micro-structural studies of gas shales. In *SPE Unconventional Gas Conference*. Society of Petroleum Engineers, 2010. doi: 10.2118/131771-MS.

A. Stukowski. Visualization and analysis of atomistic simulation data with ovito, the open visualization tool. *Modelling and Simulation in Materials Science and Engineering*, 18 (1):015012, 2010. URL `http://ovito.org/`.

S. Succi. Mesoscopic modeling of slip motion at fluid-solid heterogeneous catalysis. *Phys. Rev. Lett.*, 89(6):064502, 2002. doi: 10.1103/PhysRevLett.89.064502.

S. Succi, E. Foti, and F. Higuera. Three-dimensional flows in complex geometries with the lattice boltzmann method. *Europhysics Letters*, 10(5):433 – 438, 1989. doi: 10.1209/0295-5075/10/5/008.

S. Succi, L. Biferale, R. Benzi, M. Sbragaglia, and F. Toschi. Lattice kinetic theory as a form of supra-molecular dynamics for computational microfluidics. *Bulletin of the Polish Academy of Sciences: Technical Sciences*, 55(2):151–158, 2007.

K. Suga, S. Takenaka, T. Ito, M. Kaneda, T. Kinjo, and S. Hyodo. Evaluation of a lattice boltzmann method in a complex nanoflow. *Phys. Rev. E*, 82(016701), 2010. doi: 10.1103/PhysRevE.82.016701.

M. C. Sukop and D. Or. Lattice boltzmann method for modeling liquid-vapor interface configurations in porous media. *Water Resources Research*, 40(1), 2004. doi: 10.1029/2003WR002333.

M. C. Sukop and D. C. Jr. Thorne. *Lattice Boltzmann Modeling - An Introduction for Geoscientists and Engineers*. Springer-Verlag, Berlin Heidelberg, 1st edition, 2006. doi: 10.1007/978-3-540-27982-2.

V. Swami, C. R. Clarkson, and A. Settari. Non-darcy flow in shale nanopores: Do we have a final answer? In *SPE Canadian Unconventional Resources Conference*. Society of

Petroleum Engineers, 2012. doi: 10.2118/162665-MS.

A. Tarakanov, E. Gildin, and H. Nasrabadi. Simulation of flow in the solid matrix of shale reservoirs using lattice-boltzmann method. In *SPE Europec featured at 78th EAGE Conference and Exhibition*. Society of Petroleum Engineers, 2016. doi: 10.2118/180104-MS.

K. Vafai and S. J. Kim. Fluid mechanics of the interface region between a porous medium and a fluid layerâĂŤan exact solution. *International Journal of Heat and Fluid Flow*, 11(3):254 – 256, 1990. doi: doi:10.1016/0142-727X(90)90045-D.

B. W. van Beest, G. J. Kramer, and R. A. van Santen. Force fields for silicas and aluminophosphates based on ab initio calculations. *Physical Review Letters*, 64(16):1955 – 1958, April 16, 1990. doi: 10.1103/PhysRevLett.64.1955.

F. Verhaeghe, L. Luo, and B. Blanpain. Lattice boltzmann modeling of microchannel flow in slip flow regime. *Journal of Computational Physics*, 228(1): doi:10.1016/j.jcp.2008.09.004, 2009.

L. Verlet. Computer "experiments" on classical fluids. i. thermodynamical properties of lennard-jones molecules. *Phys. Rev.*, 159:98–103, Jul 1967. doi: 10.1103/PhysRev.159.98.

E. Viggen. The lattice boltzmann method with applications in acoustics. Master's thesis, Department of Physics, NTNU, Norway, 2009.

D. Wang, Z. Liu, J. Shen, and W. Liu. Lattice boltzmann simulation of effective thermal conductivity of porous media with multiphase. *Journal of Porous Media*, 18(10):929 – 939, 2015. doi: 10.1615/JPorMedia.2015012117.

F. P. Wang and R. M. Reed. Pore networks and fluid flow in gas shales. In *SPE Annual Technical Conference and Exhibition*. Society of Petroleum Engineers, 2009. doi: 10.2118/124253-MS.

H. Wang, X. Wang, X. Jin, and D. Cao. Molecular dynamics simulation of diffusion of

shale oils in montmorillonite. *The Journal of Physical Chemistry C*, 120(16):8986–8991, 2016a. doi: 10.1021/acs.jpcc.6b01660.

S. Wang, F. Javadpour, and Q. Feng. Molecular dynamics simulations of oil transport through inorganic nanopores in shale. *Fuel*, 171:74 – 86, 2016b. ISSN 0016-2361. doi: 10.1016/j.fuel.2015.12.071.

Q. Yang and C. Zhong. Molecular simulation of carbon dioxide/methane/hydrogen mixture adsorption in metalâĹŠorganic frameworks. *The Journal of Physical Chemistry B*, 110(36):17776–17783, 2006. doi: 10.1021/jp062723w.

P. Yuan and L. Schaefer. Equations of state in a lattice boltzmann model. *Physics of Fluids*, 18(4):042101, 2006. doi: 10.1063/1.2187070.

M. Zhang, G. Ye, and K. Breugel. Microstructure-based modeling of permeability of cementitious materials using multiple-relaxation-time lattice boltzmann method. *Computational Materials Science*, 68(Supplement C):142 – 151, 2013. doi: 10.1016/j.commatsci.2012.09.033.

X. Zhang, L. Xiao, and X. Shan. Lattice boltzmann simulation of shale gas transport in organic nano-pores. *Scientific Reports*, 4(4843), 2014. doi: doi:10.1038/srep04843.

Q. Zou and X. He. On pressure and velocity boundary conditions for the lattice boltzmann bgk model. *Physics of Fluids*, 9(6):1591 – 1598, 1997. doi: 10.1063/1.869307.

APPENDIX A

ANALYTICAL SOLUTION FOR FLOW IN A CHANNEL SYSTEM

This analytical solution for flow in channel is assumed to be analogous to flow between parallel plates, as derived from the fundamental Navier-Stokes equation.

From Eq. 2.5, the mass conservation was be obtained as

$$\nabla \cdot \vec{u} = \frac{\partial u}{\partial x} + \frac{\partial v}{\partial y} + \frac{\partial w}{\partial z} \tag{A.1}$$

For steady state, the fully developed flow equation forms where $v_y = v_z = 0$; $\dfrac{\partial v}{\partial y} = 0$ and $\dfrac{\partial w}{\partial z} = 0$. Hence,

$$\frac{\partial u}{\partial x} = 0 \tag{A.2}$$

For a two dimensional flow in terms of cartesian coordinates, the Navier-Stokes expression in Eq. 2.4 can be reduced to

$$\mu \frac{d^2 u}{dy^2} = \frac{1}{\mu} \frac{dp}{dx} \tag{A.3}$$

Upon integration,

$$u_y = \frac{1}{\mu} \frac{dp}{dx} \frac{y^2}{2} + A_1 y + A_2 \tag{A.4}$$

then invoke no slip flow boundary conditions such that $u\,(-H) = 0$ and $u\,(-H) = 0$. Recall that H is the fixed distance measured from the nanochannel center line to the inner boundary wall and y is the distance measured from the center line of the width of the channel. This yields

$$A_1 = 0 \qquad ; \quad A_2 = -\frac{1}{\mu} \frac{H^2}{2} \frac{dp}{dx} \tag{A.5}$$

This gives the expression for the velocity profile as

$$u_y = -\frac{1}{\mu}\frac{H^2}{2}\frac{dp}{dx}\left[1 - \frac{y^2}{H^2}\right] \tag{A.6}$$

Now the mean velocity u_m could be defined as

$$u_m = \frac{1}{\rho A}\int_A \rho u dA \tag{A.7}$$

If L is the plate width perpendicular to flow, u_m could be represented as

$$u_m = \frac{1}{L\rho\,(2H)}\int_0^L \int_H^{-H} \rho u dy dz = \frac{1}{H}\int_0^H \frac{dp}{dx}\left[\left(\frac{y}{H}\right)^2 - 1\right] dy \tag{A.8}$$

$$u_m = -\frac{H^2}{3\mu}\frac{dp}{dx} \tag{A.9}$$

$$\frac{dp}{dx} = -\frac{3\mu}{H^2}u_m \tag{A.10}$$

Substituting back into Eq. A.6 the dimensionless velocity profile then becomes

$$\frac{u}{u_m} = 1.5\left[1 - \frac{y^2}{H^2}\right] \tag{A.11}$$

APPENDIX B

BOUNDARY CONDITION FORMULATION

In this section, two different boundary conditions implemented in this work based on the work done by Zou and He (1997), were described. They are the constant flux boundary conditions and the constant pressure boundary conditions. Their method aimed at calculating the remaining unknown distribution functions whilst maintaining equilibrium condition assumptions that are normal to the boundary. The calculation done here would highlight a derivation only in the a single direction (North). Final solutions of the other directions (South,West and East) would only be presented here since they were all derived in similar manner.

B.1 Von Neumann boundary conditions (Constant flux)

In this case, the flux at the boundaries are constrained. A known velocity vector for the channel flow having x and y components with respect to the northern direction, could be specified as u_N and v_N respectively.

From the macroscopic density formulation in Eq. 2.17

$$\rho_N = f_0 + f_1 + f_2 + f_3 + f_4 + f_5 + f_6 + f_7 + f_8 \tag{B.1}$$

Using Eq. 2.18, the contributions of the x and y velocity components would be considered as

$$\rho_N u_N = f_1 + f_5 + f_8 - f_3 - f_6 - f_7 \tag{B.2}$$

$$\rho_N v_N = f_2 + f_5 + f_6 - f_4 - f_7 - f_8 \tag{B.3}$$

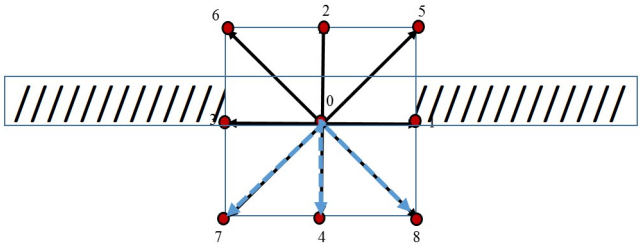

Figure B.1: Distribution functions to be computed (in blue) post streaming at a north-side boundary

If the equilibrium bounce-back condition normal to the boundary holds, then

$$f_2 - f_2^{eq} = f_4 - f_4^{eq} \tag{B.4}$$

This presents a system of four equations and four unknowns ρ_N, f_4, f_7 and f_8.

Rearranging Eq. B.1 and Eq. B.3 to obtain

$$f_4 + f_7 + f_8 = \rho_N - f_0 - f_1 - f_2 - f_3 - f_5 - f_6 \tag{B.5}$$

$$f_4 + f_7 + f_8 = f_2 + f_5 + f_6 - \rho_N v_N \tag{B.6}$$

Upon equating the right hand sides of Eq. B.5 and Eq. B.6

$$\rho_N - f_0 - f_1 - f_2 - f_3 - f_5 - f_6 = f_2 + f_5 + f_6 - \rho_N v_N \tag{B.7}$$

Then ρ_N would be obtained as

$$\rho_N = \frac{1}{(1 + v_N)} \left[f_0 + f_1 + f_3 + 2\left(f_2 + f_5 + f_6\right) \right] \tag{B.8}$$

Then from Eq. B.4, upon rearrangement

$$f_4 - f_2 = f_4^{eq} - f_2^{eq} \tag{B.9}$$

Recall that f^{eq} can be calculated from Eq. 2.29. Thus if substituted into Eq. B.9, it becomes

$$\begin{aligned} f_4^{eq} - f_2^{eq} = &\left[\frac{1}{9}\rho_N + \frac{1}{3}\rho_N\left(-1 \cdot v_N\right) + \frac{1}{2}\rho_N^2 - \frac{1}{6}\rho_N\left(u_N^2 + v_N^2\right)\right] - \\ &\left[\frac{1}{9}\rho_N + \frac{1}{3}\rho_N\left(1 \cdot v_N\right) + \frac{1}{2}\rho_N^2 - \frac{1}{6}\rho_N\left(u_N^2 + v_N^2\right)\right] = -\frac{2}{3}\rho_N v_N \end{aligned} \tag{B.10}$$

When Eq. B.10 was substituted back into Eq. B.9, f_4 would be obtained as

$$f_4 = f_2 - \frac{2}{3}\rho_N v_N \tag{B.11}$$

Next, substitute Eq. B.2 and Eq. B.11 into Eq. B.3

$$\rho_N v_N = f_2 + f_5 + f_6 - \left[f_2 - \frac{2}{3}\rho_N v_N\right] - f_7 - \left[\rho_N u_N - f_1 - f_5 + f_3 + f_6 + f_7\right] \tag{B.12}$$

Then f_7 would be obtained as

$$f_7 = f_5 + \frac{1}{2}\left(f_1 - f_3\right) - \frac{1}{6}\rho_N v_N - \frac{1}{2}\rho_N u_N \tag{B.13}$$

Similarly, f_8 was solved for by repeating the procedure for f_7 however in this case Eq. B.2 was rearranged and used to solve for f_7 in Eq. B.3

$$\rho_N v_N = f_2 + f_5 + f_6 - \left[f_2 - \frac{2}{3}\rho_N v_N\right] - \left[-\rho_N u_N + f_1 + f_5 - f_3 - f_6 + f_8\right] - f_8 \tag{B.14}$$

Then f_8 was obtained as

$$f_8 = f_6 - \frac{1}{2}(f_1 - f_3) - \frac{1}{6}\rho_N v_N + \frac{1}{2}\rho_N u_N \tag{B.15}$$

Thus, the unknowns for the northern boundary have now been specified. Similar approach could be used to obtain the unknown distribution functions in the other directions.

South side velocity boundary condition

$$\rho_S = \frac{1}{(1 - v_S)}\left[f_0 + f_1 + f_3 + 2(f_4 + f_7 + f_8)\right] \tag{B.16}$$

$$f_2 = f_4 + \frac{2}{3}\rho_S v_S \tag{B.17}$$

$$f_5 = f_7 - \frac{1}{2}(f_1 - f_3) + \frac{1}{6}\rho_S v_S + \frac{1}{2}\rho_S u_S \tag{B.18}$$

$$f_6 = f_8 + \frac{1}{2}(f_1 - f_3) + \frac{1}{6}\rho_S v_S - \frac{1}{2}\rho_S u_S \tag{B.19}$$

West side velocity boundary condition

$$\rho_W = \frac{1}{(1 - u_W)}\left[f_0 + f_2 + f_4 + 2(f_3 + f_6 + f_7)\right] \tag{B.20}$$

$$f_1 = f_3 + \frac{2}{3}\rho_W u_W \tag{B.21}$$

$$f_5 = f_7 - \frac{1}{2}(f_2 - f_4) + \frac{1}{6}\rho_W u_W + \frac{1}{2}\rho_W v_W \tag{B.22}$$

$$f_8 = f_6 + \frac{1}{2}(f_2 - f_4) + \frac{1}{6}\rho_W u_W - \frac{1}{2}\rho_W v_W \tag{B.23}$$

East side velocity boundary condition

$$\rho_E = \frac{1}{(1+u_E)}\left[f_0 + f_2 + f_4 + 2\left(f_1 + f_5 + f_8\right)\right] \tag{B.24}$$

$$f_3 = f_1 - \frac{2}{3}\rho_E u_E \tag{B.25}$$

$$f_7 = f_5 + \frac{1}{2}\left(f_2 - f_4\right) - \frac{1}{6}\rho_E u_E - \frac{1}{2}\rho_E v_E \tag{B.26}$$

$$f_6 = f_8 - \frac{1}{2}\left(f_2 - f_4\right) - \frac{1}{6}\rho_E u_E + \frac{1}{2}\rho_E v_E \tag{B.27}$$

B.2 Dirichlet boundary conditions (Constant pressure)

In this case, the pressure at the boundaries are constrained. Its solution is closely related to that done for the constant velocity boundaries done earlier. A known density as computed for the northern direction ρ_N, could be specified. Assuming the tangential velocity component to the boundary $u_N = 0$, the normal velocity component v_N could be calculated. Once again, Eq. B.1 through Eq. B.7 would be repeated, only this time in Eq. B.7, v_N would be obtained

$$v_N = -1 + \frac{1}{\rho_N}\left[f_0 + f_1 + f_3 + 2 * \left(f_2 + f_5 + f_6\right)\right] \tag{B.28}$$

When Eq. B.28 was substituted back into Eq. B.9, f_4 was obtained as

$$f_4 = f_2 - \frac{2}{3}\rho_N v_N \tag{B.29}$$

Then with similar procedure as before in the constant velocity scheme, f_7 and f_8 could be obtained respectively as

$$f_7 = f_5 + \frac{1}{2}\left(f_1 - f_3\right) - \frac{1}{6}\rho_N v_N \tag{B.30}$$

$$f_8 = f_6 - \frac{1}{2}\left(f_1 - f_3\right) - \frac{1}{6}\rho_N v_N \tag{B.31}$$

Thus, the unknowns for the northern boundary have now been specified. Similar approach could be used to obtain the unknown distribution functions in the other directions at constant pressure.

South side pressure boundary condition

$$v_S = -1 + \frac{1}{\rho_S}\left[f_0 + f_1 + f_3 + 2\left(f_4 + f_7 + f_8\right)\right] \tag{B.32}$$

$$f_2 = f_4 - \frac{2}{3}\rho_S v_S \tag{B.33}$$

$$f_5 = f_7 - \frac{1}{2}\left(f_1 - f_3\right) - \frac{1}{6}\rho_S v_S \tag{B.34}$$

$$f_6 = f_8 + \frac{1}{2}\left(f_1 - f_3\right) - \frac{1}{6}\rho_S v_S \tag{B.35}$$

West side pressure boundary condition

$$v_W = -1 + \frac{1}{\rho_W}\left[f_0 + f_2 + f_4 + 2\left(f_3 + f_6 + f_7\right)\right] \tag{B.36}$$

$$f_1 = f_3 + \frac{2}{3}\rho_W v_W \tag{B.37}$$

$$f_5 = f_7 - \frac{1}{2}\left(f_2 - f_4\right) + \frac{1}{6}\rho_W v_W \tag{B.38}$$

$$f_8 = f_6 + \frac{1}{2}\left(f_2 - f_4\right) + \frac{1}{6}\rho_W v_W \tag{B.39}$$

East side pressure boundary condition

$$v_E = -1 + \frac{1}{\rho_E}\left[f_0 + f_2 + f_4 + 2\left(f_1 + f_5 + f_8\right)\right] \tag{B.40}$$

$$f_3 = f_1 - \frac{2}{3}\rho_E v_E \tag{B.41}$$

$$f_7 = f_5 + \frac{1}{6}\left(f_2 - f_4\right) - \frac{1}{6}\rho_E v_E \tag{B.42}$$

$$f_6 = f_8 - \frac{1}{6}\left(f_2 - f_4\right) - \frac{1}{6}\rho_E v_E \tag{B.43}$$